Lara Elpelt BSc.

Towards the development of an ischemic chronic wound model using superparamagnetic nanoparticles

MASTER'S THESIS

to achieve the university degree of

Diplom-Ingenieurin

Master's degree programme:

Biotechnology

submitted to

Graz University of Technology

Supervisor

Ass.-Prof. Mag. Dr.rer.nat. Petra Kotzbeck
JOANNEUM RESEARCH Forschungsgellschaft mbH
Coremed - Kooperatives Zentrum für regenerative Medizin

Assoz. Univ.-Prof. Mag. Dr.rer.nat. Günter Hämmerle
Institut für molekulare Biowissenschaften
Karl-Franzens Universität Graz

Graz, June 2021

AFFIDAVIT

I declare that I have authored this thesis independently, that I have not used other than the declared sources/resources, and that I have explicitly indicated all material which has been quoted either literally or by content from the sources used. The text document uploaded to TUGRAZonline is identical to the present master's thesis.

Date, Signature

Abstract

A reliable ischemia model is necessary to study the effect of ischemia on the development of chronic wounds. Chronic wound research is limited by two complicating factors. First, rodent models for ischemia are still used, although they exhibit physiological characteristics, which are in sharp contrast with human skin. Porcine skin is more similar to human skin in terms of anatomy as well as physiology. Second, no current model exists, which leads to a locally defined ischemia in the skin without surgical interventions. However, those already established invasive methods of producing ischemia in animal models, such as the skin flap model, require surgical skills and would as a “side-effect” result in a massive inflammation, which in turn would interfere with the effects secondary to ischemia.

The goal of an ongoing study of the research centre JOANNEUM RESEARCH COREMED is the development of a novel ischemia model that uses magnetic nanoparticles to occlude blood flow in microcapillaries, allowing precise spatiotemporal control without the need of surgical intervention. Preliminary tests that guarantee the principle feasibility of the method and give an estimation on process relevant parameters, such as the strength of the applied magnet, are necessary. In addition, a detailed analysis of the porcine skin in the region of interest is needed. Consequently, the first part of the master thesis focusses on the detection and identification of location related variations in the structure and composition of porcine skin on a histological, as well as molecular level. In a second part, a novel *in vitro* and *ex vivo* magnetic nanoparticle-based ischemia model was designed, constructed, and tested.

Kurzfassung

Um die Effekte von Ischämien auf die Entstehung chronischer Wunden untersuchen zu können, wird ein zuverlässiges Ischämie-Modell benötigt. Jedoch wird die Forschung in diesem Bereich durch zwei wesentliche Faktoren behindert. Allem voran stellt die Abwesenheit eines zuverlässigen Tiermodells, das die menschliche Wundheilung korrekt imitiert, ein grundlegendes Problem dar. Obwohl Nagetiere (Maus, Ratte, usw.) physiologische Eigenschaften aufweisen, die im scharfem Kontrast zur menschlichen Haut stehen, werden sie immer noch sehr häufig in Wundheilungsstudien verwendet. Schweinehaut hingegen ähnelt sowohl anatomisch als auch physiologisch der menschlichen Haut. Allerdings stellt hier die Tatsache, dass es derzeit noch keine zufriedenstellende Methode gibt, um eine Ischämie ohne chirurgischen Eingriff zu produzieren, eine Hürde in der Forschung in diesem Gebiet dar. Die bereits etablierten invasiven Methoden zur Erzeugung von Ischämie in Tiermodellen, wie beispielsweise das Hautlappenmodell, erfordern chirurgische Fähigkeiten und ziehen natürlich eine eigene Entzündungsreaktion nach sich, welche sich auf die lokalen Entzündungsparameter auswirkt. Daher würden sie die Auswirkungen und Folgen des eigentlichen Forschungsthemas, der Ischämie, stören oder sogar vollständig überschatten.

Das Ziel einer laufenden Studie des Forschungszentrum JOANNEUM RESEARCH COREMED ist die Entwicklung eines Ischämie-Modells, welches magnetische Nanopartikel im Aufbau beinhaltet, um den Blutfluss in den Mikrokapillaren zu beeinflussen. Dadurch soll eine präzise, räumlich-zeitlich kontrollierte Ischämie in der Haut hervorgerufen werden, ganz ohne chirurgische Eingriffe. Um ein derart innovatives Modell etablieren zu können, sind eine Vielzahl von Vorversuchen erforderlich, die die grundsätzliche Machbarkeit der Methode untersuchen und eine Abschätzung prozessrelevanter Parameter, wie der Stärke des aufgebrachten Magneten, erlauben. Zusätzlich ist eine detaillierte Analyse der Schweinehaut im vorgesehenen Bereich erforderlich. Folglich liegt der Fokus dieser Masterarbeit in der Erkennung und Identifizierung ortsbezogener Unterschiede in der Struktur und Zusammensetzung von Schweinehaut auf histologischer als auch auf molekularer Ebene. In einem zweiten Teil wird ein vollkommen neuartiges *in vitro* und *ex vivo* Ischämie-Modell auf Basis magnetischer Nanopartikel entworfen, konstruiert und getestet.

Content

Introduction

The organ skin

The skin of an adult human has a surface of approximately 2 m^2 and an estimated weight of around 5 kg [1]. It is among the largest mammalian organs and represents an effective barrier between the outer surrounding and the inside of the organism [2]. Skin is constantly adapting to and keeping us in touch with the environment by regulating our body temperature, synthesizing vitamins, hosting nerve endings and by enhancing metabolic functions. Skin is also preventing the unregulated loss of water and solutes, as well as offering immunological protection against infection and injury [3]. The skin immune system (SIS) consists of resident immune cells, epithelial cells and the surrounding, vitamins-producing microenvironment. Via the SIS the tolerance and immunity to foreign and self-antigens is controlled [4]. Additionally, recent studies have shown that the microbiome of skin is of great importance. According to *Grice and Segre*, the skins microbiome exhibits the largest variability over time and holds the greatest phylogenetic diversity, compared to other mucosal microbiomes [5].

On different parts of the body, the skin shows different thicknesses and textures. Whereas it is paper-thin underneath the eyes, it is very thick on the soles of the feet or the palms of the hand [6]. Just as many other organs, the skin consists of a series of layered interfaces. Those layers are mostly dividable into an avascular epithelium, which can spontaneously regenerate, a so-called basement membrane zone and a vascular or stroma that supports the connective tissue and is unable to regenerate. In the case of skin, those layers are formed by the epidermis (ectodermic origin), the fibrous neurovascular dermis (mesodermic origin) and the subjacent hypodermis or subcutis, a fatty subdermal layer. Besides, it is also harbouring various other structures such as sweat and sebaceous glands, hair follicles, blood vessels, nerves and lymphatics [7], [8].

Epidermis

The avascular superficial layer of the skin is called epidermis. With a relative amount of up to 95%, it mainly consists of cornifying keratinocytes. Those keratinocytes differentiate through the five layers stratum basale, stratum spinosum, stratum granulosum, stratum lucidum and stratum corneum within a time of about 3 weeks. Besides those keratinocytes, the remaining 5 percent of the epidermis are formed by

melanocytes, Merkel receptor cells and a type of dendric cells (Langerhans cells). Since there are no blood vessels present in the epidermis, diffusion from dermal cells supplies the tissue with oxygen and nutrients [2], [3].

The main function of this external skin layer is the maintenance of an effective barrier over the entire body surface. The outermost layer, the stratum corneum, is primarily responsible for this. Since its cells are continuously worn or scraped, they have to be replaced by underlying epidermal cells. This epidermal regeneration is associated with cellular divisions in the lower, basal cell layer. During their migration towards the skin`s surface, they differentiate into layers of “flat plates”. The cells form so-called tonofibrils, an internal fibre system that offers a structural, supporting function [9], [10].

Dermis

The dermis is a connective tissue that can be sub-divided into two zones: the pars papillaris, a papillary layer, and the pars reticularis, a reticular layer. The pars papillaris refers to the upper part that is in contact with the epidermis via the basement membrane. The pars reticularis forms the lower part of the dermis and is adjacent to the underlying hypodermis [11].

The dermis is composed of various cell types including fibroblasts, mast and dermal dendritic cells, an extracellular matrix and fibrous proteins. Fibroblasts act as the main resident dermal cells and are in charge of the secretion of collagen, elastin and other extracellular dermal proteins. The dermal dendritic and mast cells play a role in the inflammatory and immunological reaction [1]. In contrast to the epidermis, the dermis hosts many blood and lymphatic vessels, as well as nerves and sensitive nerve endings. Moreover, a prime function of the dermis is the provision of strength and elasticity. Therefore, an embedment of elastic fibres and collagen in proteoglycans can be found [11]. Besides, with an average diameter of 600-3000 µm, the dermis accounts for most of the skin thickness [1].

Wound healing and chronic wounds

The process of skin wound healing is a highly dynamic and tightly regulated process including molecular, humoral and cellular mechanisms. It starts right after the wounding and lasts for a certain amount of time depending on the intensity of the injury. The skin wound closure can be realized by either regeneration or repair. Regeneration

refers to a specific substitution of the tissue, e.g. of the superficial epidermis. However, the main form of wound healing in adult skin is the skin repair, in which wound healing is achieved via fibrosis and scar formation [12].

The process of this wound repair can be sub-divided into the four overlapping phases: haemostasis and coagulation, inflammation, a proliferative phase with the formation of granulation tissue and the final remodelling scar formation phase. **Figure 1** gives an overview over three of the different stages of natural wound healing [13].

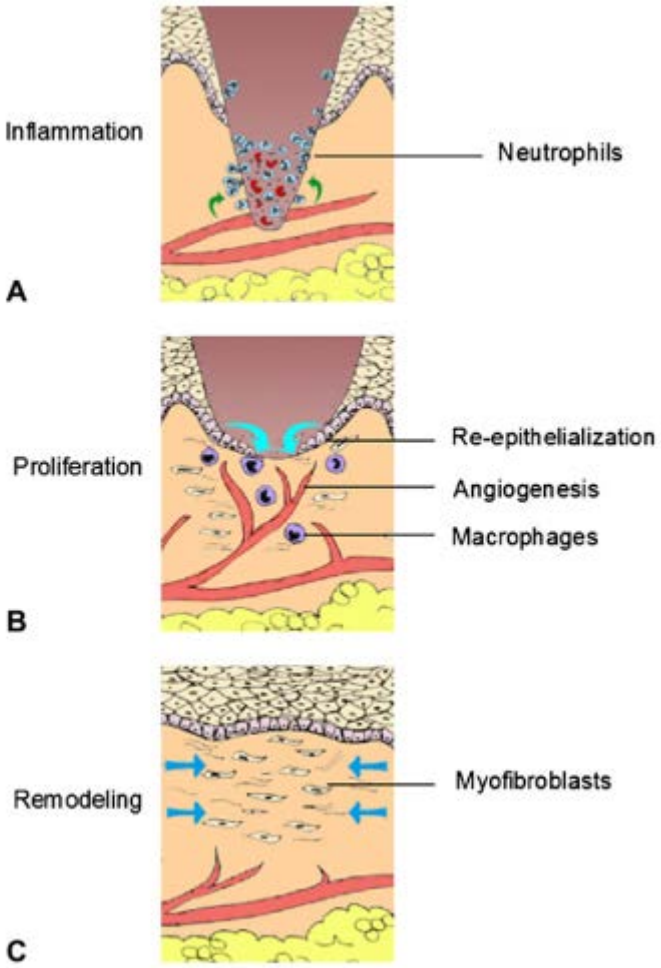

Figure 1: Physiologic wound healing occurs in four phases that may overlap in time: *Haemostasis, Inflammation, the proliferative phase and Remodelling.* ***(A) Inflammatory phase****. Secretion of growth factors and other chemical mediators that attract activated inflammatory cells and fibroblasts. Vasodilation allows neutrophils the moving into the wound site for phagocytosis of bacteria and debris. (****B) Proliferative phase****. Process of re-epithelialization starts. Detached epidermal cells migrate from the basement membrane to the wound surface. Phagocytosis of debris and release of growth factors such as vascular endothelial growth factors (VEGF) that stimulate the formation of granulation tissue by activated macrophages****. (C) Final remodelling and scar formation phase:*** *remodelling of the collagen matrix by fibroblasts. The tissue strength enhances and wound thickness decreases. Later fibroblasts develop into myofibroblasts to promote contraction of the developing scar [14].*

Haemostasis

In this first stage, the main focus is on the formation of a preliminary wound matrix that is taking place right after the injury and is finished within some hours. Additionally, the early inflammatory response is initiated. If the skin injury outreaches the epidermis, a damage of blood and lymphatic vessels occurs, that results in a flushing of the wound to remove antigens and microorganisms. Subsequently, various clotting cascades are initiated and aggregation of activated thrombocytes occurs. Simultaneously, a platelets-triggered vasoconstriction of the injured vessels to minimize the blood loss is performed. A provisional matrix consisting of cytokines, growth factors, fibrin molecules, fibronectin and other molecules forms and functions as a scaffold structure for the invasion of fibroblasts, leukocytes, keratinocytes and endothelial cells [12]. In the following vasodilation also thrombocytes migrate into the wound matrix. The leukocytes and platelets facilitate the release of cytokines and growth factors, which then initiate the inflammatory response (*IL-6; IL1ß*, etc.) [13]. Subsequently, the collagen synthesis is stimulated (*FGF, TGF-ß,* etc.), a transformation of fibroblasts to myofibroblasts occurs (*TGF-ß, ACTA2*), angiogenesis is started (*FGF-2, VEGF-A, HIF-1α,* etc.) and even the re-epithelialization is promoted [12].

Inflammation

The next phase in wound healing refers to the inflammatory response, that can be separated into an early phase characterized by the recruitment of neutrophils and a second, late phase in which the prime function lies in the appearing and transforming of monocytes [12]. Neutrophils that are recruited to the site of injury and are usually present within the first days, are essential for proper healing since they are conducting phagocytosis as well as protease secretion that kills local bacteria and helps in the degradation of necrotic tissue. Additionally, they function as chemoattractants for other cells of the inflammatory phase and release mediators (*IL-1β* and *IL-6*, etc.) that then intensify the inflammatory response and incite *VEGF* and *IL-8* for improved repair response [13]. Approximately three days later also macrophages arise and promote the already ongoing phagocytosis process and the secretion of cyto-and chemokines and growth factors. In addition to their antigen-presenting and phagocytic function, they are also synthesizing numerous factors that promote cell proliferation and the remodelling of the extracellular matrix (ECM) [12], [15].

Proliferative phase

As the inflammatory phase abates, the proliferative stage starts after approximately 3-10 days. As already indicated above, the focus thereof is on the formation of granulation tissue, the covering of the wound surface and the restoration of the vascular network [15]. Therefore, this stage is characterized by the immigration of fibroblasts, neovascularization, early re-epithelialization from the rim of the wound, as well as the activation of angiogenesis by capillary sprouting. Additionally, fibronectin, collagen and other basic wound healing substances are synthesized. Those substances function as the basis for the new connective tissue that facilitates the closure and restores the tissue with mechanical strength. During this process an equilibrium between synthesis and degradation of the extracellular matrix settles, since the proliferation of fibroblasts continuously decreases, whereas the formation of collagen increases [12], [16].

Remodelling phase

The last stage of wound healing starts after approximately 21 days and can take up to one year. Via the apoptosis of cells, the granulation tissue formation is stopped. Throughout this process, the extracellular matrix and the components thereof undergo certain adaptions and changes [12]. Accordingly, collagen III is substituted by collagen I, which exhibits with its arrangement in parallel bundles, a stronger structure than its precursor [15]. Subsequently, wound contraction is aspired via the multiple attachment of collagen to myofibroblasts. By this, the surface available for scar development is reduced. Apart from that, wound metabolic activity and blood flow declines and also the angiogenesis ceases [12].

Chronic wounds

If a wound is kept in the inflammation state and cannot successfully proceed to the next stage, the proliferative phase, the wound can become chronic. Chronic wounds are defined as wounds that fail to heal through the body's natural healing process within three months [13]. Chronic wounds are related to significant social and economic burdens, at an individual as well as societal level. People suffering from chronic wounds experience major negative impacts on their quality of life, since they do not only cause constant pain, but also often lead to further disorders such as anxiety and depression [17], [18]. According to the *SCARLETRED HOLDING GMBH,* the prevalence of chronic wounds is currently about 200,000 to 300,000 individuals in

Austria and 1.5 to 2 million individuals (= 3-4/1000 people) in the European Union [19]. However, since the proportion of the elderly, as well as the prevalence of life-style diseases such as obesity or diabetes are constantly increasing, also a rise in the number of people suffering from chronic wounds will very likely occur in the near future. Consequently, it is of great importance that research in that field is not falling into oblivion. The affliction and impacts of chronic wounds on the life quality should not be underestimated. Even though it is important to also consider the causes as well as the thereby conditioned other disorders, not all the attention should exclusively be directed at them, but also at the individual treatment of the chronic wound [17], [18].

As mentioned above, during the body`s natural healing process, chronic wounds are kept in the inflammation stage, in which the inflammatory infiltrate is not resolved after removing bacteria and dead tissue. This infiltrate is associate with an excess of neutrophils, reactive oxygen species (ROS) and destructive enzymes, which perpetuate the cycle [13]. Often only minor traumatic injuries such as insect bites or even simple scratches in dry skin are the origins of chronic wounds. Usually those small lesions would heal within days or maximal weeks. However, in patients with certain underlying pathologies, such as diabetes-induced neuropathies, it can result in the formation of chronic wounds [15].

Various factors can delay wound healing: vascular insufficiency, chronic disease, diabetes, nutritional deficiencies, neurological defects, ageing and certain local factors such as pressure, oedema or infection. The treatment of chronic wounds has to be seen as a holistic endeavor that also requires an exact identification of the individual entities influencing the wound healing in a patient [14]. However, the aetiology of chronic wounds is highly diverse and the molecular and cellular mechanisms of wound healing as well as their impairments are still just poorly understood. This decelerates the design of clinical trials and complicates the identification of therapeutic targets. Additionally, there is an absence of a suitable animal model that provides a precise representation of the medical condition. Neuropathy, vascular insufficiency and chronic debility are difficult to reproduce. Besides, most animals show a loosed skin structure and wound healing is achieved by rapid construction, which is very different from the wound healing that can be seen at sites common for chronic wounds in humans. However, the use of animal models in that field is necessary to give insights into certain

pathways and to provide a directed approach on specific mechanisms related to chronic wounds [13].

Most of the chronic wounds can be categorized into the following groups: venous ulcers, pressure ulcers, and diabetic ulcers, as well as into a small fourth group secondary to arterial ischaemia [20].

Venous ulcers are very common and often occur in the lower limbs. The origins of this group of chronic wounds are venous hypertension and congestion that is often related to valvular defects or venous thrombosis. Backpressure builds up and increases the permeability of blood vessel, resulting in a leakage of macromolecules and red blood cells into the perivascular space. There, they function as chemoattractants for leukocyte infiltration. Fibrosis and oedema arise and impede the diffusion of oxygen, growth factors and nutrients to the wound site. Venous ulcers are usually quite large and shallow [13].

Compared to venous ulcers, arterial ones are less common. They are a result of arterial insufficiency that is usually caused by atherosclerosis, or in rare cases thromboemboli. The arterial lumen is narrowed, which reduces perfusion [15]. Consequently, ischemia and hypoxia can arise [20]. Occlusion of arteries, other than those supplying the brain or heart, are defined as peripheral vascular diseases. These diseases are promoted by various risk factors such as diabetes, smoking, anemia hypertension, and advanced age. Arterial ulcers are usually demarked with a sharp, round border and are located distally over bony prominences [13].

Pressure ulcers are commonly occurring in patients that suffer compromised mobility and decreased sensory perception due to e.g. neuropathies. They can be further aggravated in people that additionally show arterial and venous insufficiencies. Usually, they arise due to prolonged unrelieved pressure to skin. Consequently, the underlying muscle tissue experiences a decrease in oxygen tension, as well as an ischemic reperfusion injury and tissue necrosis [15].

As it has been known for some time already, diabetes can increase the risk of experiencing vascular pathologies. A serious complication of diabetes are diabetic foot ulcers. Abnormalities that are related to the development thereof are neuropathy, ischemia, and trauma [13]. That can then result in a structurally impeded, insensate limb, with an increased risk of ulceration. The macroscopic pathologies of diabetic

wounds are often linked to cellular abnormalities, like a low mitogenic potential. An improved understanding of those cellular changes can eventually also improve the development of novel treatment options [15].

Ischemia

A main factor in the development of chronic wounds is localized tissue ischemia. Ischemia refers to a seriously reduced blood flow due to severe obstruction of the arteries. The consequences thereof depend on the arteries subjected to this condition. If those are located in the brain, a stroke can follow; if the heart is affected, a heart attack possibly occurs. However, if the concerned arteries are located in the skin, the development and healing of wounds is affected [21]. Since ischemia is primarily caused by vascular complications, the supply of blood-borne products, such as oxygen, nutrients and circulating cells, to the wound site is limited and thereby the healing response is severely impaired. Most of the chronic wounds are to some degree related to local tissue ischemia from either chronic fibrosis (pressure, venous and diabetic ulcers) or atherosclerosis (diabetic ulcers) [22]. Additionally, the subsequent period of reperfusion after a period of ischemia has an effect on chronic wound healing [20]. Even though it has become well accepted that underlying ischemia is an important factor in this context, the reperfusion side has not got a lot of attention so far. In fact, in the development of all three major groups of chronic wounds, periods of ischemia, followed by periods of reperfusion occur. Those events probably happen repetitively, which potentiate the noxious impacts and makes them thereby sufficient to actually cause ulceration [22].

Modelling chronic ischemic wounds

The establishment of a mechanism-based model for the study of ischemic wounds in humans is hindered by various factors. The vast majority of people with chronic wounds also suffer from other comorbid conditions. This obviously complicates the research design that aims to address a pointed hypothesis. Additionally, also the aetiology, the age of the wound, and other factors of chronic wounds present in clinical situations, are very heterogeneous. And of course, not to be forgotten the ethical aspects of constant biopsy collection represent an issue. Accordingly, the establishment of a

preclinical model that provides a reliable representation of an ischemic wound is of high relevance [22].

Most of the already established models of chronic wounds in animals include the subjection of an acute wound to the primary clinical cause of the chronic wound, like ischemia, pressure or reperfusion damage [23]. Currently, there is no satisfactory method to reproduce an ischemic chronic wound without surgical intervention available. Those already established invasive methods, such as the skin flap model, require surgical skills and of course entail an own response, that has an impact on the internal inflammation parameters. Therefore, they would interfere or even override the effects secondary to ischemia, the actual research subject. Accordingly, a wound free model is of great interest and could definitely give a boost to research in this area.

In the following, three examples of the already available chronic wound models are briefly explained. Since none of these models is considered optimal, they all contain limitations.

In the rabbit ear ischemia, or rabbit ear ulcer model, an ischemic zone in the ear of the animal is generated. For this, about two or three arteries that supply the ear are sutured off before creating punch biopsy wounds. The wounds are usually down to the cartilage to get a full thickness wound without a vascular base with very little vascular supply. As the name indicates, rabbits are utilized in this model and even though these animals are inexpensive and breed prodigiously, they are unable to replicate human hypoxic wounds and are genetically not tractable [23]. Additionally, acute wounding is necessary. The same holds true for the so-called skin flap model. In this technique surgical incisions sever blood flow to certain regions of the skin, creating hypoxic zones [23]. Although, this model can be applied using the animal model pig, of whose skin is anatomically and physiologically much more similar to that of humans, it again requires acute wounding, which can impact the meaningfulness of the results. Nevertheless, none of the two models allows to study the reperfusion of the wounded tissue. However, as mentioned before the reperfusion of ischemic tissue is not only crucial for survival, but it can also cause secondary tissue damage via the release of free oxygen radicals and inflammatory mediators. The rat-magnet-ischemia-reperfusion model enables the study of ischemia-reperfusion (IR) through the surgical implantation of a metal plate. The plate is positioned under the skin of a loose skinned animal and periodic compressions of the skin using an external magnet are then produced. Since

the number and duration of the compressions can be varied, the size and extent of injury is controllable. By this, certain features of human chronic wounds, such as reduced blood flow, hypoxia or immune cell influx, can be replicated [23]. However, this model requires loose skinned animals, such as the mouse or the rat. The differences between rodent and human skin are major and consequently the results are clinically less relevant. In the following, the importance of choosing the correct model animal in the establishment of an ischemic chronic wound model is highlighted.

Porcine skin as a model for human skin

Porcine skin functions as the most commonly used model in human skin research. For a long time already, porcine skin has been utilized in numerous studies, especially in those focusing on wound healing, burns and scar tissue formation. Additionally, porcine skin has already been applied as a source of surgical mesh in e.g. hernia treatment [24].

Consequently, it is crucial to realize that regional variations that are known to be present in humans are also present in pigs. On different parts of the human body, the skin shows different thicknesses and textures. Whereas it is paper-thin underneath the eyes, it is very thick in the soles of the feet or the palms of the hand [21]. Such variations in the structure of the skin are not exclusively present in the human species. However, while human skin has been extensively studied, there is a paucity in the generation of data on location related differences in porcine skin [1].

The increased utilization of porcine skin as an experimental human analogue is the result of previous investigation that compared and analyzed the properties of skin of different domestic animals. From all the animals studied, the pig has shown to offer the highest amount of essential similarities making it the most appropriate model for human skin [25].

Most domestic mammals, particularly carnivores, exhibit morphological features that are often associated with a very dense hair coat. Those features are in relation with many other factors that affect the appropriateness of these mammals as a model for humans. Domestic animals that are densely haired, such as dogs or cats, generally have a very thin epidermis (10- 45 µm). Additionally, the continuous layer, stratum granulosum, is often not even present as such. The dermis of these animals consists

of an even papillary layer, that is rich in blood vessels, and a stratum reticulare, which contains a high amount of densely nested collagen fibres. Mast cells in cats are mainly found in superficial areas of the dermis, whereas in dogs they can be found surrounding the blood vessels in deeper parts of the dermis. The junction of the subcutis and dermis is wavelike and roughly intertwined [25].

In contrast to cats and dogs, domestic pigs belong to the group of sparsely- haired domestic mammals. As already indicated above, porcine skin is better suited as a human analogue since it fulfils most of the requirements. The outermost skin layer, the epidermis, of pigs is relatively thick and usually measures around 70- 140 µm. In comparison to that, the human epidermis ranges from 50- 120 µm. Previous studies have also found that their epidermis shows similar tissue turnover times and a likewise characterization of keratinous proteins [26]. Moreover, in electron microscopic analysis of the surface of the skin, the two species resemble the most and both show a rather slight pigmentation. Concerning the dermis, pigs show a well distinct papillary body with slender collagen fibres linked with active connective tissue cells. Adjacent to that, one can find a board stratum reticulare with well-integrated connective tissue fibres. Even though the amount of elastic fibre in the porcine dermis is to some extents lower than in the human`s, it is still higher than in most of the other species [27], [28]. Additionally, while *Moxr A. et.al* were studying thermal injury in pigs, they found out that the size and distribution of dermal blood vessels of pigs were highly similar to those found in human skin. They even stated: ´ *the similarity of blood vessels in human and porcine skin was found to be so great that it was with difficulty that one could be distinguished from the other* [29].

Accordingly, there are many similarities between human and porcine skin. A thick epidermis with a highly differentiated substructure, a sparely dense hair coat, a well-differentiated papillary body containing dermis and a rather high amount of elastic tissue. Nevertheless, also dissimilarities can be found. For example, humans have been identified to have a rich vascularization compared to pigs. The vascularisation in this animal refers to a low- to mid-dermal and sub-epidermal network. The main difference to humans is the less dense sub-epidermal network. Yet, the vascularization of the hair papilla and general lower region of the hair follicle again resembles that of humans [25]. Further dissimilarities can be found in the sebaceous glands. Moreover,

pigs have, as many other domestic mammals, only apocrine glands, whereas the human body surface mostly contains eccrine sweat glands [30].

Nonetheless, the similarities outweigh the differences, especially when compared with other domestic mammals. The use of porcine skin as a model for human skin is well justified. However, one must keep in mind that regional differences can also be found in the skin of this species and that not every region is equally suitable for a specific scientific question. To be able to construct an optimal experimental design as well as to improve the reproducibility of animal experiments, a high quality understanding and knowledge on the used skin region has to be given. Thus, the first part of this study focusses on the identification and analysis of location related differences in porcine skin.

Nanotechnology

Nanotechnology contributes to almost every field of science and is probably one of the most promising technologies of the 21st century. *Jordan et al.* even referred to it as the fifth technological revolution after the steam engine, steel, electricity and railways, cars and chemicals production, and computers [31]. Nanotechnology and nanoscience are commonly known as the study and application of extremely small things. It is hard to imagine just how small nanotechnology is [32]. If one divides the width of a hair into 100.000 pieces, then each piece would be about one nanometre wide. Materials of this magnitude show very unusual properties in a physical, chemical and biological context. Those unique features of nanoscale materials can be used to address obstacles in medicine, electronics, physics and many more areas that cannot be overcome using materials of any other magnitude [33].

Nanotechnology has definitely become one of the most important research topics in modern science. In the last couple of years, the interest in nanoscale materials, and particularly in magnetic nanoparticles (MNPs), has grown enormously and their various application opportunities have attracted the attention of industrial, as well as research communities in the biotechnological, medical, chemical and environmental sector. As an example, magnetic nanoparticles have already been successfully applied in purification processes and membrane separation water treatment. Similarly, in the medical field the use of MNPs has achieved great successes, especially in the area of drug delivery with the aim of directing the drug to the target side without causing any side effects and thereby giving the possibility of reducing the dosage through a better localized and more efficient targeting [34].

How tremendous the expansion of integrating nanotechnology in ongoing research has really been, shows a graph from a paper published by MDPI in January 2020 (**Figure 2**), based on statistics provided by *Web of Science* [35]. It depicts the numbers of papers that mentioned “magnetic nanoparticles”. One can clearly see the exponential increase in publications related to this topic (statistics for 2019 are not complete).

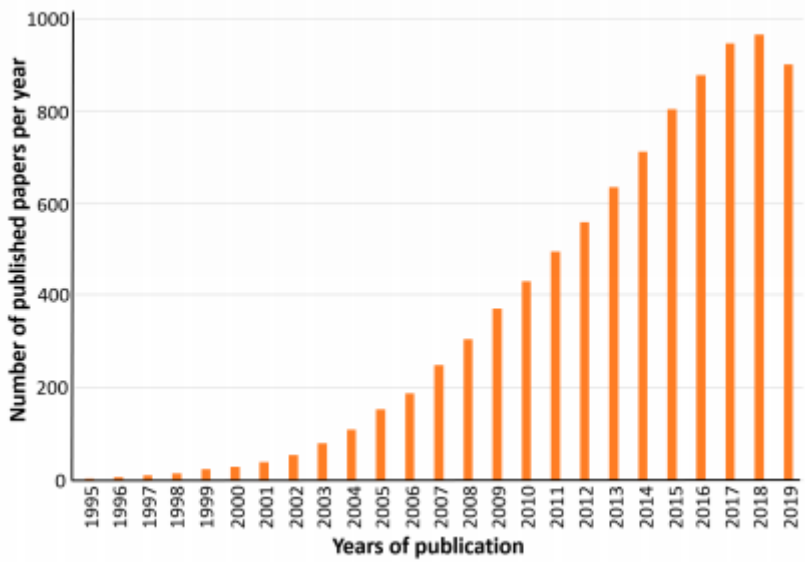

Figure 2: Number of published papers mentioning "magnetic nanoparticles". *The graph demonstrates how tremendous the expansion of integrating nanotechnology in ongoing research has been over the last years. (Statistics for 2019 incomplete) [35].*

Magnetic nanoparticles (MNPs)

Magnetic nanoparticles are of comparable size to biomolecules and show, compared to their bulk materials, superior properties, such as a unique magnetic response, excellent reactivity and a larger surface-to-volume ratio. One of the most frequently used magnetic nanoparticle type is iron oxide. Considering its high chemical and colloidal stability, as well as high biocompatibility and low cost, the frequency of its use is well justified. Among the many pure phases of iron oxide available in nature, the nanoscale zero-valent irons (nZVI), Fe_3O_4 and γ-Fe_2O_3, are the most popular regarding novel scientific applications [36], [37]. However, also those two have different physiochemical properties due to the different iron oxidation states. Magnetite (Fe_3O_4) is a ferromagnetic black-to-grey-coloured iron oxide of Fe (II) as well as Fe (III). It has the potential of acting as an electron donor due to the presence of the Fe^{2+} and has been the most extensively studied and used magnetic nanoparticle so far [38]. Moreover, iron is a naturally occurring metal in the human body, which makes iron-containing nanoparticles biocompatible. Since the body is able to metabolize the particles into its elements, it can also utilize them afterwards in subsequent metabolic processes [39].

Size and magnetic properties of MNPs

The magnetic properties of nanoparticles, such as the magnetic moment and anisotropy constant, strongly depend on the size and shape of the particles. In most of the anticipated applications, the particles achieve the best effect if the size of the nanoparticles is reduced below a critical value, which is typically around 10-20 nm [37], [40]. In larger magnetic particles, there are regions of uniform magnetizations that are separated by domain walls. Accordingly, those particles show a multi-domain-state. The formation of the domain walls depends on the magnetostatic effect that increases proportionally with the volume of the materials, as well as on the domain-wall energy that increases proportionally with the interfacial area between the domains. If the size of the particles is reduced below a critical value, each nanoparticle becomes a single magnetic domain [41]. Since below this critical volume it is more energy efficient to support the external magnetostatic energy of the single-domain state, than to create a domain wall, it becomes the preferred configuration. As already mentioned before, this critical diameter lies approximately in the range of 10-20 nm and is influenced by the individual material [40].

Single domain particles exhibit superparamagnetic behaviour if the temperature is above the so-called blocking temperature. In the case of magnetite (Fe_3O_4) and maghemite (γ-Fe_2O_3), the blocking temperature for particles with a critical volume of 20 nm is approximately at room temperature, meaning that particles smaller than 20 nm at a temperature of 20 °C show superparamagnetic properties [40], [41].

In the absence of an external magnetic field, superparamagnetic nanoparticles do not show permanent magnetization. In this state, there is no stable alignment of the magnetic moments of all particles given anymore. Only if an external magnetic field is applied, a high magnetic susceptibility becomes apparent [39]. In other words, if an external magnetic field is present, superparamagnetic particles show a high degree of magnetizability, since they align along the field lines with all the spins pointing in the same direction. Therefore, the individual nanoparticles possess a large, constant magnetic moment. They respond very fast to the applied magnetic field, but do not show a residual magnetism (remanence) if the magnetic field is removed. Subsequently, their coercivity, which is the field that is required to bring the magnetization to zero, is also negligible [41].

Biocompatibility and surface coating

The toxicity caused by magnetic nanoparticles on biological entities depends on a myriad of factors that are related to the general properties of the MNPs, such as the dosage, structural properties or the intended use [39]. Some particles exhibit, due to their chemical composition, a natural toxicity. Moreover, some materials that are not inert if applied in large quantities, can become toxic at nanoscale, such as gold, for example. Metals such as silver, nickel, cobalt and zinc are already known to be toxic to biological entities and are therefore unsuitable for biomedical application. Others, such as titanium or also iron oxide, are considerately less harmful to cells [42].

However, naked iron oxide nanoparticles, especially magnetite, show high chemical activity and are very easily oxidized in air. This does not only lead to a loss of magnetism and dispersibility, but is also, at the cellular level, one of the main causes of the toxicity [43]. This oxidative stress arises if there is an imbalance between reactive oxygen species (ROS), which are mainly the result of incomplete reduction of oxygen, such as H_2O_2 or hydroxyl radicals, and protective antioxidants, such as vitamin C or glutathione. The resulting accumulation of antioxidants causes the destruction of cellular proteins, lipids, enzymes and nucleic acids. Thereby the normal cellular processes can become greatly impaired leading to the formation of cell apoptosis, necrosis and disease [39].

Due to those reasons, providing a proper surface coating to effectively protect the stability of the iron oxide nanoparticles (IONPs) is essential. Strategies to ensure such a stabilisation compromise coating with organic molecules, such as surfactants, polymers and biomolecules, or coating with inorganic layers, such as silica, for example. Besides, those shells do not only protect the IONPs, but also provide space for further functionalization [44], [45].

One polymer that has been extensively studied, especially for drug delivery application, is polyethylene glycol (PEG). PEG is a stable, hydrophilic and biocompatible polymer, which can alter the surface characteristics of the particle it is immobilized on. Furthermore, PEG modification does not only reduce the response of the immune system to the magnetic nanoparticles, but also the risk of plasma protein adsorption on the particles surface by hindering interactions with plasma proteins. The magnetic particles used in our experiments are coated with PEG2000 [44].

Therapeutic applications of MNPs

Superparamagnetic nanoparticles show very special physical and chemical properties, which make them attractive candidates in a wide range of biotechnological, medical, chemical and environmental applications [40]. The therapeutic uses of MNPs that have been studied the most extensively so far include: signal enhancing in magnetic resonance imaging techniques (MRI), drug delivery by promoting the accumulation and deposition of bio-therapeutic compounds in certain microniches; and the production of a local-thermo-ablative effect and thereby mediating the destruction of cancer cells or biofilms (magnetic hyperthermia) [42], [46]. In the following, those three therapeutic uses are briefly described.

Magnetic resonance imaging (MRI)

Magnetic resonance imaging is a non-invasive technique that produces images of internal structures by using the magnetic character of protons and non-ionizing electromagnetic radiation [42]. In this technique radiofrequency pulses are used to force the protons into a high-energy state. Milliseconds after the removal of a radiofrequency pulse, the protons relax and turn back into a longitudinal state and thereby giving of an own radiofrequency signal that can be detected by the scanner. There are two types of relaxations that occur in the MRI process- the T1 relaxation and the T2 relaxation. A high T1 value means a quick realignment of the protons with the magnetic field. In contrast, the higher the T2 signal is, the slower the dephasing is happening. Depending on the water amount of the tissue, the protons in the body realign and dephase with differing rapidity. For example, protons in fat realign very fast and thus produce a high T1 signal. Consequently, 'T1-weighted' images are used to highlight fat in tissues of the body. In contrast, protons in water dephase rather slowly, which creates 'T2-weighted' images that highlight water in the tissues [46].

Contrast agents influence the T1 and T2 relaxation times of different tissues unequally in order to enhance the quality of the MRI images. T1 contrast agents produce bright positive signal intensities in images by altering the T1 relaxation times of the water protons and thereby increasing the possible conspicuousness of cells, whereas T2 contrast agents affect the transverse relaxation times of the water protons, leading to dark negative signal intensities in the obtained images [42].

Superparamagnetic nanoparticles are usually used as T2 contrast agents increasing the hypo-intense signals of certain regions. Since the effect they have on the relaxation time is proportional to the following disruption of the magnetic field, MNPs with a high magnetic susceptibility are preferred [45].

Even though only a rather small amount of superparamagnetic nanoparticle-based MRI contrast agents has been produced so far, they have already been successfully used in the detection and diagnosis of major diseases such as cancer, diabetes and cardiovascular disease [40], [47], [48].

Drug delivery

Another extensively studied therapeutic use of magnetic nanoparticles lies in the field of drug delivery. The aim thereof is the effective directing of the drug to the target site as well as the release of it in a well-controlled manner. Obviously, the success or failure of a therapy using a novel drug does not only depend on the drug itself, but also on how effectively it can be delivered to the target site. However, the systemic application of highly potent drugs, such as chemotherapeutics or antibiotics, via the intravenous or oral route, is always related to a certain risk of causing unintended side effects. However, in order to deliver sufficient amounts to the target site, high concentrations are needed. Very often, the systemic distribution of those highly concentrated drugs causes severe side effects, like bone marrow depression, hair loss, liver and kidney dysfunction, nausea and vomiting, etc. That in turn, limits the applicable dosage of those drugs. Consequently, it is of great importance to target the agent as precisely as possible to the target side and thereby reducing the resulting systemic, toxic side effects. Furthermore, the precise targeting enables one to work with lower doses, which results in a further reduction of toxicity [48].

As an example, *Alexiou C*. et al. were able to successfully treat squamous cell carcinoma in rabbits using magnetic nanoparticles that were bound to mitoxantrone, a chemotherapeutic agent (**Figure 3**). By using an external magnetic field, the mitoxantrone-bound particles were accumulated intratumoral, without causing signs of toxicity [48].

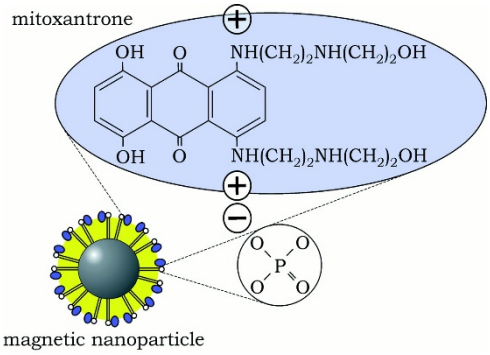

Figure 3: Structural formula of the chemotherapeutic agent "mitoxantrone" that was successfully applied in the treatment of squamous cell carcinoma in rabbits, *bound to a magnetic nanoparticle [42], [48].*

Magnetic hyperthermia

Magnetic hyperthermia (MH) describes a process, in which magnetic nanoparticles generate heat when subjected to an external alternating magnetic field (AMF) [49]. First attempts of using this strategy can be dated back to *Gilchrist et al.* in 1957, who tried to heat up tumors using magnetic particles in the presence of an AMF [50]. With the upsurge in nanotechnology and the increased interest in the application possibilities of MNPs, magnetic hyperthermia expanded into a well-established field of research. Today, the great potential of MH as an alternative approach for tumor treatment is undisputed. Recently, MNPs-MH based tumor treatments have been translated to clinical trials and have been successfully applied in the treatment of prostate cancer and glioblastoma [40], [51]. The greatest advantage of its therapeutic modality is the achievability of the selective elimination of cancer cells and deep tissue penetration without causing any harm to the surrounding tissues. In addition, the intracellular hyperthermia can even be further improved by conjugating the magnetic nanoparticles with cell-targeting ligands. Nevertheless, additional research concerning the effectiveness and efficiency of magnetic hyperthermia in cancer therapy is required to realise the full potential of nanotechnology in this context [51].

During the application of magnetic hyperthermia the temperature of a tumor is raised within the range of 43-46°, which leads to a change in the physiology of the cancer cell that causes apoptosis and necrosis. In order to successfully apply MNPs in cancer eradication, it is essential that sufficient amounts of the generated heat are delivered to the total tumor mass while the surrounding tissue is left completely unaffected [40]. The therapeutic efficiency of MH mainly depends on the thermal conversion efficiency of the MNPs themselves. Subsequently, also in this application several modifications concerning particle size, shape, composition, etc. are necessary in order to reach

enhanced induction heat properties. However, the still rather shallow understanding of magnetic hyperthermia limits the speed of scientific progress in this field. Currently, MH is mainly exploited in a combinatorial manner with traditional cancer treatments like chemo- or radiotherapy in order to increase the sensitivity and efficiency of those methods [52].

Almost certainly, the full range of application possibilities of magnetic nanoparticles has not been discovered yet and a large amount of research is still required to explore the full potential of magnetic nanoparticles. In this master thesis, magnetic nanoparticles were applied in preliminary experiments that aim to study a novel technique of producing an ischemic chronic wound in skin in order to establish a reliable wound free model for the study of chronic wounds and ischemia.

Aim of the study

The present master thesis focuses on the establishment of a novel ischemic wound model that uses superparamagnetic nanoparticles to alter the blood flow in micro capillaries. This approach represents a new, well controllable method for researching ischemic chronic wounds.

Since ischemia is primarily caused by vascular complications, the supply of oxygen, nutrients and circulating cells, to the wound site, is limited and thereby the healing response is severely impaired [53]. A reliable ischemia model that enables the study of the relation and effects of ischemia and chronic wounds is still missing. Research in that area is currently limited by a number of complicating factors. Firstly, model systems capable of mimicking human wound healing are absent. In most of the already available models, small animals (mouse, rat, etc.) are used, even though they exhibit physiological characteristics that are completely contrary to those of humans. Pig skin, in contrast, resembles human skin anatomically as well as physiologically. They share similar patterns of blood vessels and hair follicles, have a comparable dermal elastic content and their molecular and physiological response to various growth factors resembles as well [53], [54].

Another big obstacle hindering research design in the establishment of a reliable ischemia model is the fact, that there is currently no satisfactory method to reproduce an ischemia without surgical intervention. Already established invasive methods, such as the skin flap model, require surgical skills. They entail an own response, that has an impact on the internal inflammation parameters. This would interfere or even override the effects secondary to ischemia, the actual research subject [53].

The goal of an ongoing study of the research centre JOANNEUM RESEARCH COREMED is the development of an ischemia model that allows precise spatiotemporal control, but without the need of surgical intervention. This occlusion should be achieved via neodymium-iron-boron (NdFeB-) magnet-mediated aggregation of specific superparamagnetic nanoparticles within defined microcapillaries. To be able to establish such an innovative model, preliminary tests that give an estimation on process relevant parameters, such as the strength of the applied magnet and guarantee the principle feasibility of the method, were necessary. In addition, a detailed analysis of the porcine skin in the region of interest is needed. Consequently, the following master thesis focuses on the detection and identification

of location related variations in the structure and composition of porcine skin on a histological, as well as molecular level. In a second part, a novel *in vitro* and *ex vivo* magnetic nanoparticle-based ischemia model was designed, constructed, and tested, that aimed to evaluate the potential of the method.

Anatomical site differences

Materials and Methods

Porcine skin is a commonly used model for human skin injury and wound healing research. It is a well-known fact that there are many remarkable similarities between porcine and human skin that justify the utilization of porcine tissue for scientific purposes. However, previous studies have shown that regional anatomic variations, which are present in human skin, are also present in porcine skin [55].

The objective of the following study was to evaluate the structure of porcine skin from 16 different anatomic regions along the back of three domestic pigs. The biopsies were collected from the dorsal/superior side of the pigs' trunk. Four times four biopsies in a row were taken that covered the two cranial regions: upper neck/cervical region and thoracic region; and the two caudal regions: lumbar region and sacral region. The positions can be further classified into eight inner biopsies placed next to the spine (medial) and eight outer biopsies that were further lateral sited.

Figure 4 gives an overview over the distribution and location of the 16 examined positions. At each position, biopsies with a diameter of 8 mm were taken, and histological as well as molecular biological (gene expression) evaluation was performed.

This part of the study aims at highlighting the importance of appreciating regional differences to avoid misinterpretation of experimental results when using porcine skin as a human analogue in research.

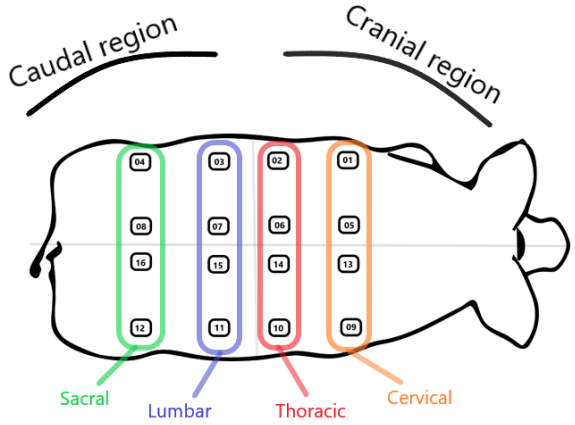

Figure 4: Distribution and location of the 16 examined positions along the pigs` trunk.

Biopsies

Skin samples were collected from three female domestic pigs, *sus scrofa*. At the time of the experiment each pig had an average age of 10 weeks. **Table 1** gives information on the bodyweight of the animals.

Table 1: Animal data: *domestic pigs 1-3. Bodyweight [kg]*

Animal	Bodyweight [kg]
Pig 1	19
Pig 2	17,5
Pig 3	18,5

Histological evaluation

Morphometric analysis was performed on paraffin embedded tissue sections. After removing 8 mm biopsies for histology, the samples were placed in embedding cassettes and immediately stored in formalin-filled containers. After 24 hours, they were transferred into new containers containing 70% ethanol and stored in the fridge (4°C) until further processed by hematoxylin and eosin staining. The stained biopsies were then digitalized for data analysis and skin thickness measurement. For this purpose, the software *Aperio ImageScope* (Leica Biosystems, Wetzlar, Germany), a pathology slide-viewing platform, was used. For the calibration of the scale bar, the spatial calibration tool of the software *Image J* was applied. **Figure 5** refers to a representative histological biopsy showing a stained and digitalized visualization of the epidermis, dermis and part of the adjacent hypodermis (subcutis).

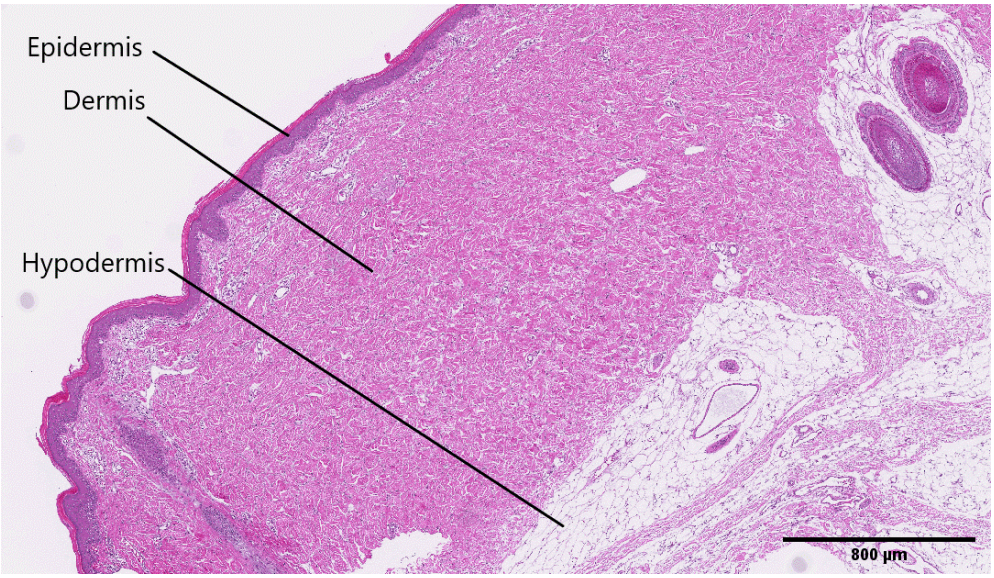

Figure 5: Exemplary illustration of an H&E- stained and digitalized biopsy using the softwares Aperio ImageScope and ImageJ. *The different layers of the skin (dermis, epidermis, and part of the adjacent hypodermis (subcutis)) are well visible.*

In the measurement of the epidermis both, living and non-living epidermis (Stratum corneum), were included in the measurement. In **Figure 6** a representative depiction of such an epidermis measurement using the software *Aperio ImageScope* is shown. The distances were measured at multiple positions and the average value was calculated. In all the samples, the staining and visualization of the epidermis enabled the identification of the individual layers: Stratum corneum, Stratum lucidum, Stratum granulosum, Stratum spinosum, Stratum basale (**Figure 7**). However, the stratum lucidum and stratum granulosum were less distinct.

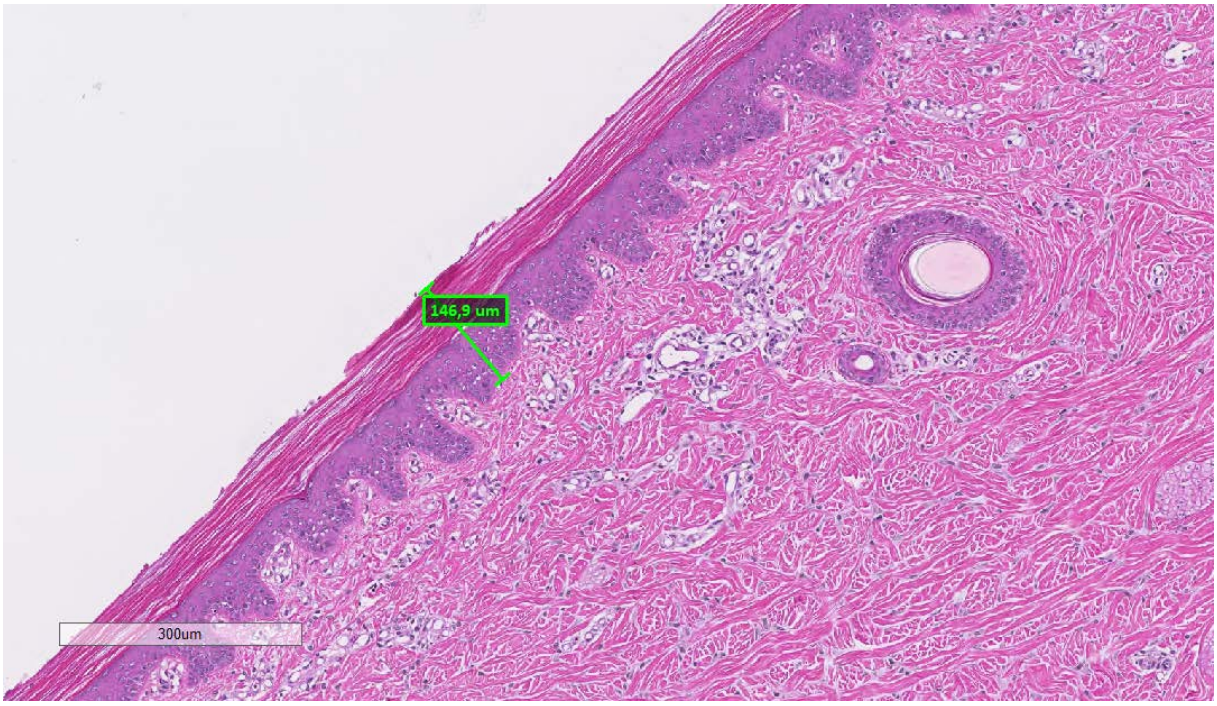

Figure 6: Measurement of the epidermis thickness using the software Aperio ImageScope*. For further calculations the distances were measured at multiple positions and the average value was calculated.*

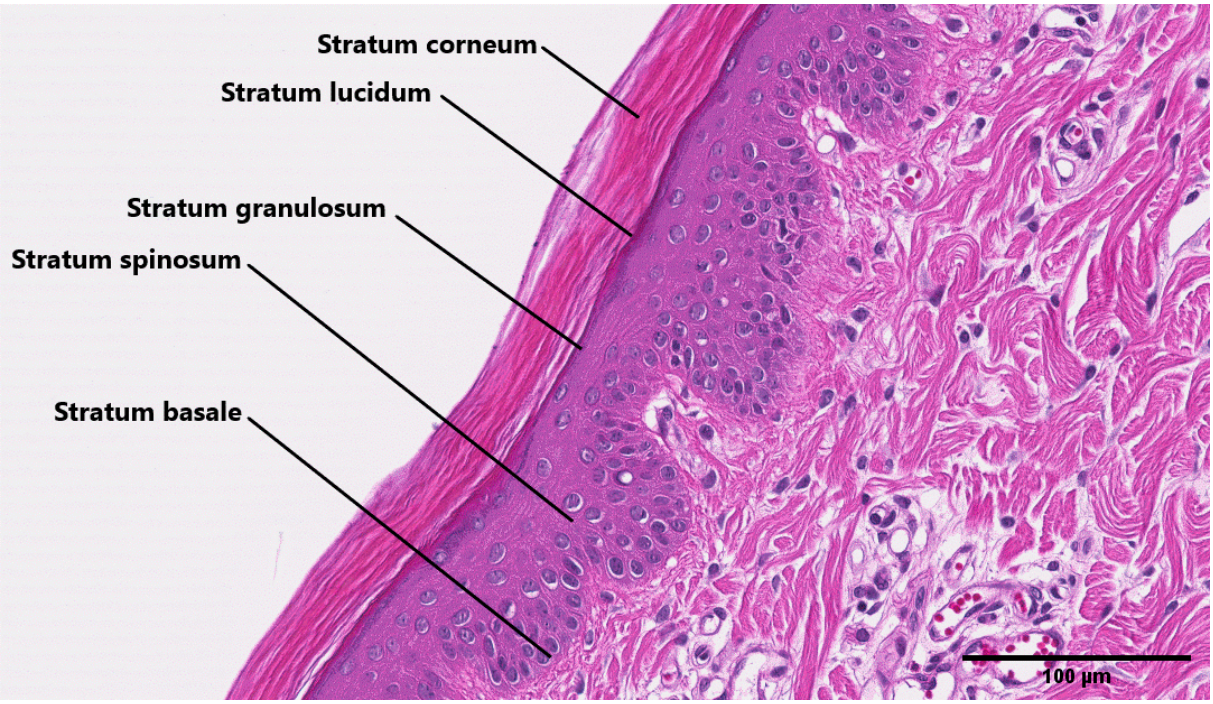

Figure 7: Layers of the epidermis: *stratum corneum, stratum granulosum, stratum spinosum, and stratum basale.*

Ultrasonic analysis

Next to the histological evaluation, the thickness of the second skin layer, the dermis, was additionally measured using ultrasound. By this, not only a second analysis method was provided, but also the accuracy of employing ultrasound in the measurement of the porcine dermis was investigated.

The dermis' thickness at the 16 locations was measured by 22 MHz Skin ultrasound using the device GE healthcare ultrasonic LogiQe R6 with R10-22-RS Linear Probe (Int.Nr.: G0240,G-0241).

Molecular evaluation

Furthermore, molecular evaluation via gene expression analysis was performed. Similar to the procedure described above, 16 biopsies were examined. Firstly, RNA isolation was performed, followed by the transcription into cDNA using the enzyme *reverse transcriptase* (RT) and subsequently amplification and analysis thereof via real-time/ quantitative polymerase chain reaction (qPCR). The aim of this part of the study was the detection and identification of location related differences in the transcription levels of certain genes related to important skin structures as well as to skin development and inflammation processes.

RNA isolation

The biopsies were collected from the same positions and animals as described above (**Table 1, Figure 4**). The biopsies were placed in 1.8 ml cryotubes, weighed and snap frozen in liquid nitrogen. Until homogenization, the biopsies were stored in a freezer at – 80 °C. Homogenization was achieved using the benchtop instrument *MagNA Lyser* (Roche Diagnostics; Product No.: 03358968001; Vienna, Austria) and the respective MagNA Lyser Green Beads (Roche Diagnostics; Product No.: 03358941001; Austria). The biopsies were transferred into the precooled beads-containing lysis tubes and 700 µl QIAzol Lysis Reagent (© QIAGEN; Cat No./ID: 79306) was immediately added. The samples were then placed in the *MagNa Lyser* device and homogenization was performed at 6500 rpm for 35 seconds (3 cycles). The remaining procedure of purification of total RNA was conducted as described in the RNeasy Lipid Tissue Mini Kit from QIAGEN. The yield of the isolated RNA was then quantified by measuring the absorbance (ABS) at 260 nm in a nanodrop spectrophotometer (NanoDrop™ One/OneC Microvolume UV-Vis Spectrophotometer; Thermo Scientific™).

cDNA

For the synthesis of cDNA the enzyme *reverse transcriptase* was used. Therefore, a total mass of 1 µg of the isolated RNA was mixed with nuclease-free water as well as with 4 µl of the iScript™ Reverse Transcription Supermix (Bio-Rad Laboratories GmbH; Cat No.:1708840; Germany) to reach a total volume of 20 µl, as given in **Table 2.** The reaction was run in the MiniAmp™ Thermal Cycler (Applied Biosystems™; Cat No.: A41195; Austria) according to following reaction protocol:

- 5 minutes at 25°C (room temperature)
- 30 minutes at 42°C
- 5 minutes at 85°C
- Hold at 4°C (optional)

Table 2: Components of the cDNA-synthesis reaction mixture. *A total mass of 1 µg RNA template was mixed with the required volume of nuclease-free water to reach a volume of 16 µl. Finally, 4 µl of the enzyme-containing iScrip Supermix solution was added.*

Component	Volume per reaction
iScript Supermix	4 µl
Nuclease-free water	X µl
RNA template (1µg Total RNA)	X µl
Total volume	20 µl

The received cDNA was then stored in a freezer at - 20 ° C until qPCR was performed.

qPCR

Real-time quantitative PCR (qPCR) describes the simultaneous amplification and detection of nucleic acids using the polymerase chain reaction (PCR). The detection is achieved by including a fluorescence molecule into the reaction that reports the increase in the amount of DNA with a proportional increase in fluorescence signal. This signal is then monitored by specialized thermal cyclers that are equipped with fluorescence detection modules. The generated fluorescence is a measure for the amplified amount of product in each cycle. In this project the instrument CFX384 Touch Real-Time PCR Detection System (Bio-Rad Laboratories GmbH; Cat No.: 1855484; Germany), which is providing a 384-well format, was used [56].

Components of the reaction mixture included: the TaqMan Gene Expression MasterMix (Applied Biosystems; Austria) as well as the for each gene individual probe assays (PrimePCR™ Probe Assays; Bio-Rad Laboratories, Inc.; California, United States), which are listed in **Table 23** in the Appendix section. The reaction volume for each individual reaction was 10 µl. The mixing ratio and the amounts of the individual components are given in **Table 3**.

Table 3: Components and mixing ratio of the qPCR reaction mixture*. The amounts given refer to the amounts needed for one reaction (=1rxn).*

Component	Volume per reaction
TaqMan Gene Expression Master Mix (2x)	5.0 µl
TaqMan Assay (20x)	0.5 µl
cDNA template	2 µl
Nuclease-free water	2.5 µl
Total PCR reaction mix volume	10 µl

In total, twelve genes were analyzed and each gene was measured in duplicates. Every individual PCR reaction mixture was placed in a single well of a 384-multiwell

plate. The PCR reaction was run in the CFX384 Touch Real-Time PCR Detection System according to the following PCR standard thermal protocol (**Table 4**).

Table 4: PCR standard thermal protocol. *The PCR reaction was conducted within 40 cycles of alternating denaturing and annealing steps subsequent to an initial polymerase activation phase.*

Polymerase activation [2]	PCR (40 cycles)	
Hold 95°C	Denature 95°C	Anneal / extend 60°C
10 minutes	15 seconds	60 seconds

Data analysis was performed using the device-associated software CFX Maestro Software for CFX Real-Time PCR Instruments (Bio-Rad Laboratories, Inc.; Hercules, CA).

Relative gene expression was calculated using the delta-delta-Cq method, normalizing target gene expression to the averaged Cq of the endogenous control gene (ß-Actin (ACTAB)) and calibrating all samples to a blank skin sample (Biopsy position 05 of pig 1). N-fold expression levels are presented as mean values with the respective standard deviation.

Statistical Analysis

For all quantitative assays, as well as for the histological and ultrasonic evaluation, for which data passed tests for normality, one-way ANOVA was performed to determine differences between the sample sites cervical, thoracic, lumbar and sacral, with and without further classification into four lateral and four medial positions. Regarding only the lateral and medial positioning, a paired t-test was performed to compare the differences of those two body sites. Where data failed tests for normality, a Friedman test was conducted. P-values < 0.05 were considered as statistically significant with *, **, *** indicating $p < 0.05$, $p < 0.01$, and $p < 0.001$, respectively. All tests were performed using GraphPad PRISM Software (2021 GraphPad Software Inc; San Diego, CA).

Results

Histology

Comparison of the three individual pigs

A comparison of the average skin thicknesses of the three individual pigs (**Table 5**) revealed that pig 1 had the greatest skin thickness, followed by pig 3. Pig 2 measured the thinnest average skin thickness. The results indicate a correlation between the bodyweight/size of the pigs and their skin thickness. The animal with the highest body weight (pig 1; **Table 1**) also reached the maximum value in the skin measurements. Equally, pig 2 showed the lowest body weight and the thinnest skin tissue. Pig 3 reached the intermediate values concerning both points.

Pig 2 achieved the highest value in the measurement of the epidermal thickness. While pig 1 and pig 3 almost showed identical epidermal thicknesses, pig 2 exhibited a higher value.

Table 5: Comparison of the average cutis, dermis and epidermis thicknesses of the individual pigs 1-3.

	Cutis [µm]	**Dermis [µm]**	**Epidermis [µm]**
Pig 1	**1974** ± 219	**1874** ± 220	**104** ± 20
Pig 2	**1904** ± 350	**1775** ± 352	**120** ± 27
Pig 3	**1938** ± 334	**1818** ± 320	**103** ± 19

Overall cutis, dermis and epidermis thickness

For all the following evaluation and data interpretation, the measured values of the pigs were averaged. Since three pigs were used, the following data's total number of responses is three (n=3).

The measurement of the skin at all positions revealed an average cutis thickness of 1938 ± 218 µm and a mean dermis thickness of 1822 ± 214 µm. The epidermis measured, according to our results, an average distance of 108 ± 12 µm. The results of the individual measurements at each position depicted in **Table 16-18** (Appendix).

Comparison of cranial and caudal regions

The 16 positions along the pigs' trunk were categorized into four subgroups to better identify location-related differences. Therefore, a separation into two cranial regions

(cervical and thoracic) and two caudal regions (sacral and lumbar) was employed. Each of the four subgroups covered four positions (from the right to the left lateral side). For a better illustration, the respective positions have been marked in individual colours, as shown in **Figure 8**. Also in the tabular representation of the data, the respective regions are highlighted in the according colour.

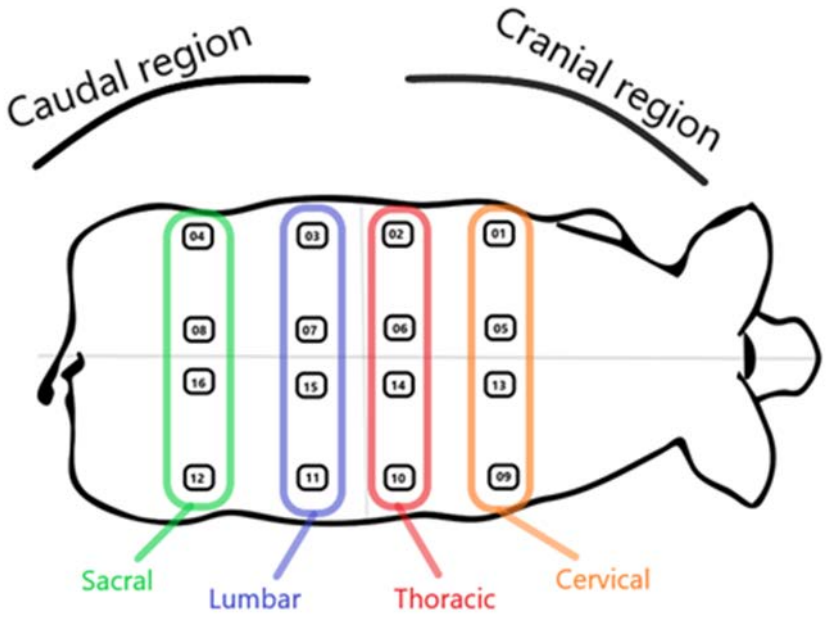

Figure 8: Categorization of the 16 positions into four subgroups (cervical, thoracic, lumbar and sacral) for a better identification of location-related differences.

The values of the cutis' thickness varies between 2082 µm and 1833 µm; those of the independent dermis measurement between 1956 µm and 1730 µm and those of the epidermis measurement between 118 µm and 102 µm.

The data analysis revealed that the greatest thickness is given in the sacral region of the pigs' trunk. The determination of the cutis thickness, as well as the independent dermis and epidermis measurement, led to this outcome. The second greatest distance was measured at the cervical region, which refers to the very cranial area. The two inner regions, thoracic and lumbar, exhibited in all three cases very similar values. **Figure 9** refers to the average results at each region (n=12).

Tables 19, 20 and 21 (in the Appendix section) give the results of the cutis, dermis and epidermis measurement at each individual position (Pig 1-3; 1-16).

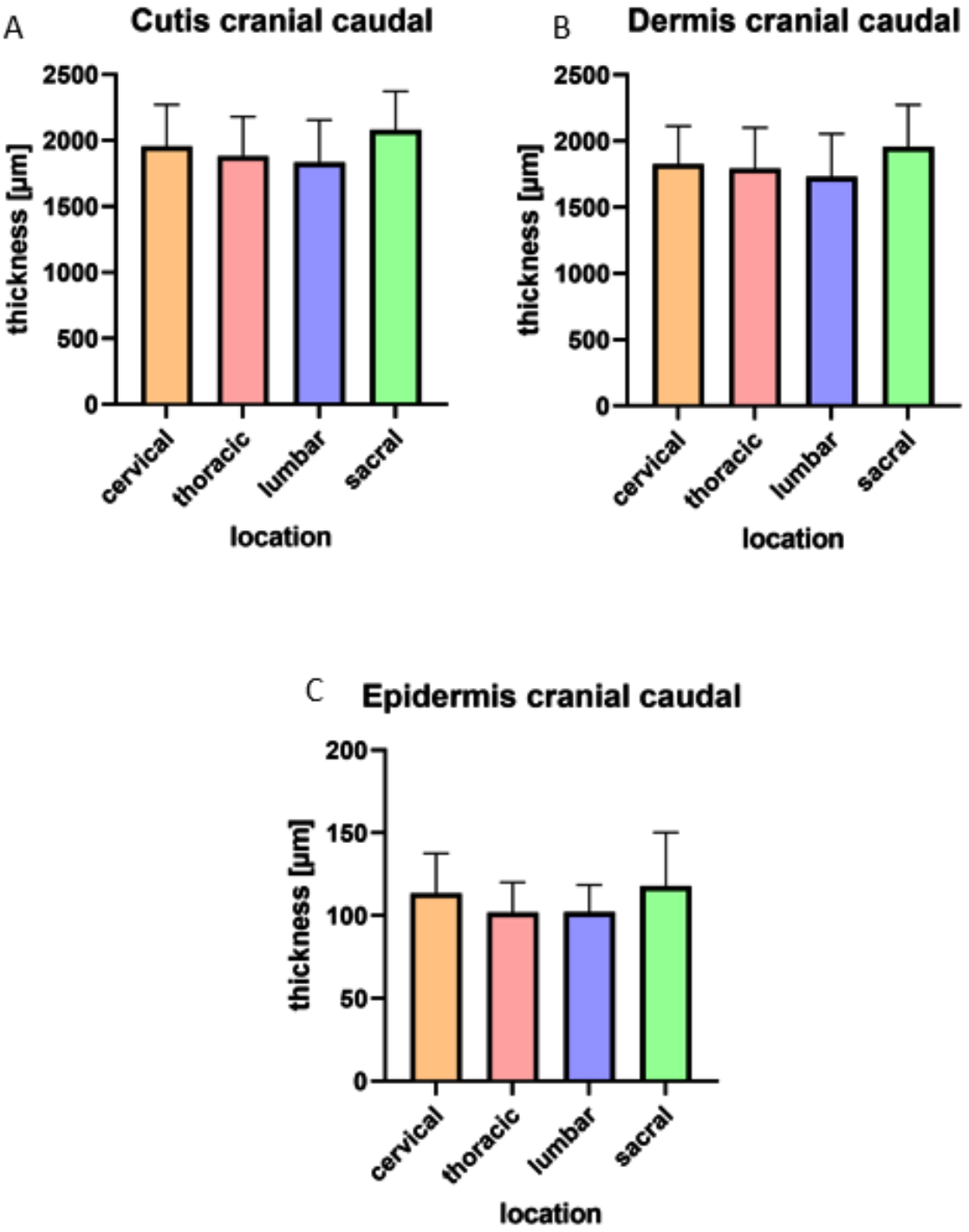

Figure 9: Graphical representation of the average values (mean with SD) of the cutis (A), dermis (B) and epidermis (C) thickness at cervical, thoracic, lumbar and sacral positions*. The greatest skin thickness was given at the sacral region, followed by the cervical region. The two inner sites, thoracic and lumbar, measured smaller distances. The measurement of the epidermis revealed the same trend (P-values ≥0.05).*

Comparison of the lateral and medial positions

In addition to categorizing cranial and caudal positions, a separation based on the horizontal location was included in the analysis. Therefore, the 16 examined biopsies were divided into eight lateral and eight medial positions (**Figure 10**).

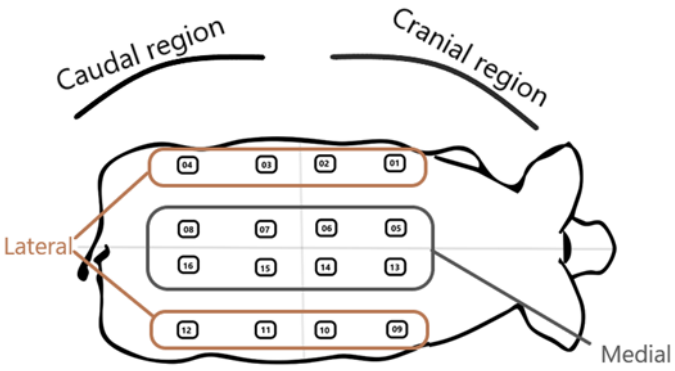

Figure 10: Graphical representation of the categorization into eight lateral and eight medial positions.

The medial positions are located in close proximity either on the left or on the right side of the pigs' spine. The lateral positions are further apart from the spine and approximating the ventral/dorsal region.

Figure 11 depicts the direct comparison of the lateral and medial sites. The analysis of the cutis, as well as the independent dermis measurement, revealed a significantly higher thickness at the lateral positions (P-value<0.05). The differences in the distances are more significant in this context than in the comparison of the caudal and cranial regions. Whereas the skin's thickness was at an average value of 2100 µm at the lateral site, the medial site's average value only reached 1777 µm. In contrast, the epidermis' thickness does not seem to be influenced by the horizontal location. The difference between the two average values obtained in the epidermis measurement is less than it is concerning the values obtained for the dermal part. Furthermore, the highest thickness of the epidermis was not identified at the lateral, but at the medial site. This contradicts the results of the cutis and dermis measurement.

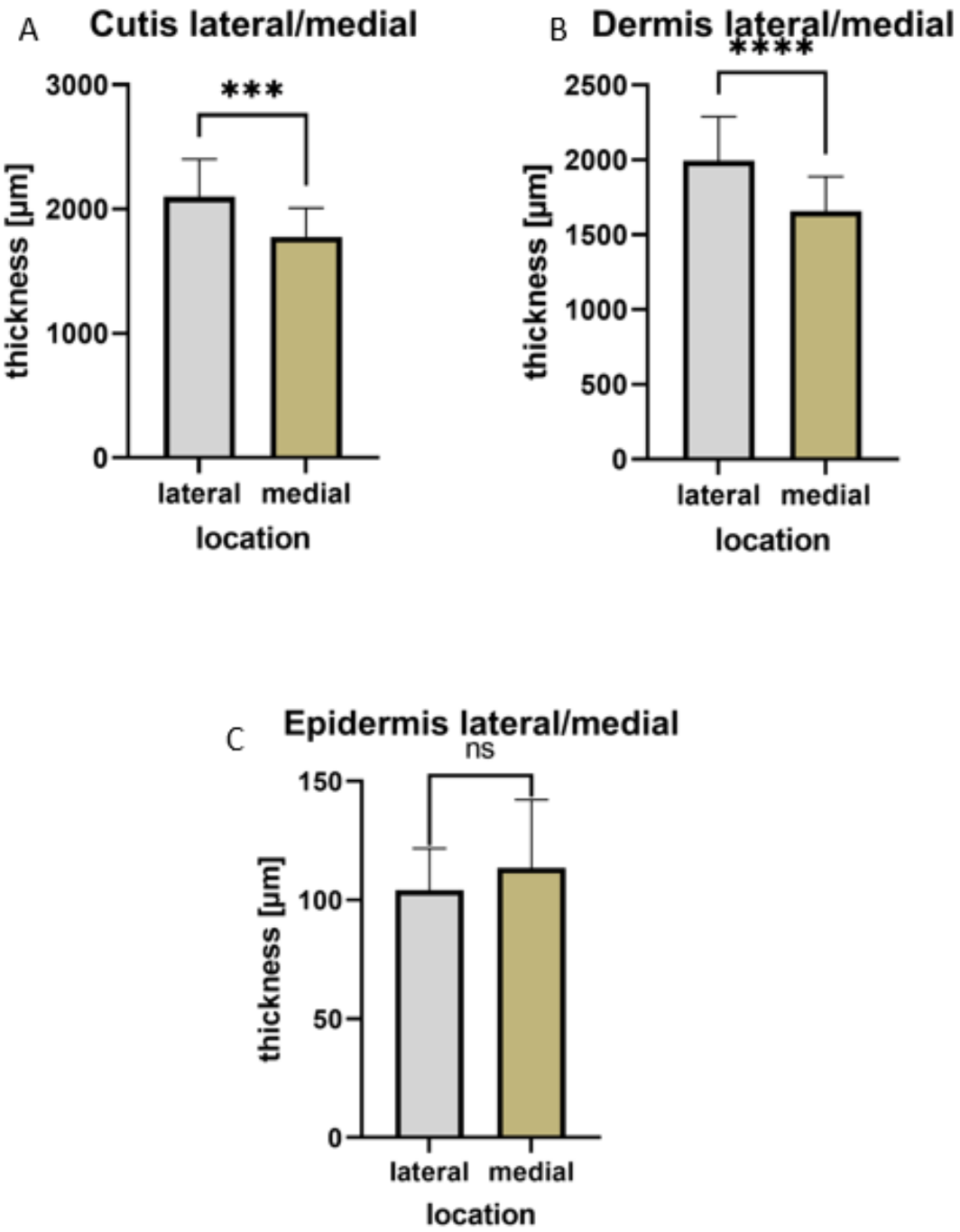

Figure 11: Graphical representation of the direct comparison of the lateral and medial sites. *The mean values with SD of the cutis, dermis and epidermis measurement are depicted. The thickness of the cutis* ***(A)*** *(P-value = 0.0002) and dermis* ***(B)*** *(P-value < 0,0001) was significantly increased at lateral sites compared to medial sites. The epidermis measurement* ***(C)*** *revealed the opposite trend (P-value > 0.05).*

Detailed analysis including caudal/cranial and lateral/medial positioning

In the following figure (**Figure 12**), both parameters (caudal vs cranial and lateral vs medial) were similarly included in the evaluation. According to the results of the measurement of the cutis thickness as well as the independent dermal thickness, the

greatest distances are always given at the lateral sites. The smallest distance of all lateral sites (lumbar region; 1965 µm) still exceeds the highest value obtained at the medial sites (sacral region; 1904 µm). The same situation holds true regarding the epidermal-independent dermis measurement (lateral-lumbar; 1866 µm vs. medial-sacral; 1762 µm).

The outcome of the epidermis measurement displayed a different situation. In this case, the maximum value was not reached at a lateral, but at a medial site (sacral; 128 µm), whereas the minimum value was identified at the lateral-lumbar position (97 µm). In general, all of the four medial sites exhibited a greater epidermal thickness than the respective lateral sites. Nevertheless, the order sacral over cervical, followed by thoracic and lumbar, remained the same.

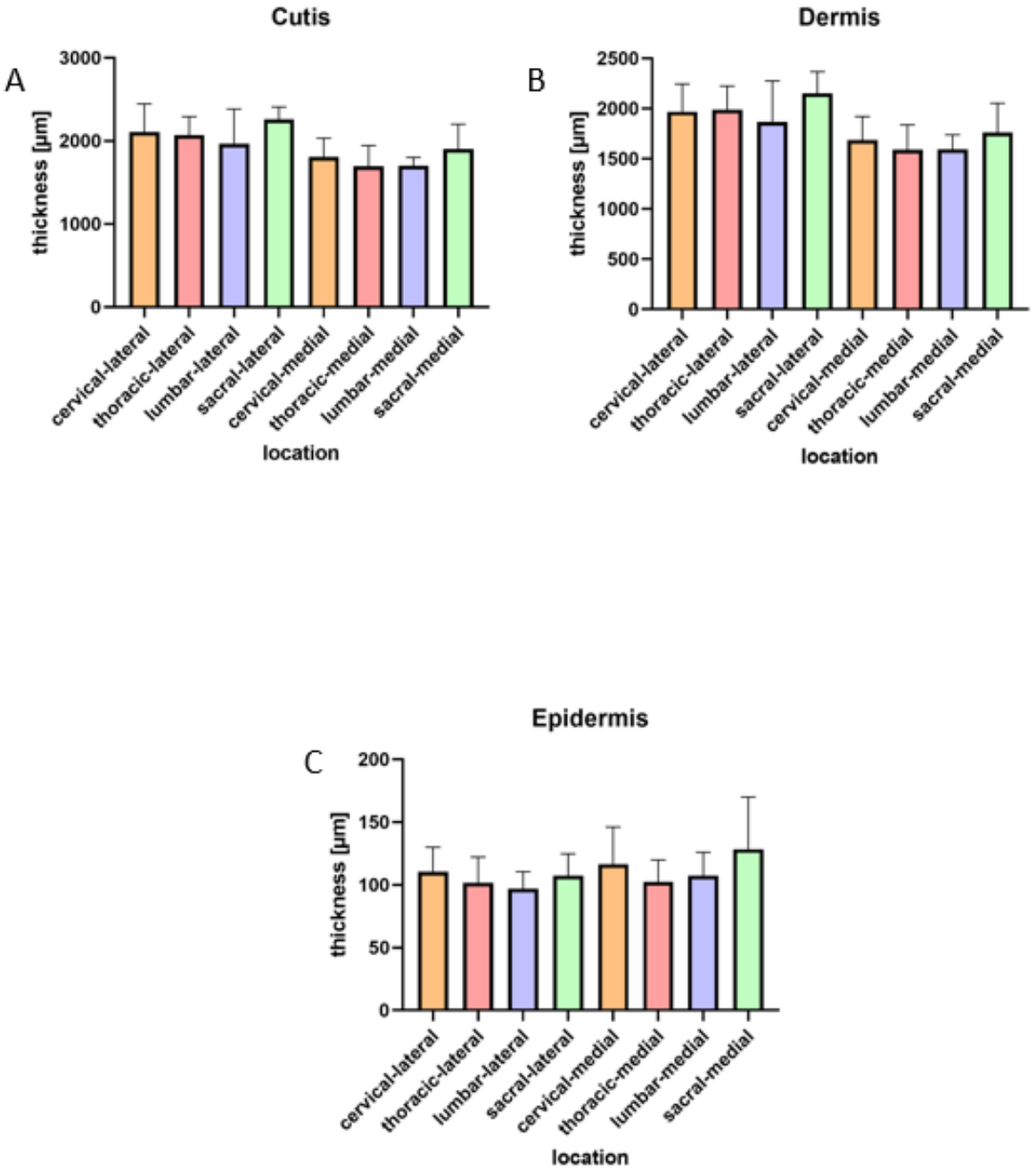

Figure 12: Average thickness (mean with SD) of the porcine cutis (A), dermis (B) and epidermis (C) [µm] in respect to the lateral/medial and caudal/cranial sites (n=6). Significant differences were identified concerning *the thicknesses of the cutis (P-value = 0.05) and the dermis (P-value = 0.011). The greatest distances were always measured at the lateral sites. The epidermis measurement revealed an opposite trend (P-value ≥ 0.05). All of the four medial sites exhibited a greater epidermal thickness than the respective lateral sites.*

Ultrasonic evaluation

The measurement of the dermis thickness using an ultrasonic device revealed a mean dermis thickness of 1394 ± 318 µm. The greatest skin thickness was achieved by pig 1, followed by pig 3. Pig 2 showed the thinnest dermis thickness (**Table 6**). In general, the values of the ultrasound based dermis measurement lay between 2239 µm and 791 µm.

Table 6: Average dermis thicknesses of the three individual pigs. *Measurement was conducted using an ultrasound device.*

	Pig 1 [µm]	**Pig 2 [µm]**	**Pig 3 [µm]**
Average dermis thickness	1562	1109	1511
Std. dev.	252	166	300

The 16 positions along the pigs' trunk were again categorized into four subgroups including the regions cervical and thoracic (cranial), as well as, sacral and lumbar (caudal; **Figure 8**). The ultrasound based dermis measurement revealed that the greatest thickness was given in the thoracic region of the pigs' trunk. The second greatest distance was measured at the lumbar region, followed closely by the sacral area. The thinnest dermis thickness was detected at the cervical region, which refers to the very cranial area. **Figure 13** refers to the average results at each region (n=12);

The comparison of the lateral and medial positions (**Figure 10**) revealed that, according to the results obtained in the US measurement, the medial regions showed a higher dermis thickness than the lateral ones. Whereas the dermis thickness reached an average value of 1516 ± 151 µm at the medial site, the lateral site's average value only measured 1272 ± 73 µm (**Figure 13**).

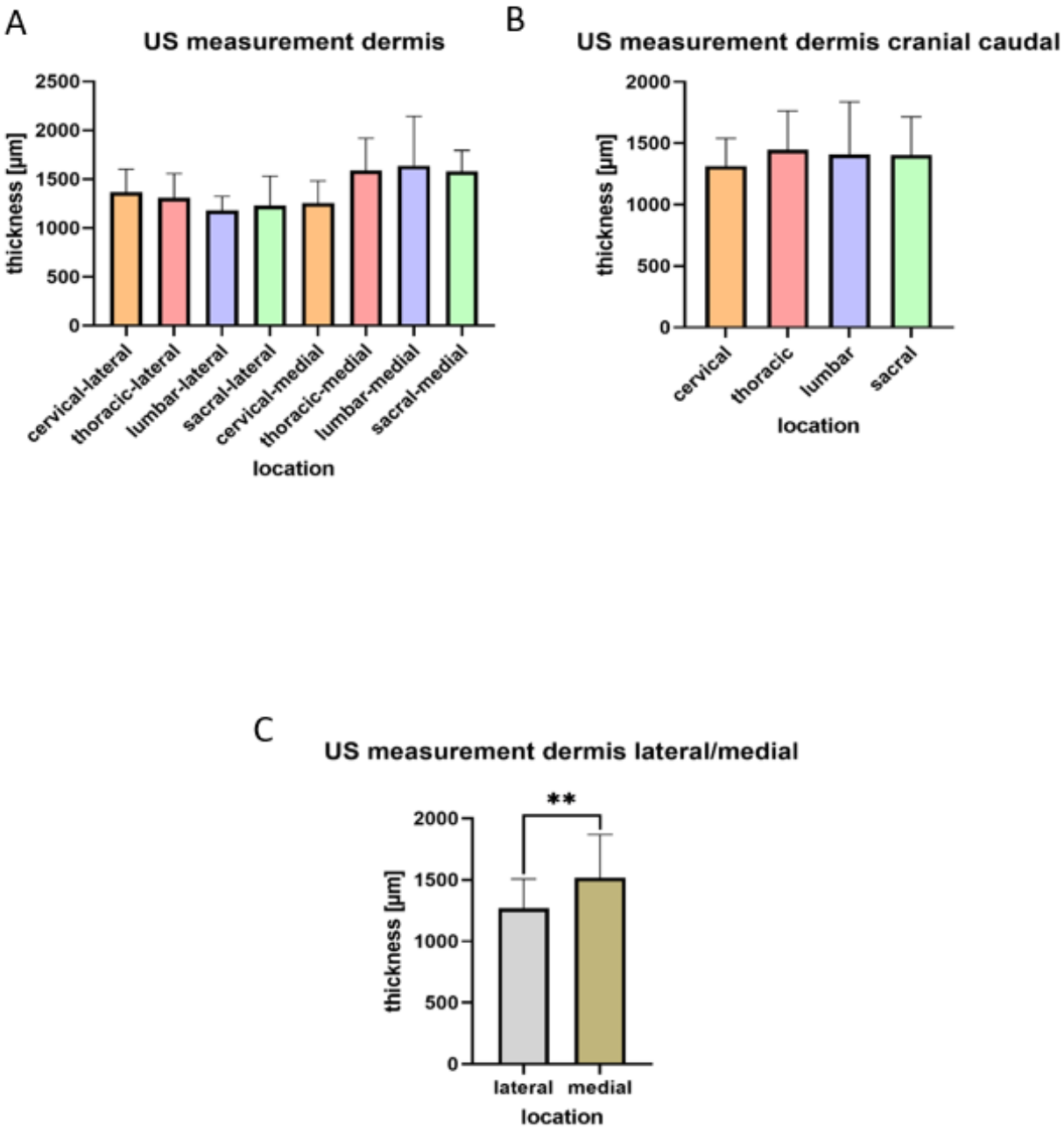

Figure 13: Graphical representation of the results of the porcine dermis thickness measurement using ultrasound (mean with SD)*. **(A)** Categorization into cervical, thoracic, lumbar and sacral, as well as into lateral and medial positions, was performed. **(C)** The medial sites measured significantly larger distances than the respective lateral sites (P-values < 0.05). **(B)** Concerning the caudal and cranial positions, the measurement revealed a decrease in thickness in the following order: thoracic, lumbar, sacral and cervical (P- values > 0.05).*

Table 22 (in the Appendix section) gives the results of the dermis measurement using ultrasound at each individual position (Pig 1-3; 1-16).

Molecular evaluation

In the molecular evaluation, the expression of certain genes was investigated to detect potentially present location-related differences in their expression levels. Therefore, gene expression assays of genes crucial in the development of skin structures and in wound healing processes were conducted. The factors analyzed, included: the *inflammatory mediator interleukin IL1B* and *C-X-C motif chemokine ligand 8* (*CXCL8*; former *IL8*); the angiogenesis markers *vascular endothelial growth factor alpha* (*VEGFA*) and *fibroblast growth factor 2* (*FGF2*); as well as the growth factor *cell motility protein actin alpha 2, smooth muscle* (*ACTA2*) and the hypoxia and blood circulation associated transcription factor *HIF1A* (*hypoxia inducible factor 1 subunit alpha*). The *fatty acid-binding protein 4 (FABP4)* that is mainly expressed in adipocytes and macrophages was also included in the evaluation [57]. Furthermore, *Keratin 5* as a marker for keratinocytes; and *CD209* and *CD14* representing markers of inflammatory monocyte-derived cells, either dendritic cells or macrophages, were considered in the analysis [1]. Moreover, as an additional factor that is associated with wound healing and angiogenesis, *Leptin (LEP)* was analyzed and to also include another endothelial marker, the *platelet-endothelial cell adhesion molecule-1* (*PECAM-1*, also known as *CD31*) was added.

The gene expression analysis revealed that the expression of the *Vascular Endothelial Growth Factor A (VEGFA)* was significantly increased at lateral sites compared to medial sites (P-value= 0.0137), as shown in **Figure 14**. Regarding the cranial/caudal location, no significant differences in the expression levels of *VEGFA* were detectable. However, a trend established. The expression of the vascularization gene was the highest in the cervical region, followed by the lumbar and sacral region. In the thoracic area, the expression was detected to be the lowest. The results are depicted in **Figure 14**.

The expression of the wound healing associated transcription factor *HIF1a* showed the same trend (P-value≥0.05), regarding the horizontal location. The expression level was higher at the lateral than at the medial site. However, the measured difference in the expression levels was minor. Concerning the categorization into cranial and caudal locations, the results indicate that the expression was the greatest in the lumbar, and the most minor in the thoracic region. However, the differences were again small and the values at all four positions very similar. The results are depicted in **Figure 14**.

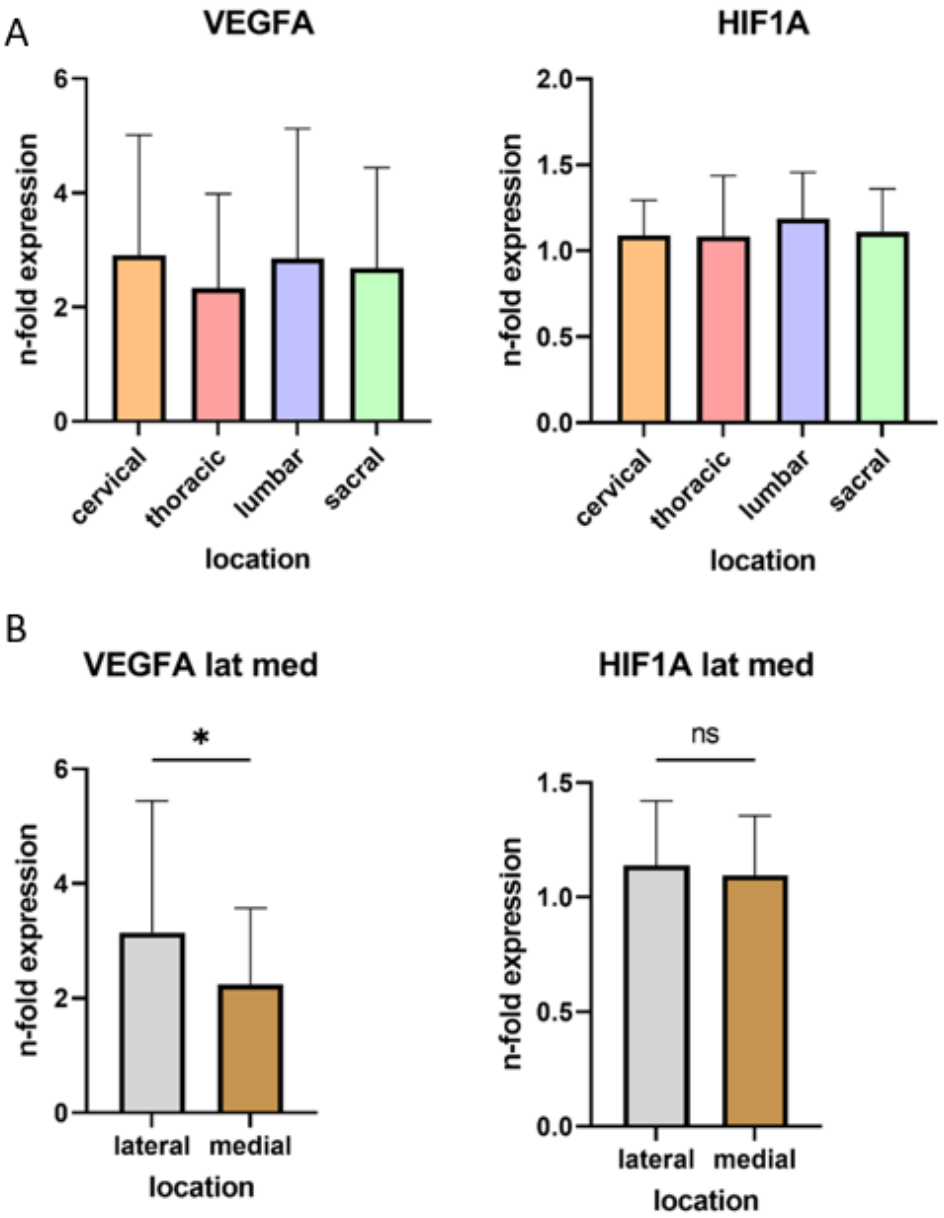

Figure 14: n-fold expression of VEGFA and HIF1A at (A) cervical, thoracic, lumbar and sacral sites, as well as at (B) lateral and medial sites (mean with SD). *Expression of VEGFA was significantly increased at lateral sites (P-value = 0.0137), whereas* no significant difference between lateral and medial sites was detectable in the expression level of HIF1A (P-value ≥ 0.05; with lat med for lateral medial). *Expression of VEGFA was the greatest at the cervical region, followed by the lumbar and sacral area. The expression levels of HIF1A were similar at all four locations.*

Similar to *VEGFA*, the *fibroblast growth factor 2* (*FGF2*) showed a significant higher expression at the lateral positions than at the medial ones (P-value = 0.0014). In contrast, the expression of the actin protein *ACTA2* did not show significant differences in the expression levels in relation to the lateral and medial location. (P-value ≥ 0.05).

Regarding the differences in the expression levels at cervical, thoracic, lumbar and sacral sites, those two genes showed varying trends. The expression maxima of *FGF2* was measured in the cervical area. In the lumbar region, the expression was the second highest. The lowest expression level of *FGF2* was identified in the thoracic region. Also *ACTA2* was the least expressed in this area. However, the highest expression of *ACTA2* was given in the lumbar region. The n-fold expression of the two genes in graphic form is given in **Figure 15**.

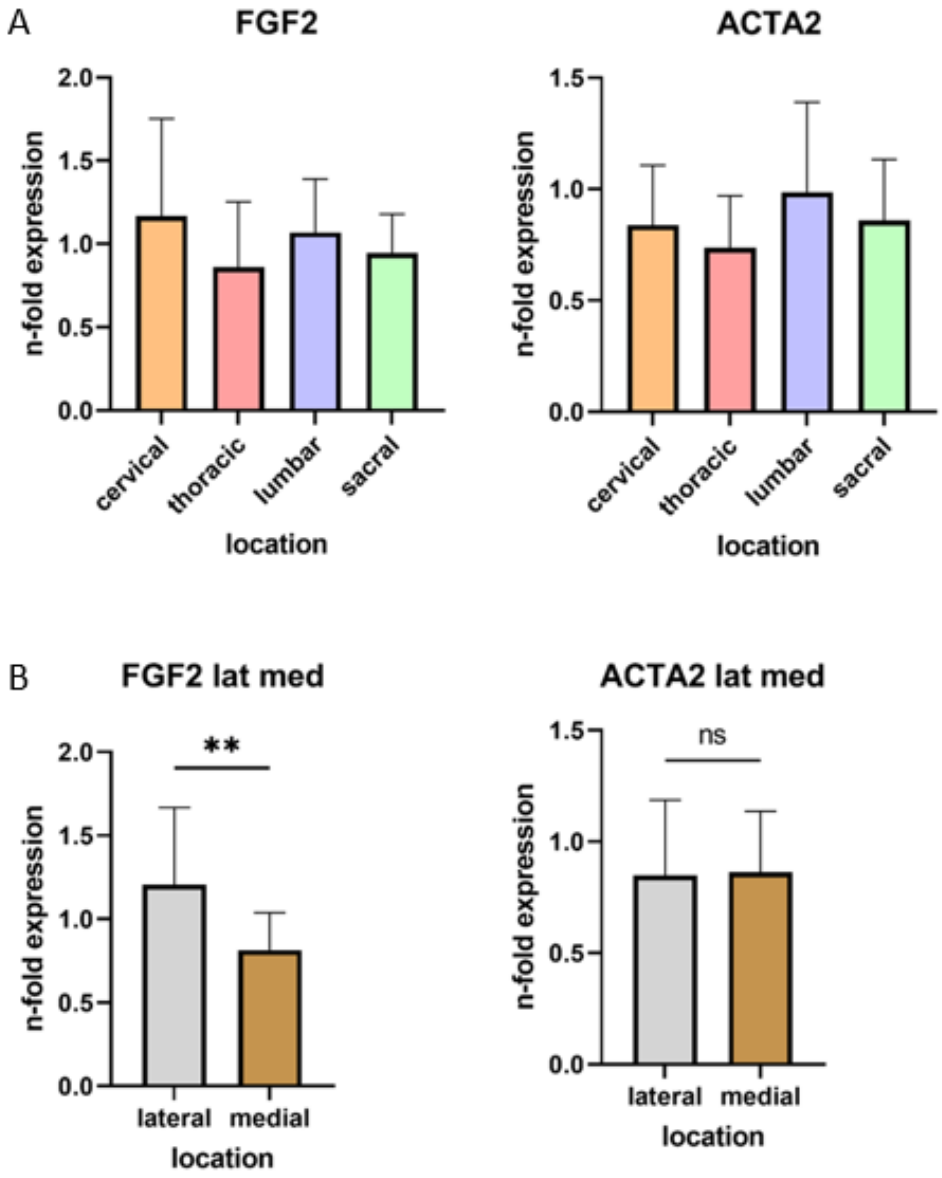

Figure 15: n-fold expression of FGF2 and ACTA2 at (A) cervical, thoracic, lumbar and sacral sites, as well as at (B) lateral and medial sites (mean with SD). *Expression of FGF2 was significantly increased at lateral sites (P-value = 0.0014), whereas no significant difference between lateral and medial sites was detectable in the expression levels of ACTA2 (P-value ≥ 0.05). Expression of FGF2 was the greatest at the cervical region, followed by the lumbar and sacral area. Also the expression of ACTA2 was the lowest in the thoracic region. However, the maximum expression was detected in the lumbar area. Expression of ACTA2 in the cervical and sacral region was almost identical.*

In addition to those four genes, the expression of the *fatty acid binding protein 4* (*FABP4*) was also analyzed. The results indicate a significantly increased gene expression in the lateral areas of the pigs' trunks (P-value = 0.0002). Regarding the cranial/caudal location, data analysis revealed the highest gene expression at the lumbar site. The expression levels at the sacral and cervical site exhibited similar

values, whereas the minimum expression was again measured in the thoracic region. (P-values ≥ 0.05). This trend accords with the expression pattern obtained for the genes *HIF1A* and *ACTA2*. **Figure 16** refers to the results of the gene expression analysis of *FABP4*.

The expression of the keratinocyte marker *KRT5 (Keratin 5)* did not show a significantly different expression pattern, neither at lateral and medial sites, nor at cranial and caudal ones. The values obtained at the lateral and medial positions were almost identical and also in the cervical, thoracic, lumbar and sacral region the differences were minor. The expression minimum was again identified in the thoracic area, whereas the maximum expression was measured in the lumbar area. The n-fold expression of *KRT5* is given in **Figure 16**.

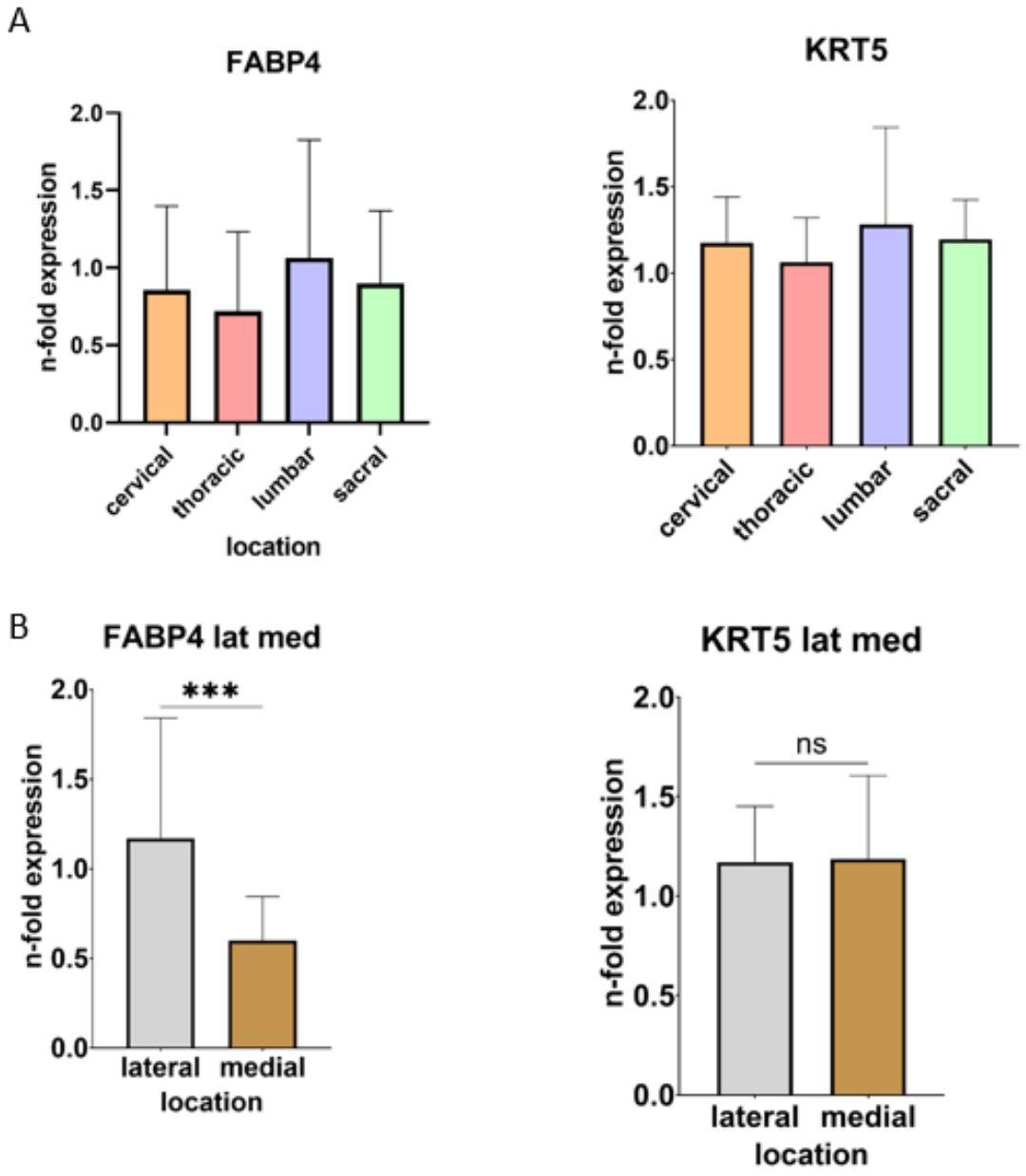

Figure 16: n-fold expression of FABP4 and KRT5 at (A) cervical, thoracic, lumbar and sacral sites, as well as at (B) lateral and medial sites (mean with SD). *Expression of FABP4 was significantly increased at lateral sites (P-value = 0.0002) compared to the expression levels at the respective medial sites. Furthermore, expression of FABP4 was the greatest in the lumbar region, followed by the cervical and sacral area. Similar to the other genes, in the thoracic region the gene expression levels were the lowest. On the other hand, KRT5 did not show alternating expression patterns at lateral and medial sites. Also the comparison of cranial and caudal positions did not show significant differences. The expression maximum was reached in the lumbar region, followed by the sacral one. Once again, the expression minimum was measured in the thoracic area.*

The evaluation of the expression patterns of the inflammatory monocyte-derived cells *CD209* and *CD14* revealed that, while *CD14* was equally expressed at lateral and medial sites, the expression of *CD209* was significantly increased at the medial positions (P-value = 0.0434). Regarding the comparison of the two cranial and two

caudal regions, no significant differences were measureable. However, both genes showed similar trends with their maximum expression in the lumbar **Figure 17**.

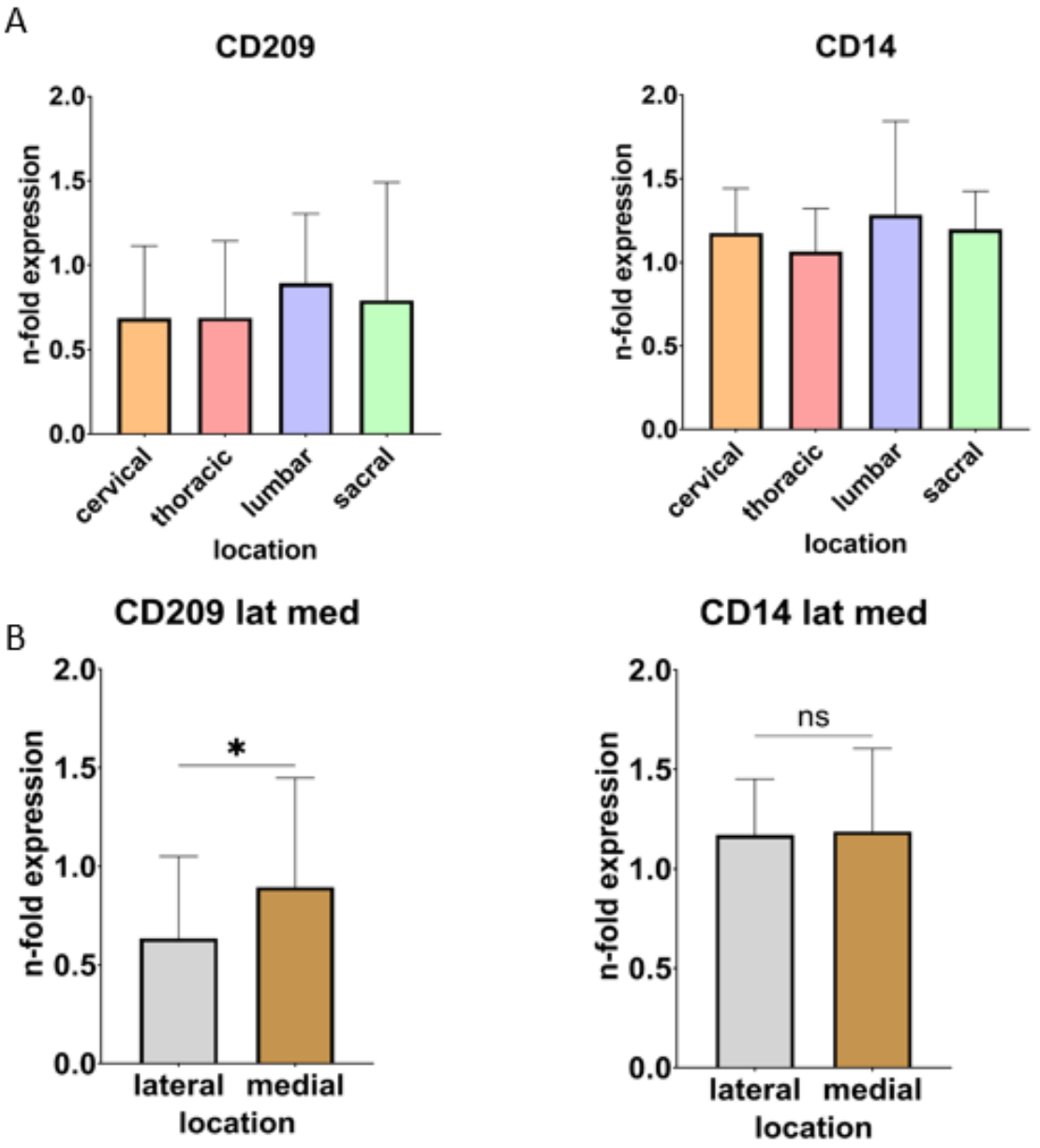

Figure 17: n-fold expression of CD209 and CD14 at (A) cervical, thoracic, lumbar and sacral sites, as well as at (B) lateral and medial sites (mean with SD). *Expression of CD209 was significantly increased at medial sites (P-value=0.0434). CD14 did not show different expression levels in the comparison of lateral and medial positions. Furthermore, expression of both genes was highest in the lumbar area, followed by the sacral area. The minimum expression was measured in the thoracic region (P-values > 0.05).*

Even though *leptin (LEP*) is primarily known as a circulating hormone, which is responsible for energy homeostasis and food intake, it is also an additional factor that

is associated with wound healing and angiogenesis. The expression of *LEP* was enhanced in the lateral area compared to the expression at medial sites; however, the differences were not significant. In addition, also in the comparison of cranial and caudal regions, no significant differences were measureable. Nevertheless, a trend established that indicates that the expression of *LEP* is highest in the sacral area, followed by the lumbar region. The expression minimum was again identified in the thoracic area.

The 130-kDa transmembrane glycoprotein *platelet endothelial cell adhesion molecule-1 (PECAM-1*) was additionally included into the analysis as another marker for endothelial cells. The expression thereof was not significantly different at any of the examined regions. However, expression was higher at the medial sites. In addition, the already observed trend of an expression maximum in the lumbar region as well as an expression minimum in the thoracic area was detected again. The results of the gene expression assays of *LEP* and *PECAM-1* are depicted in **Figure 18**.

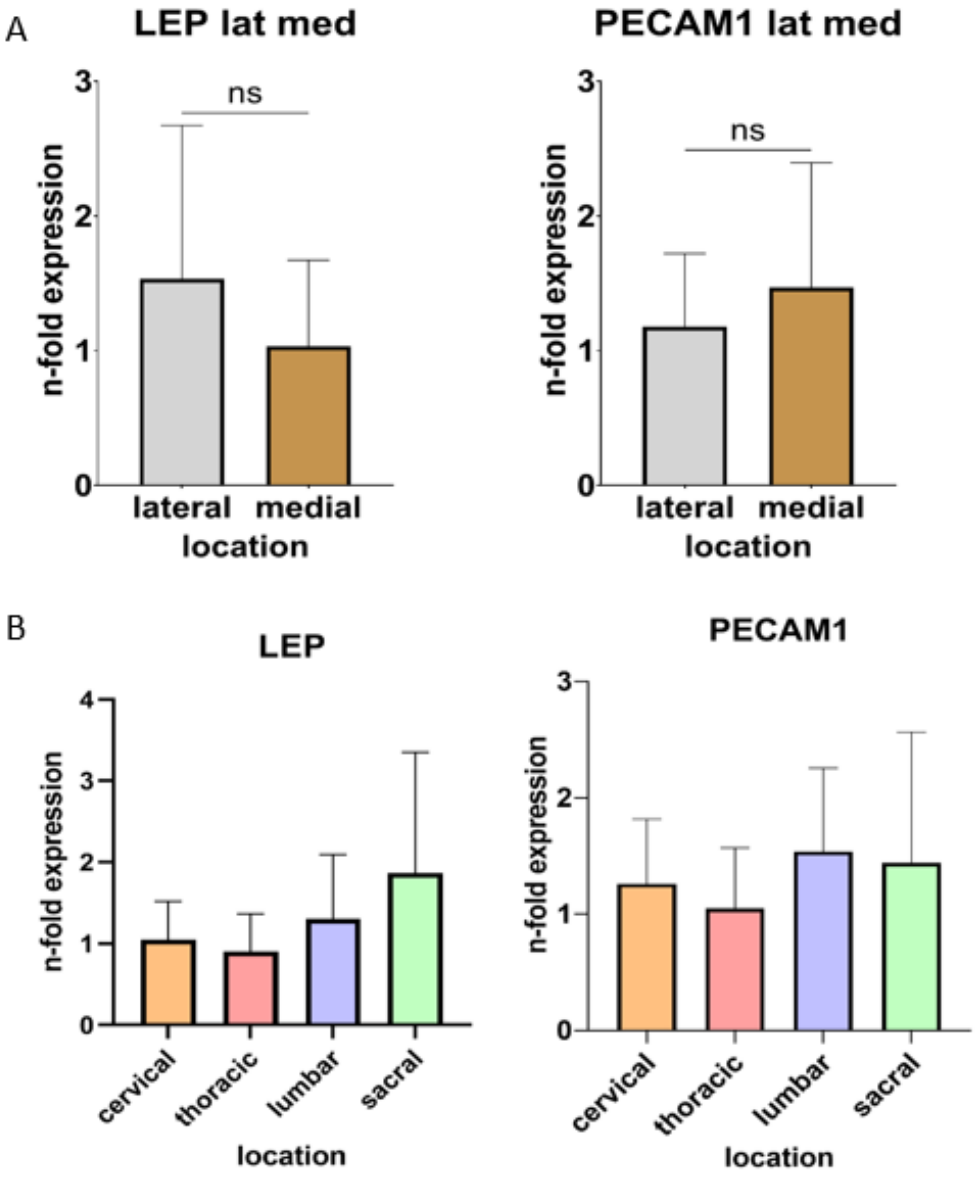

Figure 18: n-fold expression of LEP and PECAM-1 at (B) cervical, thoracic, lumbar and sacral sites, as well as at (A) lateral and medial sites (mean with SD). *Expression of PECAM-1 was increased at lateral sites; however, the differences were not significant (P-value>0.05). LEP did not show different expression levels in the comparison of lateral and medial positions. The expression of LEP was highest in the sacral area, followed by the lumbar and cervical one. The minimum expression of LEP was measured in the thoracic region. PECAM-1 was mostly expressed in the lumbar region, whereas expression was the lowest in the thoracic area.*

The expression of the inflammation markers, *Interleukin-1-Beta* and *C-X-C motif chemokine ligand 8*, in the analyzed biopsies, was too low to reach the needed detection limits. The outcome of the gene expression assays did not reveal meaningful results, since only Cq values higher than 35 were measured.

Discussion

For a long time already, porcine skin has been utilized in numerous studies, especially in those focusing on wound healing, burns and scar tissue formation [24]. The increased utilization of porcine skin as an experimental human analogue is the result of previous investigations that compared and analyzed the properties of skin of different domestic animals [26], [58]. From all the animals studied, the pig has shown to offer the highest amount of essential similarities making it the most appropriate model for human skin. Variations in skin structure and composition that are known to be present in human skin, are also found in porcine skin. While human skin has been extensively studied, there is a paucity in the generation of data on location-related differences in porcine skin [25], [28]. Thus, the first part of this master thesis focusses on the identification and analysis of potentially present location related variations in the composition and structure of porcine skin.

By performing a histological analysis, it was possible to characterize regional variations in porcine skin from 16 different anatomic areas. The greatest skin thickness was measured at the lateral sacral site. The results indicate that the influence of the horizontal location on the cutis thickness is greater than the caudal/cranial positioning. However, the variations present in the two skin layers, epidermis and dermis, occur independently of each other. Whereas the maximum dermis thickness is usually given in lateral areas, the epidermal thickness was found to be greater in the medial regions.

Histological analysis revealed a correlation between the bodyweight/size of the pigs and their skin thickness. However, it appears as if the thicknesses of the epidermis and dermis do not correlate in the same proportion with the body weight of the animals. According to our results, the dermis increases with an increasing body weight, whereas the epidermis shows the opposite trend. However, to propose a significant hypothesis on the correlation of those two parameters, much more animals would have to be included in the analysis. Although previous studies that examined differences in the skin of pigs in relation to the sex of the animals have reported that the dermis indeed correlates with the bodyweight of the animals, the epidermis shows no dependency on the bodyweight [25], [28].

In the categorization into two cranial and two caudal areas, the greatest skin thickness was identified in the sacral region of the pigs' trunk. The determination of the cutis

thickness, as well as the independent dermis and epidermis measurement, led to this outcome. By this, the assumption that porcine skin thickens towards the caudal end could be confirmed. Previous studies have already reported that the highest cutis thickness in a pig's entire body is usually given in the caudal back region [28]. The second greatest distance was measured at the cervical region, which refers to the very cranial area. Also this observation has already been described by Meyer, who refers to that area of the pigs' withers as one of the regions showing the highest skin thickness subsequent to the back [28]. The two inner regions, thoracic and lumbar, exhibited in all three cases very similar values. However, at least regarding the dermis, the thoracic region exceeded the lumbar positions. The measurement of the epidermis revealed almost identical values, indicating that there is no location-related difference in the epidermis regarding those two areas.

Since the results of the comparison of those four regions are consistent, they clearly indicate the presence of regional anatomic variations in the porcine skin. However, the results suggest that the decisive point is not only whether the position is cranial or caudal, but also the proximity to the middle part (loin), regardless of whether head or pelvic region, seems to be important. Since dermis and epidermis revealed to be the thinnest at the two inner regions, thoracic and lumbar, it can be assumed that porcine skin decreases in depths towards the loin, whereas it increases towards the cranial and caudal end. Even though the increase is the greatest in the sacral area, a significant gain in the thickness was also measured in the cervical region compared to the thoracic and lumbar positions. That outcome is confirmed by some publications that observed the same trend [24], [28].

In the course of data analysis, it became apparent that not only a dependency of the skin`s thickness on the cranial or caudal location, but also on the horizontal location (proximity to the spine) is present. Our results suggest that the lateral/medial positioning is even more influential on the cutis thickness than the caudal/cranial location. Especially regarding the dermis, the lateral sites show a far greater thickness than the medial sites. Since the dermis is in general to some extent thicker than the epidermis, the influence of the dermis on the cutis thickness is greater than that of the epidermis [28]. Consequently, also the cutis thickness showed higher values in the lateral area than in the medial area. In contrast to that, our results do not suggest a dependency of the epidermis on the horizontal location. A higher epidermis thickness

was not identified at the lateral, but at the medial site. Furthermore, the difference between the two average values was less significant.

According to the results, the dermis increases in depth towards the dorsal area, whereas the epidermis even decreases a little in depth. Accordingly, Meyer et al. reported that in contrast to the dermis, there is no tendency for the epidermis to increase or decrease in thickness from the back to the abdomen [28]. This confirms the assumption that the epidermis' thickness is less dependent on the horizontal location. However, concerning the dermis, the data found in literature is inconsistent. Whereas certain regions along the pigs' trunk are found to be thicker in the lateral area, others increase in depth towards the median [26], [28]. Consequently, a more detailed separation including a simultaneous classification into caudal and cranial, as well as lateral and medial positions was needed.

Accordingly, if both parameters, the cranial and caudal as well as the lateral and medial location, were considered in the evaluation, the maximum distance of the dermis was measured at the lateral sacral site. However, this time, the second greatest distance was evaluated in the thoracic lateral region, followed by the cervical one. The minimum distance was measured in the lumbar medial region. As already mentioned before, it is known that the greatest skin thickness of pigs is usually given in the sacral area [28]. However, also the fact that the thoracic lateral site overtook the respective cervical one regarding the dermis thickness can be explained. This displays an already observed formation, which is specific to the dermis. Previous studies refer to it as the "shield formation" in the shoulder area of pigs. It is especially distinct in wild boars but also in domestic pigs. This formation shapes along the body of the animals and has the form of a lying, elongated-oval knight's shield with a straight frontal end. It decreases towards the caudal region and closes at the level of the rib. That means it is not reaching into the lumbar area. The shields end cranially with the front edge of the shoulder blade and dorsally below the medians of the body [28]. This explains why the same trend was not observed at the medial positions. The cervical regions may be still part of the shield, however only at the edges, which is why the cervical regions are not as influenced by this formation as the thoracic regions are, which are located in the middle of the shields. The formation of this skin structure is related to a strong thickening of the dermis in the corresponding area. However, this only holds true for the dermal part of the skin and not for the epidermal one, which exhibits the greatest

thickness in the sacral back region, followed by the cervical medial one [24], [28]. Of the four positions examined, the mid medial regions (thoracic and lumbar) show similar values and refer to the areas with thinnest epidermis thickness.

Besides those results from our study, other experiments on porcine skin have shown that the dermis of male pigs is usually thicker compared to the dermis of female animals [25], [26]. Since only female pigs were included in our study, this observation could not be verified by us. However, literature reports of average porcine dermis thicknesses of around 1800 -2100 µm in females and 3800-4100 µm in males [26], [28]. This applies to our results since the measured dermis thicknesses lay between 1833- 2082 µm. Regarding the epidermis, the opposite trend has been reported. In this case, the epidermal skin layer is approximately 20-40 % thicker in females than in males and mostly measuring distances between 100- 120 µm [25], [28].

In addition to the histological analysis, an ultrasonic evaluation was performed. Even though ultrasound is recognized as a valuable tool in clinical skin assessment and is considered useful in the evaluation and quantification of skin lesions, only few studies have assessed the validity of ultrasound in the measurement of skin thickness. Especially in non-human skin samples, the application of ultrasound for this purpose has not been investigated yet. In this study, ultrasound was applied in the measurement of the thickness of the porcine dermis. The aim thereof was to validate skin ultrasound measurements against histological skin analysis [58].

Since this technique is less labor-intensive compared to the histological evaluation, it would be desirable to achieve similar and meaningful results. However, the separation of the dermis and the hypodermis during the evaluation was found to be very challenging. A determination of a clear border between the two layers was not possible and consequently, the obtained results cannot be considered robust and reproductive. Accordingly, the employment of ultrasound in the measurement of the porcine dermis is not the method of choice. It can be applied if a rough estimation is needed, however, in the case of the present experiment, not even a reliable trend was detectable. The results mostly contradicted the outcome of the histological evaluation. However, using histology a clear and precise separation of the different layers was possible. Consequently, the data of the histological evaluation are of major importance. Additionally, the outcome thereof matches with the identified trends of previously conducted studies examining the structure of porcine skin. Even though, ultrasound is

highly important in many medical fields and is also successfully applied in the detection of objects and measurement of distances, my data suggests that it is not suitable for the measurement of the porcine dermis thickness. In **Figure 19,** a direct comparison of the results of the histological and ultrasonic evaluation is depicted. The values obtained in the US measurement are not only lower, but are also displaying a different outcome regarding location-related differences in the porcine dermis thickness.

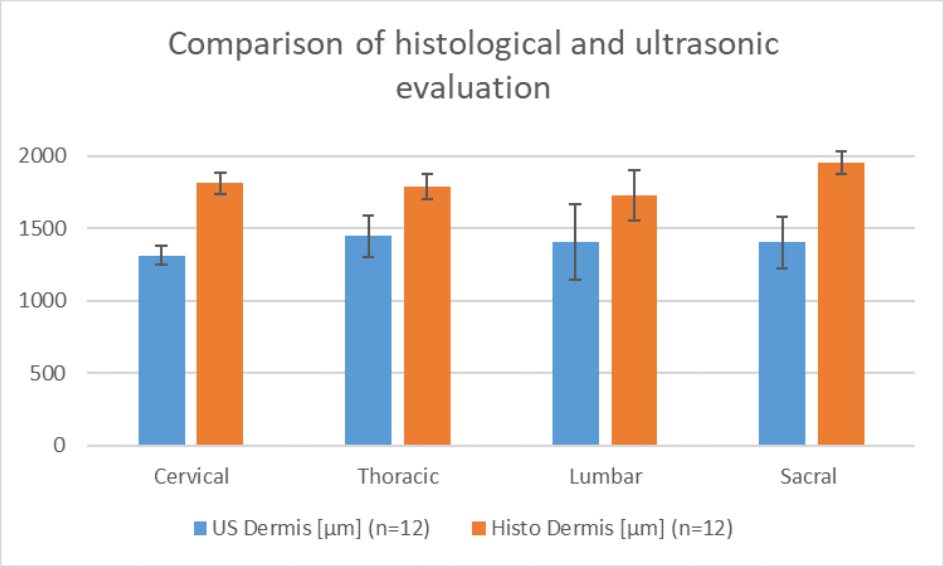

Figure 19: Direct comparison of the results of the histological and ultrasonic evaluation. *The values obtained in the US measurement are lower than those obtained in the histological analysis. Furthermore, the revealed trends are not coherent.*

In addition to the measurement of the skin thickness, an analysis of the composition of the skin, and potentially present location-related variations in the composition, was conducted. The aim was to evaluate the structure of porcine skin via analysis of the density and the distribution of blood vessels, immune cells and other structurally relevant factors.

This was achieved by performing gene expression analysis of certain genes that are crucial in the development of those structures as well as in wound healing processes. By measuring and comparing the expression levels of the respective genes at the examined sites, variations could be detected and quantified. Accordingly, the expression levels of pro- and anti-inflammatory mediators, factors involved in angiogenesis, transcription and growth factors as well as of adipocyte and endothelial markers were evaluated. To be more precise, the factors analyzed included: the inflammation markers *IL1B* and *CXCL8*, the angiogenesis markers *VEGFA* and *FGF2*, as well as the growth factor *ACTA2* and the wound healing associated transcription

factor *HIF1A.* The *fatty acid-binding protein 4 (FABP4),* the keratinocyte marker *KRT5* and the markers of inflammatory monocyte-derived cells, *CD209 and CD14*, were additionally considered in the evaluation. Moreover, as an additional factor that is associated with wound healing and angiogenesis, *LEP* was analyzed and to include another endothelial marker, *PECAM-1* was added.

Housekeeping genes are expressed in all cells of an organism under normal and patho-physiological conditions, regardless of the tissue type, developmental stage and external signal. Thus, they are widely used as an internal control in experimental research [59]. In this study, the housekeeping gene *ß-actin (ACTAB)* was used.

One of the most potent pro-angiogenic factors in wound healing is *VEGFA.* It is mostly found in connective tissue cells like fibroblasts, macrophages and mast cells [60]. The expression of *VEGFA* is induced by some transcription factors. One of those is the hypoxia-inducible factor *HIF1A*. Since also some pro-inflammatory cytokines were found to be able to activate HIF1 in certain cell types, a role of *HIF1* in the regulation of gene expression during inflammation was proposed [61].

According to our results, the expression of the vascularization factor *VEGFA* is significantly higher at lateral than at medial porcine body sites. Consequently, it can be assumed that in the lateral region a more pronounced vascularization is given. Since none of the biopsies included in the analysis were in close proximity to an ongoing inflammation process, the expression of inflammation-induced genes was not favoured in this experimental setup. *HIF1A*, which plays a role in the regulation of gene expression during inflammation, did not show significant alterations in the gene expression patterns in relation to the body site. The comparison of the expression levels of the two genes in the caudal and cranial area of the pig`s trunks did not reveal significant differences. However, out of the four examined regions, the expression was in both cases the lowest in the thoracic region.

Also the level of *Fibroblast growth factors* (*FGF*) expression is an important factor during wound healing, as it has a great influence on many processes that are crucial for proper wound closure and tissue regeneration. The local dependent gene expression thereof is important to be known before choosing a suitable site for wound healing studies [62]. The gene expression analysis has shown significant increases in the expression levels of *FGF2* in the lateral area. In contrast to that, the data suggests that *ACTA2*, which functions as a marker of myofibroblast formation, is expressed

equally in both regions- lateral and medial [63]. Regarding the separation into cranial and caudal regions, the expression levels of the two genes were again the lowest in the thoracic area. However, one cannot see any highly significant alteration in the gene expression pattern of *ACTA2* or *FGF2* in relation to the cranial/caudal position.

Furthermore, the expression patterns of *FABP4* were additionally included in the molecular evaluation. Again, the generated data shows a significantly higher expression of *FABP4* at lateral sites compared to the expression at the respective medial sites. In this case, the outcome can be explained considering the natural fat distribution in the body of pigs. Usually the amount of adipose tissue increases towards the abdomen and is relatively small in the medial region, which is in close proximity to the animal`s spine. The adipocyte *fatty acid-binding protein (FABP4)* belongs to the FABP superfamily and is highly expressed in adipose tissue by means of adipocytes and macrophages [64]. Accordingly, the levels of *FABP4* are higher in the lateral regions than in the medial ones. Referring to the separation into a cervical, thoracic, lumbar and sacral region, the difference in the expression level is less significant. However, as it was also the case for most of the other genes, the expression was again the lowest in the thoracic region, whereas the expression maximum of *FABP4* was identified in the lumbar area.

As already described before, the epidermis represents the avascular superficial layer of the skin and consists to up to 95% of several layers of cornifying squamous keratinocytes. Those keratinocytes (KC) are the first cellular defence line in the skin and they are capable of secreting a wide range of pro-inflammatory cytokines, such as cationic antimicrobial peptides (AMPs, e.g. cathelicidins) [1]. In this study, *Keratin 5 (KRT5*) was analyzed as a marker of keratinocyte expression. However, no location-related differences in the expression pattern thereof at any of the analyzed positions were detectable. Even though the expression minimum was again identified in the thoracic region, the values mostly resembled indicating no great variations in the gene expression levels due to the location. The outcome thereof also pairs up with the results of the histological measurement of the epidermis thickness, which also revealed that no significant differences are given at any of the examined positions.

In the dermis, the most important and dominating immune cell type is represented by dendritic cells (DC). Many different subsets of DC have been described already, which possess important functional specializations. In this study, the expression patterns of

two DC with monocytic origin (monocyte-derived DC) were analyzed. *CD209* and *CD14* represent markers of dendritic cells and macrophages. The evaluation of their expression patterns at the different body sites revealed that the expression of *CD209* was significantly increased at medial sites compared to the respective lateral sites. In contrast to that, *CD14* was equally expressed in both areas. In addition, the comparison of the two cranial and two caudal regions showed the already observed trend with the minimum expression in the thoracic region and the highest expression on the lumbar area. Besides, Summerfield et.al. have already reported that *CD209* as well as *CD14* are generally rather rare in the dermis under steady state conditions [1]. However, their amount increases under inflammatory conditions. This observation cannot be verified, since no inflammatory conditions were given in our samples.

The *platelet endothelial cell adhesion molecule*-1 (*PECAM-1*) is a 130-kDa transmembrane glycoprotein of the immunoglobulin (Ig) superfamily that is expressed on the surface of monocytes, neutrophils, platelets and on some selected T-cell subsets. It is part of the endothelial intercellular junction and plays an important role in many cellular interactions, such as in inflammatory processes or between adjacent endothelial cells during angiogenesis [65]. The analysis of the expression patterns of *PECAM-1* at different sites revealed that no significant alterations in the expression levels are present at any of the examined positions. The observed trend indicates a higher expression at medial than at lateral sites, as well as a higher expression in the lumbar and sacral area. However, the differences were not found to be significant. Consequently, no conclusion on anatomical site-related variations can be made.

The product of the *Leptin* gene is a 16kDa polypeptide anti-obesity hormone that is usually produced by adipose tissues. It is known for its influence on body weight homeostasis via affecting food intake by giving negative feedback to the hypothalamic nuclei. However, some past studies revealed an effect of *Leptin* on would healing processes. Tadokoro et.al have proven that *LEP* is able to promote wound healing in the skin by enhancing proliferation as well as differentiation and migration of epidermal keratinocytes and thereby enhancing angiogenesis in the wounded area [66]. In this study, no significant differences in the expression levels of this gene were detectable. However, some trends established that indicated an enhanced expression at lateral and sacral sites. Since *LEP* is mainly expressed by adipose tissue, those results appear logical [63]. The fat content is usually higher in the lateral area than in the

medial, and also an increase towards the caudal end of the porcine back matches the expected trend. Nevertheless, the differences were not significant.

The fact that healthy tissue was utilized in the experiments is also the reason why the molecular evaluation of the gene expression patterns of *CXCL8* and *IL1B* could not be included in the evaluation. The expression levels of these two inflammation markers were too low to obtain meaningful values. Since the biopsies were derived from healthy skin tissue, no inflammation processes that could have increased the expression levels of these genes were present. Nevertheless, they were still included in the experimental setup with the aim of investigating whether there is a basal expression and, if so, whether this basal expression differs from region to region. This question could not be answered because the basal expression was too low.

Conclusion

In conclusion, it can be said that the expression patterns do not show great variations between the different anatomical regions. The expression of the genes *VEGFA*, *FGF2* and *FABP4* was significantly higher at the lateral sites than at the respective medial ones. In contrast, *CD209* was expressed significantly higher at medial positions. In the separation into the cranial and caudal areas, none of the genes analysed showed significantly different expression patterns. However, a noticeable trend established, which indicates a generally higher expression in the lumbar and cervical region, closely followed by the sacral one. The expression in the thoracic area was in almost every case the lowest. However, the differences were still rather minor and do probably not affect the healing and inflammation processes in the skin. While it would be advantageous to consider the identified differences regarding the skin thickness at the examined positions in designing an experimental setup, the variations regarding gene expression seem to be less important. Nevertheless, in the course of this project, a more detailed picture of the structure and composition of the skin along the entire pigs‘ back could be created, which will be needed and used in the design of preclinical studies involving wound induction and wound healing.

Proof-of-principle experiments using magnetic nanoparticles (MNPs)

Material and Methods

Magnetic nanoparticles

The magnetic nanoparticles consisted of magnetite (Fe_3O_4; ferrite oxide) and had a polyethylene (PEG-2000) coating. They were directly ordered from the German company *MicroMod* (Rostock, Germany*)*. The particle`s diameter was 180 nm and the stock had a concentration of 10 mg/ml (nanomag®-D, PEG-2000, 180 nm, 10 mg/ml, prod. Code: 09-82-182; MicroMod, Germany). Jia et al. used the same particle type in their experiments and estimated the magnetic moment per particle as follows: 305 emu/nmol for D=180 nm particles [55].

For the experiment, a 10 mg/ml solution was further diluted to a concentration of 0.5 mg/ml (d= 1:20). The inflow bag was loaded with 1-2 ml of the dilution and eventually had to be refilled during the experiments.

Magnets

The magnets used in the experiments were ordered at the German company *Supermagnete*® (Gottmadingen, Germany) in three different sizes. The magnets were disc-shaped and consisted of neodymium, iron and boron. The magnet that had the best dimension in relation to our experimental setup, and was therefore mainly used, was the medium-sized magnet (magnet type 1), which had a diameter of 2 cm and a height of 1.2 cm (NdFeB magnet Ø 20 mm,12 mm, neodymium N42; Article-ID: S-20-12-N). The second, smaller sized magnet (magnet type 2) had a diameter of 5 mm and a height of 3 mm (NdFeB magnet Ø 5 mm, 3 mm, neodymium N42; Article-ID: S-05-03-N). Since these magnets were to some extent smaller, they were used in clusters (two magnets attached to each other). The biggest magnet used in our experiments (magnet type 3) had a diameter of 4.5 cm and a height of 3 cm (NdFeB magnet Ø 45 mm, 30 mm, neodymium N42; Article-ID: S-45-30-N). An NdFeB-magnet of this dimension has already an adhesive force of around 70 kg. While designing the experimental setup, it turned out that this magnet size is too big for our application,

which is why it was used just once. Further information on the magnets can be taken from the manufacturer data sheet that can be found on their website.

Agarose gels

Agarose gels were used as a dummy for skin to estimate the strength of the magnets and to evaluate the magnet's ability to reach into certain depths. Therefore, five different depths (2 mm, 4 mm, 5 mm, 7 mm and 12 mm) were examined in the trials. The agarose was ordered at the company *Bartelt* (multi-purpose agarose; Art.Nr.:9584695; Graz, Austria). The gels had a concentration of 2 % (w/v) and were poured in weighing dishes (ROTILABO® 14x14 cm, 2 cm height) in layers to obtain different heights (12 mm= 200 ml; 7 mm= 100 ml; 5 mm= ~90 ml; 4 mm= ~80 ml; 2mm= ~30 ml).

Pump and tubes

The pump, which created the flow in the tubes, as well as the tubes themselves, were provided from the institute *JOANNEUM RESEARCH HEALTH*. The peristaltic pumping system is part of the open-flow-microperfusion device that was developed by *JOANNEUM RESEARCH HEALTH*.

Since the blood flow velocity in microcapillaries in the skin is about 0.5 mm/sec, a flow rate of 1.475 µl/min was needed. Therefore, the pump rate of our peristaltic pumping system was set to 1.5 µl/min. However, to counteract the rising pressure that may form inside the tubes due to a possible constipation generated by a magnet-induced aggregation of the magnetic nanoparticles, the tubes in the experimental setup of the first test run had a branching point before reaching the gels. The idea was to provide pressure relief, if necessary. Additionally, by this, the possibility of direct comparison between two positions with identical test conditions and the only differing parameter of the applied or missing magnet was provided. The branching point was introduced using a Y-connector that was not entirely compatible with the tubes and had to be glued together using a UV-light based glue. The pump rate was set to the approximately doubled flow rate (3 µl/min) in the first test run. Due to the branching point, this resulted again in a flow rate of ~1.5 µl/min in the region of interest. The tubes had an inner diameter of 0.25 mm and consisted of perfluoroalkoxy polymer (PFA).

Determination of the MNP concentration

To include quantitative analysis, the amounts of iron, and thus the amounts of magnetic nanoparticles in the outflow solution were determined photometrically using a potassium thiocyanate (KSCN) based assay. Therefore, aliquots of 20 µl of the obtained MNP outflow solutions were mixed with 200 µl concentrated HCl (hydrochloric acid, 37%, a.c.s. reagent; 258148-25ML; Sigma-Aldrich®) to ionize the iron oxide crystal core and liberate the iron in its ferric state. Then the samples were incubated for five minutes at room temperature with 250 µl of a 40 mM Potassium thiocyanate aqueous solution (volumetric, 8M KSCN; BCCB9798; Sigma-Aldrich®). The product of the reaction between the anion $[SCN]^-$ and the $Fe3^+$ is a red coloured complex, pentaaqua(thiocyanate-N)Fe(III), $[Fe(NCS)(H_2O)_5]^{2+}$, whose absorbance (ABS) at 480 nm was read in a nanodrop spectrophotometer (NanoDrop™ One/OneC Microvolume UV-Vis Spectrophotometer; Thermo Scientific™).

To evaluate the concentration of magnetite in the outflow tubes, a calibration curve was generated (**Figure 20**). Therefore, the magnetite stock solution (10 mg/ml (nanomag®-D, PEG-2000, 180 nm, 10 mg/ml, prod. Code: 09-82-182; MicroMod, Germany) was diluted in PBS (PBS pH 7,2; SLBX1593; Sigma-Aldrich®) to a stock concentration of 2 mg/ml. Since the inflow had a concentration of 0.50 mg/ml, concentrations close to this value were desired for the establishment of the calibration curve. The following concentrations in mg/ml were recorded: 1.0 mg/ml; 0.8 mg/ml; 0.6 mg/ml; 0.5 mg/ml; 0.4 mg/ml; 0.2 mg/ml; 0.1 mg/ml (diluted with PBS).

The standards and the fractions of the samples were measured using a Spectrophotometer with an absorbance maximum at 480 nm, as described:

20 µl sample/stand + 200 µl HCl + 250 µl KSCN

Reaction: $Fe^{3+} + SCN^- \leftrightarrow FeSCN^{2+}$

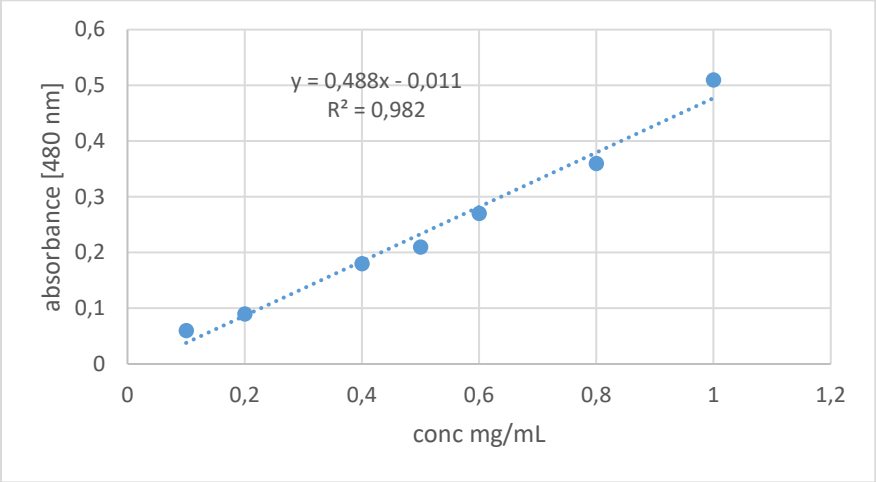

Figure 20: Calibration curve: MNP concentration in [mg/ml] vs. absorbance at 480 nm. *Seven different concentrations were analysed (1.0 mg/ml; 0.8 mg/ml; 0.6 mg/ml; 0.5 mg/ml; 0.4 mg/ml; 0.2 mg/ml; 0.1 mg/ml (diluted with PBS)).*

Experimental setup and Procedure

In the following *in vitro* proof-of-principle experiments using magnetic nanoparticles, agarose gels were used as a representative material ("dummy") for skin to estimate the strength and influence of the applied magnet on the magnetic nanoparticles in solution through a barrier of a certain thickness. These first experiments aimed at guaranteeing the principle feasibility of the method and to observe the magnetic capture of MNPs in a flow system via magnet-induced MNP retention.

Figure 21 shows a simple self-drawn sketch of the experimental setup. The inflow bag is filled with magnetic nanoparticle (MNP) solution (c= 0.5 mg/ml) and is attached to the peristaltic pumping system (not depicted here). The pump generates the flow of the MNP solution in the tubing system towards the outflow tube. In the middle part, the tube is implanted into a gel of a certain thickness, which has the magnet applied on top of it. The magnet should be strong enough to reach the magnetic nanoparticles flowing through the tube and retain them in place. That should result in a lower concentration of magnetic nanoparticles in the outflow compared to the concentration of MNPs in the inflow.

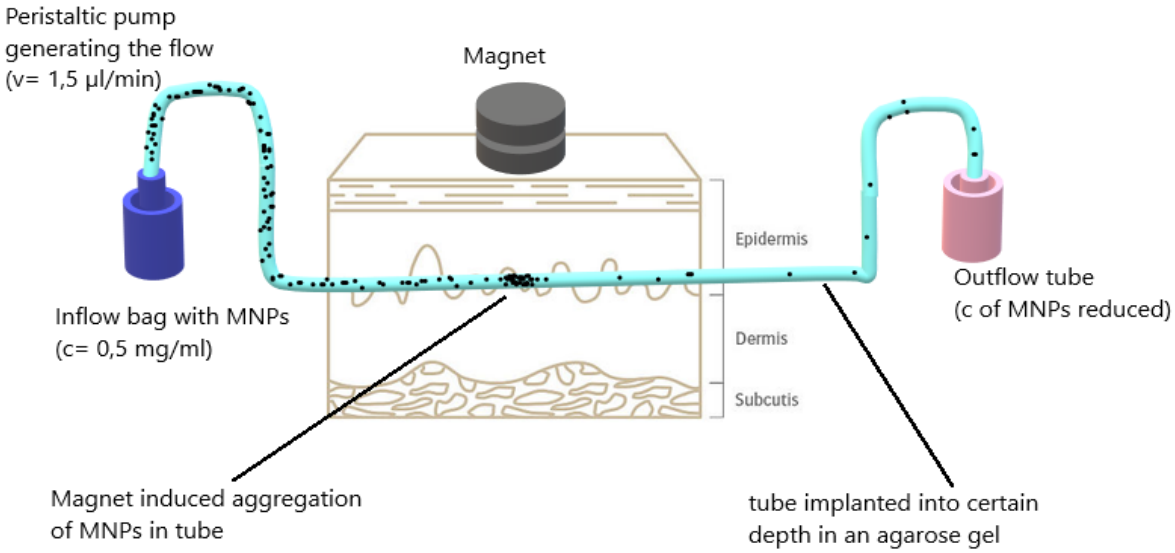

Figure 21: Simple sketch of the experimental setup: *Inflow bag with magnetic nanoparticle (MNP) solution (c= 0.5 mg/ml) attached to a pumping system (not depicted here). The pump generates the flow of the solution in the tubing system in the direction towards the outflow tube. In the middle part, the tube is implanted into a gel of a certain thickness, which has the magnet applied on top of it. The magnet should be strong enough to reach the magnetic nanoparticles flowing through the tube and retain them in place. That should result in a lower concentration of MNPs in the outflow compared to the concentration in the inflow.*

To evaluate and compare different parameters and conditions, six different *in vitro* test runs were conducted. The differing parameters included the magnet size, the thickness of the gels and therefore of the barrier, the amount and setup of the tubes, the time, and the number of total responses (n) of each test run. The six test runs were further organized in the following manner: the first trial, which comprises the test runs 1 and 2; the second trial, including test runs 3, 4 and 5; and the third trial, which corresponds to the sixth and last test run. Each trial has some similarities in the experimental setup, which is why they are categorized into those sub-groups. **Table 7** gives an overview of the different parameters in the three trials' experimental setup.

Table 7: Overview of the different parameters in the experimental setup of the three trials. *Following conditions differed in the individual test runs: magnet type, thickness of the gel, number of the tubes, timestep of interest, number of total responses (n)*

Magnet types	Gel thicknesses [mm]	number of tubes	timestep [min]	[n] of each test
1 and 2	4, 5 and 7	6	40 and 15	1
1, 2 and 3	2, 7 and 12	6	20	1
2	1, 5 and 12	3	20	3

Initial experiment setup

This trial refers to the first proof-of-principle experiments of this kind and included two different test runs, which differed in three main points. Firstly, the time step after which the magnets were applied/removed was set to 40 minutes during the first test run and to 15 minutes during the second one. Secondly, two different conditions (prior magnet and magnet applied) were studied in the first test run. In contrast, in the second test run, three different conditions were investigated (prior magnet, magnet applied and post magnet). Lastly, during the first test run, only magnet type 1 was used, and the six gels with three different depths were divided into three positive controls (1M-3M; magnets applied) and three negative controls (1B-3B; no magnets applied). In the second test run, the three positive controls (1M-3M) remained the same, while only one of the three negative controls was kept as a negative control (1B). The other two (2B and 3B) were used for the application of the smaller magnets (magnet type 2). In **Table 8,** the different conditions at each position in the two test runs are depicted.

To counteract the rising pressure that may form in the tubes, secondary to a possible constipation generated by a magnet-induced aggregation of the magnetic nanoparticles, a branching point was introduced in the first trial. The idea was to provide pressure relief, if necessary. Additionally, by this, the possibility of direct comparison between two positions with identical test conditions and the only differing parameter of the applied or missing magnet was provided. However, the Y-connector was not entirely compatible with the tubes and had to be glued together using a UV-light based glue. Since it became apparent that the branching point could act as a possible source of error, it was excluded in the two subsequent trials.

Table 8: Experimental setup of the first trial. *Magnet types used were magnet type 1 and magnet type 2. The gels had a height of 7 mm, 4 mm and 5 mm. The time step was set to 40 minutes in the first test run and to 15 minutes in the second run. Positions 1M-3M were treated in the same way in both test runs, whereas positions 1B-3B were altered.*

[^{x} = 2 conditions investigated (prior magnet & magnet applied); ^{Y} = 3 conditions investigated (prior magnet, magnet applied & post magnet)]

Experimental setup of the first trial		
Position	**Test run 1^{x} with t= 40 min**	**Test run 2^{Y} with t= 15 min**
1M	Magnet type 1; Gel= 7 mm	Magnet type 1; Gel= 7 mm
2M	Magnet type 1; Gel= 4 mm	Magnet type 1; Gel= 4 mm
3M	Magnet type 1; Ge = 5 mm	Magnet type 1; Gel= 5 mm
1B	No magnet; Gel= 7 mm	No magnet; Gel= 7 mm
2B	No magnet; Gel= 4 mm	Magnet type 2; Gel= 4 mm
3B	No magnet; Gel= 5 mm	Magnet type 2; Gel= 5 mm

Figures 22-25 show the experimental setup in pictures. The three right sided gels in **Figure 22** display the positive controls on which the magnets were applied in both test runs. The left sided gels were used as negative controls or respectively at position 2B (middle gel) and 3B (upper gel) for the application of magnet type 2 in the second test run.

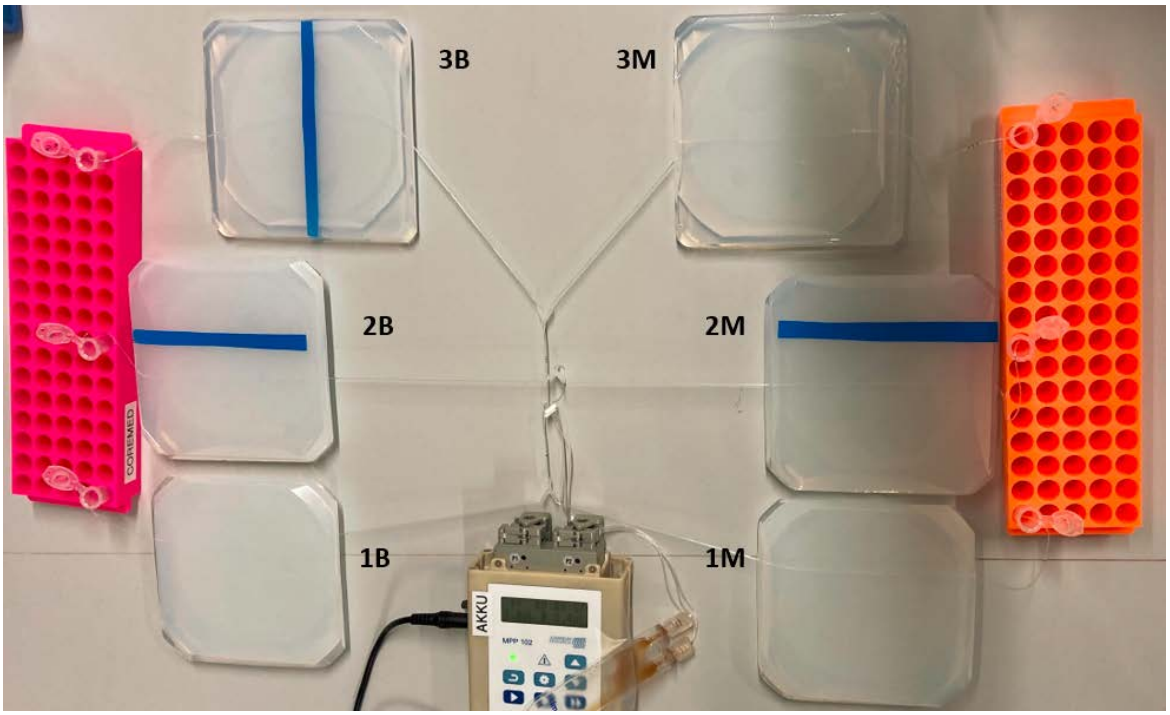

Figure 22: Experimental setup of the in vitro experiments in the first trial*. The right sided gels refer to the positions 1M-3M; the left sided gels to the positions 1B-3B. In the middle of the image, the peristaltic pump is depicted.*

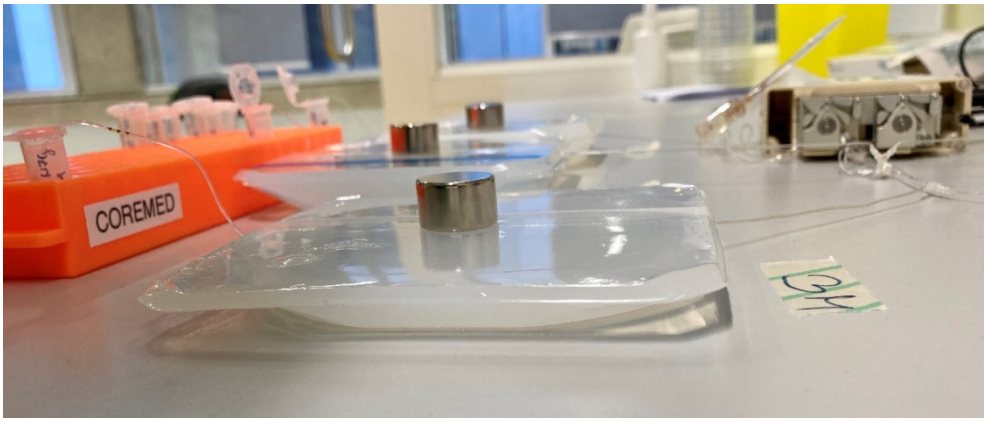

***Figure 23: Experimental setup of the in vitro experiment**. Magnet type 1 is placed on a gel in which a tube is implanted.*

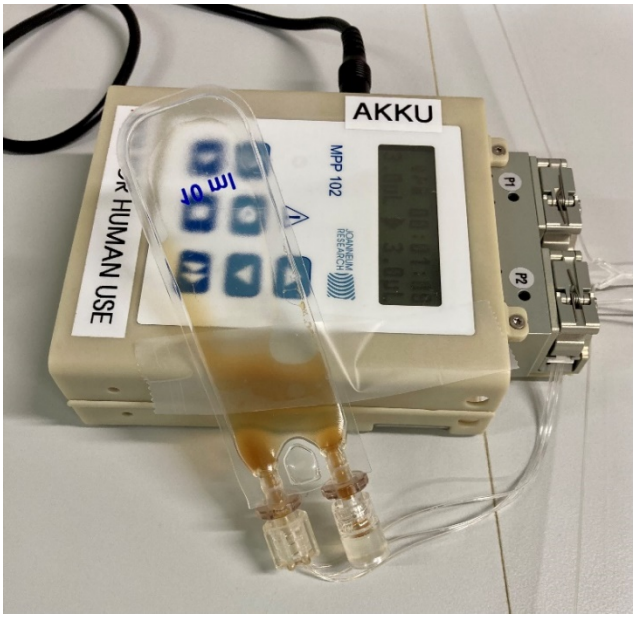

***Figure 24: Experimental setup of the in vitro experiment**. The peristaltic pumping system with the respective inflow bag is shown. The pump generates a flow of 3 µl/min in the first trial or 1,5 µl/min in the second and third trial. The inflow bag is filled with a 0,5 mg/ml MNP solution.*

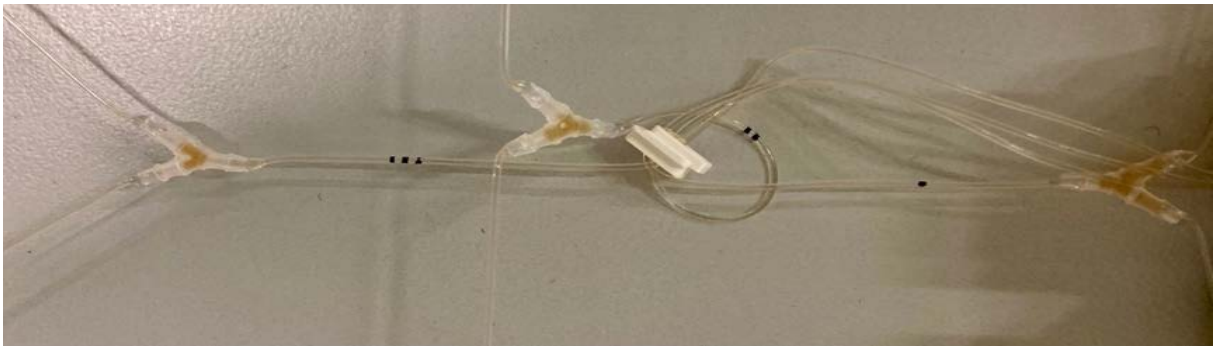

***Figure 25: Experimental setup of the in vitro experiments**. In the first trial, a branching point was introduced to provide the possibility of pressure relief if needed. However, it became apparent that this might act as a source of error and was therefore excluded from the setup of the second and third trial.*

Refine tubing

In the second trial, some alterations and optimizations in the experimental setup were employed. This trial consisted of the different test runs 3, 4 and 5. In the third test run, three different conditions were investigated (prior magnet, magnet applied and post magnet). In contrast to that, in test run 4 and 5 only one condition (magnet applied) was analyzed. The time was set to 20 minutes to achieve a timestep, which is short enough to represent the retention of the magnetic nanoparticles via the concentration differences in the in- and outflow and long enough to eventually also observe an impact on the outflow volume.

Additionally, each position was investigated in duplicates, which means that positions, e.g. 1A and 1B, were exposed to identical conditions. Therefore, the setup comprised six gels and tubes but no negative controls. Test runs 4 and 5 refer to some experimental setups that were mainly conducted to observe possible differences in the impact of the three different magnet types. Position 1 was exposed to magnet type 1 (medium-sized magnet) in the fourth test run and to magnet type 3 (big-sized magnet) in the fifth test run. Since magnet type 2 (small-sized magnet) was applied in the third test run, all three magnets' impacts could be compared. Additionally, position 3 was exposed to the two magnet types 1 and 3, which also allowed a comparison at this position. To investigate the impact of a double-sided exposure to magnetic capture, the tube at position 2 was squeezed in between two gels that both had magnet type 1 applied on either of the sides.

In **Table 9**, the different conditions at each position in the second trial's test runs are depicted.

Table 9: Experimental setup of the second trial. *Magnet types used were magnet type 1, magnet type 2 and magnet type 3. The gels had a diameter of 2 mm, 7 mm and 12 mm. The timestep was set to 20 minutes in all test runs. Positions were measured in duplicates with identical conditions (A and B).*

[X→ three conditions investigated (prior magnet, magnet applied & post magnet); Y→ only one conditions investigated (magnet applied)

Experimental setup			
Position:	***Test run 3X***	***Test run 4Y***	***Test run 5Y***
1M	Magnet type 2	Magnet type 1	Magnet type 3
	Gel = 2 mm	Gel = 2 mm	Gel = 2 mm
1B	Magnet type 2	Magnet type 1	Magnet type 3
	Gel = 2 mm	Gel = 2 mm	Gel = 2 mm
2M	Magnet type 1	No magnet	2x type 2
	Gel = 7 mm	Gel = 7 mm	Gel = 7 mm
2B	Magnet type 1	No magnet	2x type 2
	Gel = 7 mm	Gel = 7 mm	Gel = 7 mm
3M	Magnet type 1	Magnet type	No magnet
	Gel = 12 mm	Gel = 12 mm	Gel = 12 mm
3B	Magnet type 1	Magnet type 3	No magnet
	Gel = 12 mm	Gel = 12 mm	Gel = 12 mm

As already mentioned above, the branching point was precluded from this trial. However, to still provide a possibility to detect and quantify a rising pressure inside the tubes that may build up due to the magnet-induced aggregation of the MNPs, the tubes were equipped with pressure sensors, which the institute JOANNEUM RESEARCH HEALTH provided. The second trial's experimental setup (test run 3) is depicted in **Figure 26**. The design resembles the first trial since also this time, six gels and tubes were used. The magnets applied were magnet type 1 and type 2. The device on the left side of the picture shows the pressure sensor apparatus. The peristaltic pump with the inflow bag was placed in the middle and the two duplicates were arranged on opposite sides.

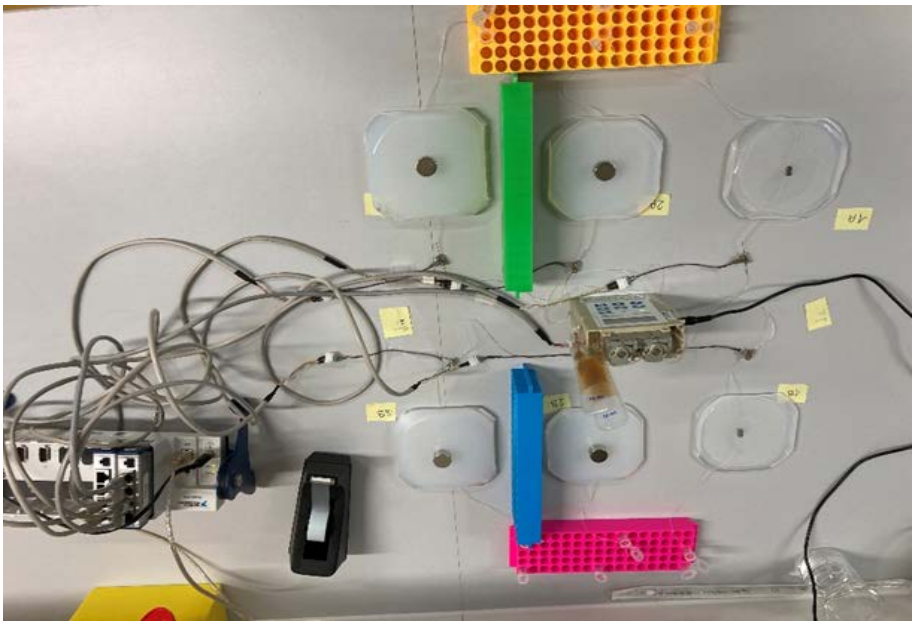

Figure 26: Experimental setup oft the second trial (test run 3). *The arrangement comprises six gels and tubes. The left side of the picture shows the pressure sensor apparatus. The peristaltic pump is located in the middle.*

Repeat experiment

In the third trial, the *in vitro* experiment was repeated in a setup which turned out to be the most reliable according to the first two trials. The investigation with identical test conditions and parameters was carried out three times to get more meaningful results (n=3). The gels used had a height of 2 mm, 5 mm and 12 mm, and only magnet type 1 was employed. The number of tubes was reduced to three since each position was measured just once and not duplicated. There was no branching point, which is why the flow rate was set to 1.5 µl/min. The time step was set to 20 minutes, and three conditions were investigated (prior magnet, magnet applied and post magnet). **Table 10** and **Figure 27** depict the conditions and setup that were employed in the third trial.

Table 10: **Experimental setup of the third trial.** Only magnet type 1 was used. The gels had a height of 2 mm, 5 mm and 12 mm. The time step was set to 20 minutes and three conditions were investigated (prior magnet, magnet applied, post magnet).

Experimental setup of the third trial	
Position	**Test run 6**
1	Magnet type 1; Gel= 2 mm
2	Magnet type 1; Gel= 5 mm
3	Magnet type 1; Gel= 12 mm

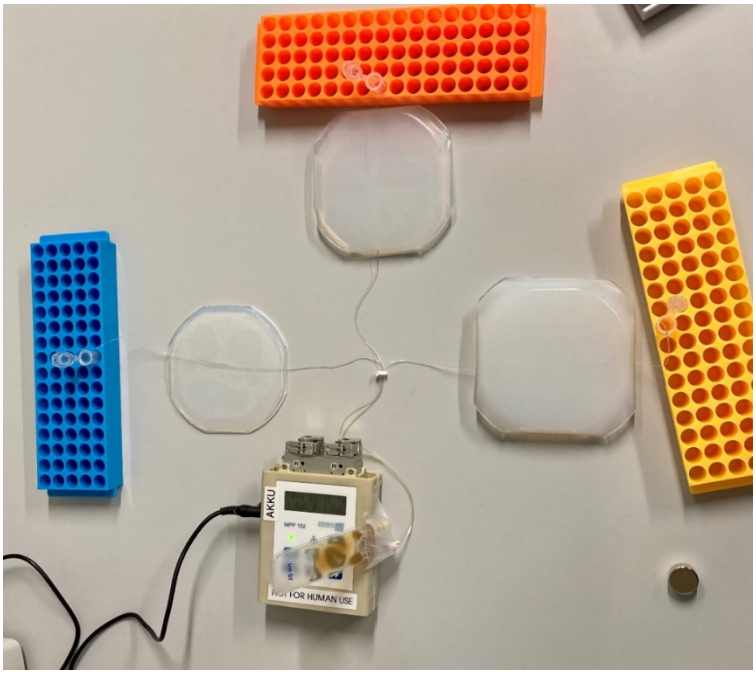

Figure 27: Experimental setup oft the third trial (test run 6). *The arrangement comprises three gels and tubes; the peristaltic pump is located in the middle.*

Ex vivo experiments using porcine skin flaps

Before moving on to the preclinical *in vivo* testing phase, it is essential to ensure that the desired effect can also be achieved with the original barrier, physiological skin. Therefore, an *ex vivo* experiment was conducted. Instead of agarose, porcine skin flaps were used as the barrier in this context. The skin flaps were derived from the trunk region of female domestic pigs (Sus scrofa; 29 kg; Hahnhof Pyrat No.: 8005-A019; 02-Mar.2021). Each of the three flaps measured 8 x 8 cm in length and 1.5 cm in height.

In general, the experimental conditions and parameters were equalized with those of the third trial; however, some adjustments to better fit the available setup and materials had to be included. As in the third trial, three conditions (prior magnet, magnet applied and post magnet) were investigated. Similarly, the number of tubes was three. However, their cross-sectional area was scaled down from 0.25 mm to 0.125 mm, since those tubes had to be implanted into *ex vivo* skin. In the process of that, the different depths of implantation could not be determined precisely prior to implantation but afterwards by means of ultrasound (**Figure 28**). The Perfluoroalkoxy (PFA) tubes (JR Push Tubing SCS001; LOT: LK18H195), which were provided by the institute JOANNEUM RESEARCH HEALTH, had an inner diameter of 0.125 mm and were

implanted using sterile needles (Sterican 20G, B.Braun, Germany). Since the diameter of the tubes was just half as large as the diameter of the tubes used in the *in vitro* experiments (0.25 mm), the flow rate had to be adjusted to remain with a flow velocity of 0.5 mm/sec, which equals the blood flow velocity in microcapillaries. Due to this, the pump rate was set to 0.4 µl/min, and the sampling time was extended to 60 minutes to obtain adequate outflow volumes.

Additionally, since implantation depths greater than 4 mm are not relevant for preclinical testing, the analyzed barrier thicknesses were demagnified. The three examined depths measured 0.95 mm (position 1), 1.93 mm (position 2), and 3.46 mm (position 3). On the first position, where the barrier thickness was minor, magnet type 2 was applied, whereas magnet type 1 was placed on the other positions (**Figure 28**). **Figure 29** shows the experimental setup of the *ex vivo* experiment using porcine skin flaps.

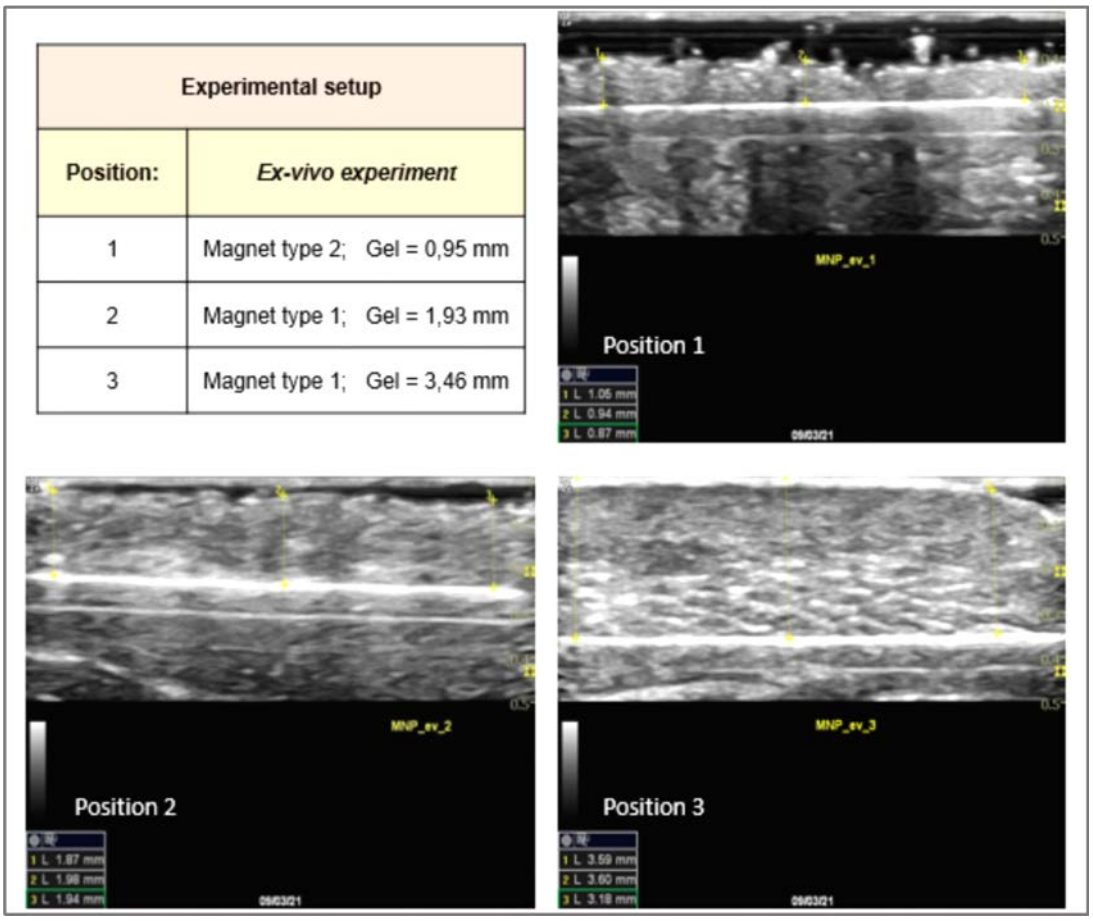

Figure 28: Experimental setup of the ex vivo trial and measurement of the implantation depths using ultrasound at positions 1-3. *Determined depths: Position 1: 1.05 mm, 0.94 mm and 0.87 mm with µ=0.95 mm; Position 2: 1.87 mm, 1.98 mm and 1.94 mm with µ= 1.93 mm and Position 3: 3.95 mm, 3.60 mm and 3.18 mm with µ= 3.46 mm*

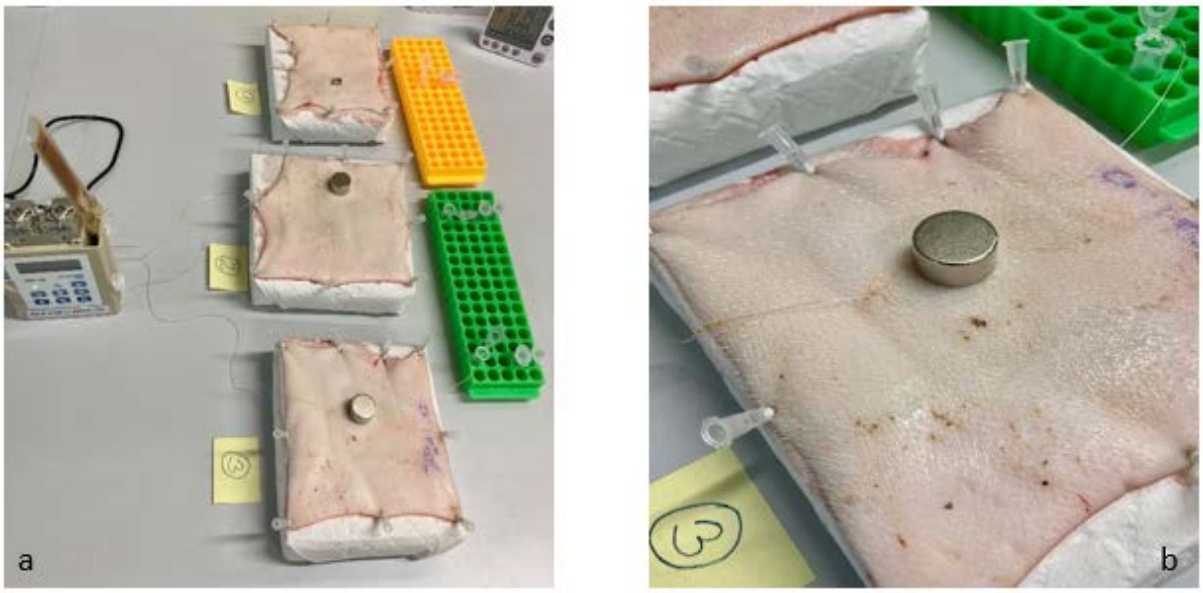

Figure 29: Experimental setup of the ex vivo experiment using porcine skin flaps*. (a) Position 1-3) with magnet type 2 applied on position 1 and magnet type 1 on positions 2 and 3; (b) Position 3 with magnet type 1 applied. The tube was implanted into a depth of 3.46 mm*

Results

Each test run was evaluated by measuring the outflow volume and by quantifying the concentration of magnetic nanoparticles in the outflow solution via the assay of magnetite. Before starting the trials, the system needed approximately 10 minutes to fill up the tubes and reach homogenous and uniform conditions. Even though all tubes had filled up after that time and outflow was observed at all positions, the precise amounts still differed. An exact homogeneity could not be achieved before starting the test runs. However, deviations became negligibly little.

Initial experiment setup

The first trial analyzed six positions, of which three functioned as a blank with no magnet applied at any time. Those blanks (1B-3B) were positioned on the left side of the branching point, whereas the right-sided gels (1M-3M) were used to investigate the applied magnet`s impact. The first condition studied was the condition “prior magnet”, which refers to the first period of interest, in which no magnet was applied on any of the gels. By this, the MNP concentration and volume of the outflow, if no external influences are given, were defined. As expected, the concentration after this condition was not entirely identical with the inflow concentration (0.50 mg/ml) since a certain amount of magnetic nanoparticles was retained/lost in the tubing system. However, this effect was observed at all conditions and in all experimental setups and did not interfere with the results regarding the magnet's impact. For unknown reasons, the left-sided blank tubes were constipated throughout almost the entire trial. Due to this, the values obtained at those positions were not included in the evaluation, as they cannot be considered meaningful.

Test run 1

In the first test run, only two conditions were investigated: “prior magnet” and “magnet applied”. At all three positions, a decrease in the MNP concentration in the outflow after the condition “magnet applied” compared to the concentration after the situation “prior magnet” was observable. The highest difference (0.41 mg/ml vs. 0.16 mg/ml) was achieved at position 2M, which referred to the thinnest gel height analyzed in this test run. The application of the magnet on position 3M also led to a strong decrease in the concentration of magnetic nanoparticles in the outflow (0.43 mg/ml vs. 0.16 mg/ml). At position 1M a MNP concentration of 0.37 mg/ml was measured before applying the

magnet, which decreased to a concentration of 0.26 mg/ml after the application of the magnet on the gel. **Figure 30** shows the MNP concentrations in the respective outflow tubes at the two investigated conditions.

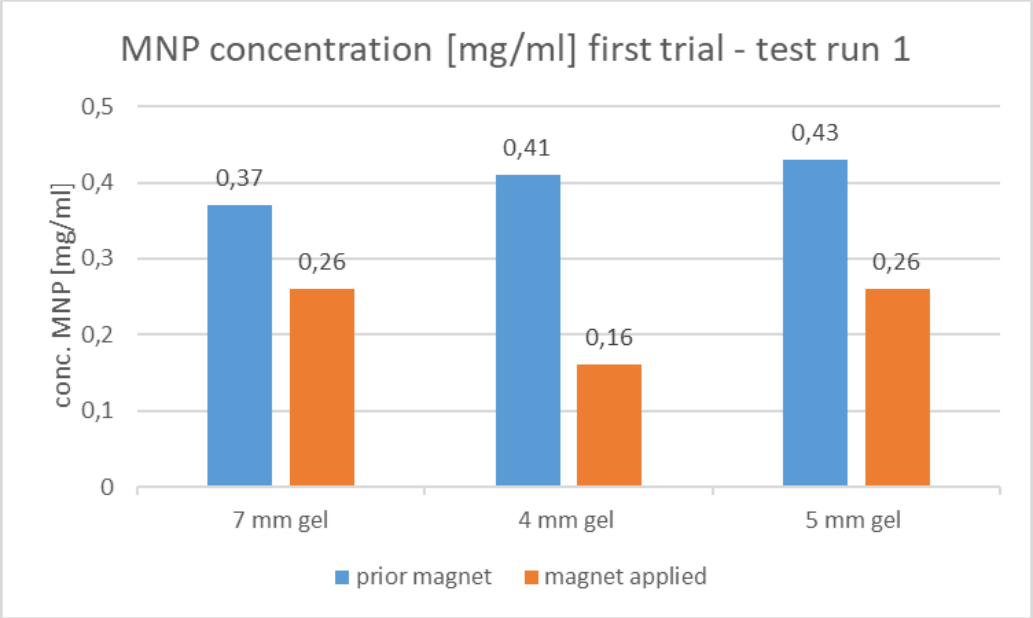

Figure 30: MNP concentrations after the conditions "prior magnet" (blue) and "magnet applied" (orange) in test run 1 (first trial) at each position. *Gel heights analyzed included 7 mm, 4 mm and 5 mm. The highest decrease in MNP conc. between the two conditions was achieved at position 2 (4 mm gel).*

The changes in the flow-through volume were measured by weighing the respective Eppendorf tubes before and after the experiment. The difference between those two weights corresponds to the flow-through volume. The results of this measurement are shown **Figure 31**.

During the first 40 minutes (prior magnet), the outflow in all the Eppendorf tubes varied, even though the conditions at all positions were equal. After the following 40 minutes (magnet applied), the flow-through in all three tubes was reduced. The tube of 1M had a reduced outflow of 12.5 µl, 2M of 14.2 µl, and the tube of 3M of 12.7µl compared to the first condition. Therefore, disregarding the gel thickness, the average reduction in the flow-through volume was 13.1 µl (**Table 11**).

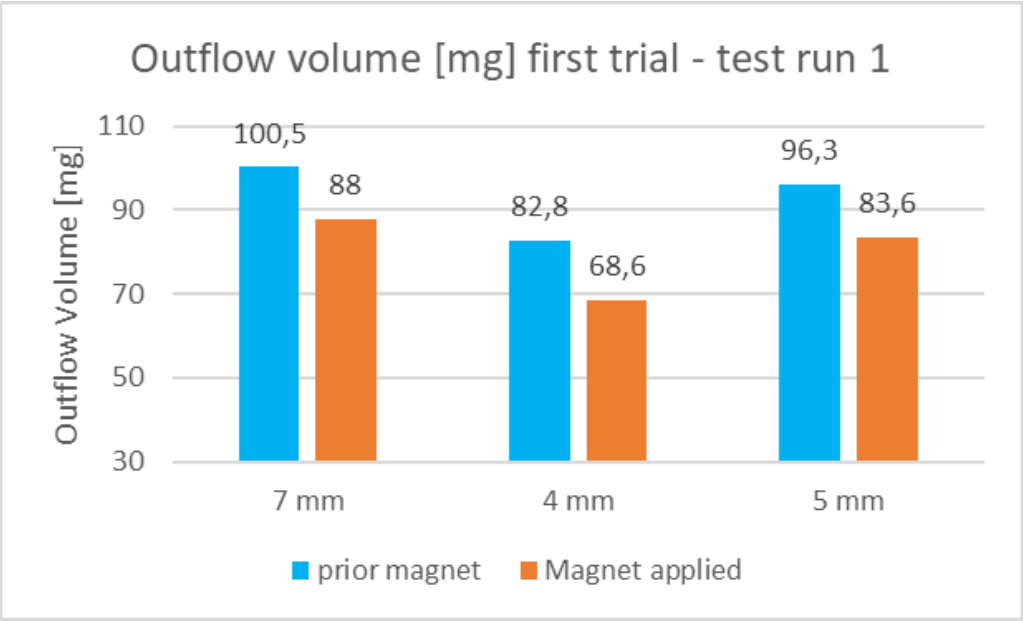

Figure 31: Outflow volumes after the conditions "prior magnet" and "magnet applied" in test run 1 (first trial). *The highest decrease in the flow-through volume was measured at position 2 (4mm gel).*

Table 11: Reduced outflow volume after condition "magnet applied" compared to condition "prior magnet" [µl].

Position	Reduced outflow volume [µl]
1M	12.5
2M	14.2
3M	12.7
Average	**13.1**

After approximately eight minutes, an accumulation of nanoparticles in the tubing system right below the magnets occurred (**Figure 33a**). Since the micro-tubes and the gels were transparent, the aggregation was well visible and held in place below the magnet for approximately ten minutes. After that time, the accumulated MNPs, which appeared as a dark smear, could not be held back anymore and slid further into the Eppendorf tubes. This occurrence was observable first in the tube of 1M, followed by 2M, and finally by 3M. By this, we were able to prove that the magnetic strength of the applied magnets is strong enough to reach the magnetic nanoparticles in the tubing system in all three examined depths.

To include a second evaluation method and thereby excluding a device error of the scale, the volume was additionally measured using a pipette. **Table 12** represents the results thereof. Since this method is not very precise, slight deviations occurred.

However, the results agreed strongly enough to confirm the accuracy of the other method's outcome.

Table 12: Outflow volumes of test run 1 (first trial) [µl] measured using pipettes.

prior magnet	Position	volume [µl]	magnet applied	Position	volume [µl]
	1M	100		1M	85
	2M	80		2M	68
	3M	95		3M	82

Test run 2

The second test run included a third condition (post magnet). Furthermore, by shortening the time step from 40 to 15 minutes, we aimed at achieving more meaningful results since the outflow tubes were changed before the accumulated nanoparticles' smear slid on. The tubes of the positions 1B-3B were still constipated for unknown reasons. The outflow volume of those three tubes was at all three conditions significantly reduced compared to the positions 1M-3M. Therefore, those three positions' results cannot be considered meaningful and were again excluded from the evaluation.

The MNP concentration measurement showed the same trend as in the first test run. Before positioning the magnets on the gels, the MNP concentration was around 0.42 mg/ml. However, after the application of the magnets, the concentration of magnetic nanoparticles decreased drastically at all three positions. In general, the concentrations were about two to four times lower after the application of the magnets. The lowest concertation (0.14 mg/ml) was achieved at the position 2M, followed by a concentration of 0.16 mg/ml at position 1M. The smallest difference after the two first conditions was measured at position 3M (0.22 mg/ml after “magnet applied”).

The third condition analyzed, which referred to the concentration measurement after removing the magnets again (post magnet), resulted in the highest MNP concentrations so far. The obtained values exceeded the initial starting concentration of 0.50 mg/ml. The highest concentration was reached at the position 2M (0.67 mg/ml), followed by 3M (0.65 mg/ml), and also at position 1M (0.55 mg/ml) a strong increase was measured. The results of the MNP measurement are shown in **Figure 32.**

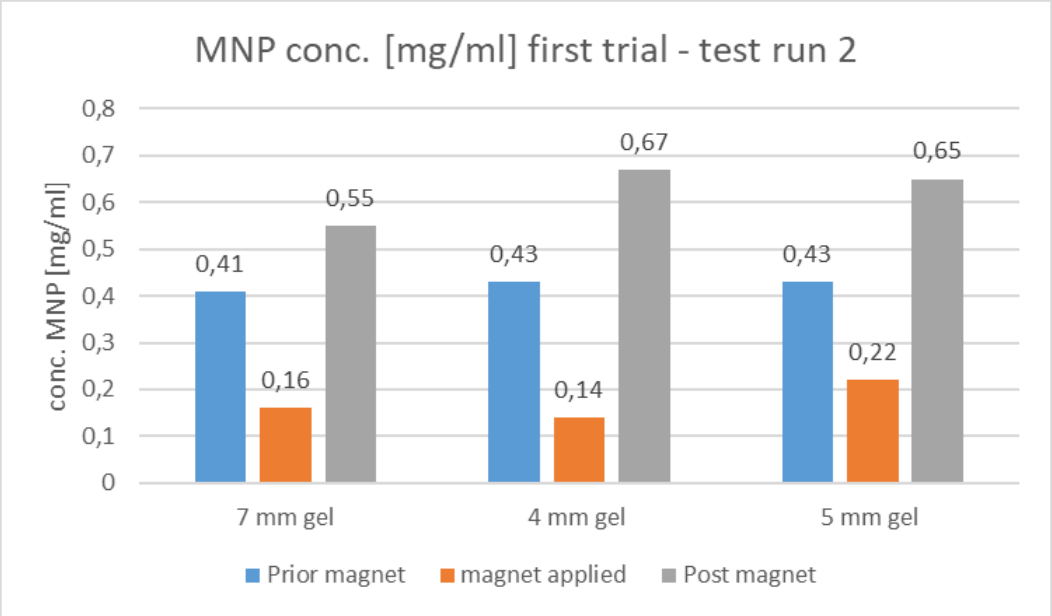

Figure 32: MNP concentrations after the conditions "prior magnet", "magnet applied" and "post magnet" in test run 2 (first trial) at each position. *The highest differences in the MNP conc. after applying/removing the magnet were achieved at position 2 (4 mm gel).*

As in the first test run, a visible retention of MNPs below the applied magnets was achieved (**Figure 33a**). The shorter time step of just 15 minutes in test run 2 aimed at achieving that the nanoparticles are kept in the agglomerated conformation until the magnets are removed again. Consequently, the amount of MNPs in the outflow tubes during the condition “magnet applied” was significantly reduced, whereas in the following condition “post magnet” the amount of MNPs increased again. Since not only the nanoparticles that were transported due to the usual flow within 15 minutes, but also the restrained nanoparticles from the condition before concentrated in that tube, the amount of the MNPs in the outflow tubes reached their maxima after this condition. In **Figure 33b**, the outflow tubes with the obtained MNPs solutions are shown. The colour intensity of the liquid refers to the amount of magnetic nanoparticles contained. **Figure 33a** depicts the visible agglomeration of magnetic nanoparticles in the tubing system below a magnet.

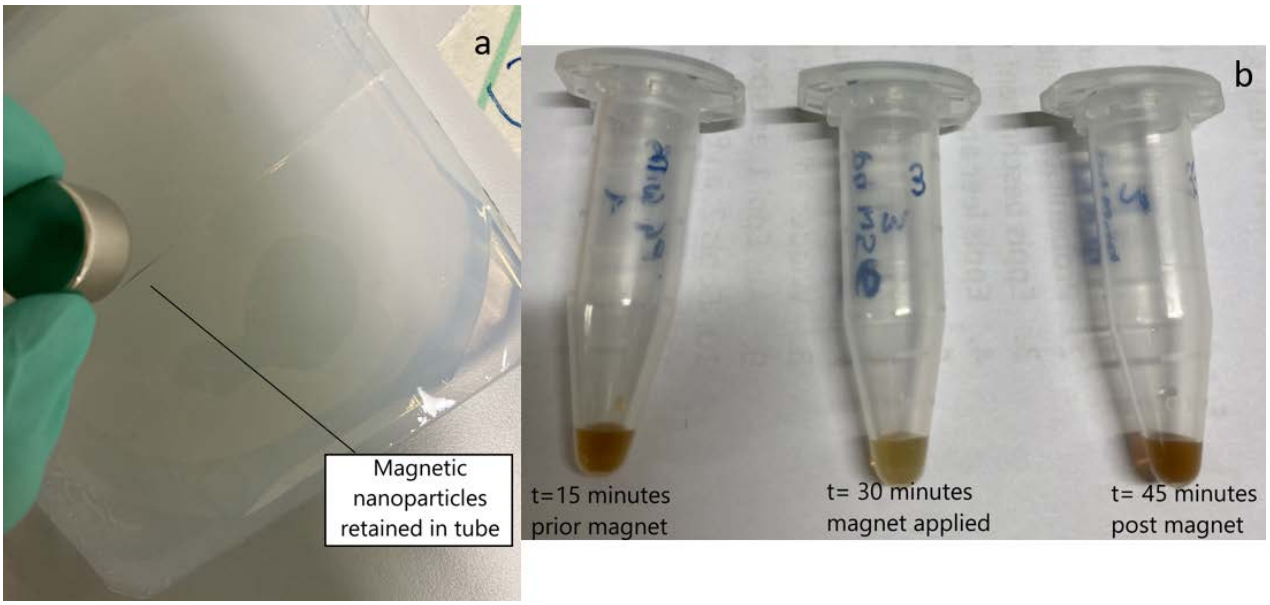

Figure 33: Magnetic nanoparticles. *(a) The visible agglomeration of magnetic nanoparticles in the tubing system below a magnet. (b) Outflow tubes with the obtained MNPs solutions after the three different conditions. The colour intensity of the liquid refers to the amount of magnetic nanoparticles contained.*

The results of the volume measurement of the second test run revealed a different trend than those of the first test run. The outflow volume of 1M-3M at the condition "prior magnet" lay between 38-41 µl. During condition "magnet applied", the outflow volumes increased to 39-42 µl and the highest outflow volumes were measured after condition "post magnet" (40-44 µl).

Whereas a decrease in the volume after applying the magnet on the gel was observed in test run 1, an increase occurred in the second test run. The third condition "post magnet", which reached the maximum values at all positions, was not included in test run 1. Therefore, no comparison of the two test runs regarding this condition was possible. **Figure 34** depicts the volumes and results obtained at each position. **Table 13** refers to the volume measurement using a pipette.

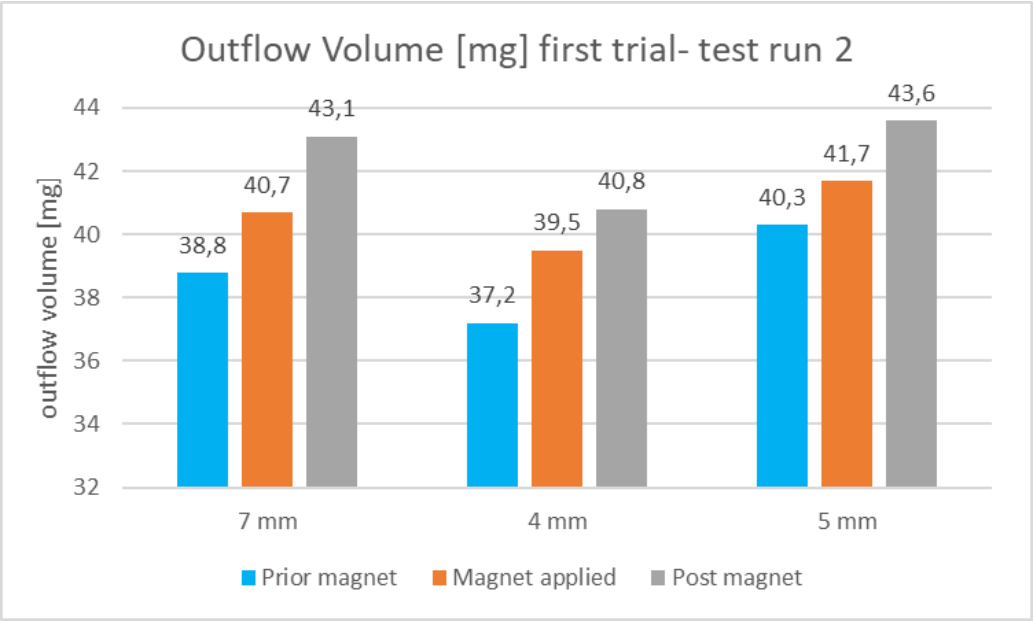

Figure 34: Outflow volumes after the conditions "prior magnet", "magnet applied" and "post magnet" in test run 2 (first trial). *At all positions the volumes increased continuously from the first to the third condition.*

Table 13: Outflow volumes of test run 2 (first trial) [µl] measured using pipettes.

Prior magnet	Position	volume [µl]	Magnet applied	Position	volume [µl]	Post magnet	Position	volume [µl]
	1M	37		1M	39		1M	41
	2M	36		2M	38		2M	40
	3M	40		3M	41		3M	43

Refine tubing

The second trial aimed at addressing the error sources that emerged in the first trial. Accordingly, some alterations to minimize those imperfections were introduced. The branching point was excluded since it became apparent that it might act as a source of error. However, it was attempted to quantify the rising pressure, which eventually builds up due to occlusions of the tubes caused by MNP aggregations, using pressure sensors that were integrated into the tubes. The pressure that built up could not reach the detection limits that would have been needed to propose scientific hypotheses based on the outcome. A detailed evaluation of the pressure sensor data was, therefore, not conducted.

Since there was no clear and significant relationship between the investigated gel thicknesses and the magnetic capture in the first trial, higher gel thicknesses were investigated. Thereby, the decrease of magnetic capture with increasing gel depth was analyzed, which is essential for the preclinical testing phase.

The second trial comprised three independent test runs, whereof the fourth and fifth refer to more experimental setups, which mainly aimed at studying different constructions, even though they do not refer to intended, first choice setups for the preclinical testing.

Test run 3

The third test run was measured in duplicates, which means that the six gels were not separated into three positive and three negative controls but consisted of three different conditions that were measured in a double approach. Therefore, the results depicted in **Figure 35** refer to the average values.

Compared to the first trial, the condition "prior magnet" achieved more consistent results in this test run (0.46 mg/ml – 0.47 mg/ml), and the values approached more to the concentration of the inflow solution. After the following condition, the values decreased at all positions. The decline was the most significant at position 1 (0.47 mg/ml to 0.23 mg/ml), where magnet type 2 was applied, and the gel had a diameter of just 2 mm. In contrast to that, the gel at position 3 had a diameter of 12 mm. Even though this was the highest barrier thickness investigated, it was not the position were the retention was the least efficient. At the second position, where the gel had a diameter of 7 mm, the decrease in the concentration was less. However, those two positions' values resembled, whereas they were far apart from the value obtained at position 1.

In this test run, the concentration reached its maximum values after the third condition, "post magnet". The highest concentration was measured at position 3 (0.63 mg/ml), followed by position 1 (0.59 mg/ml) and position 2 (0.57 mg/ml). The trend was the same at all positions and paired up with the expected tendency.

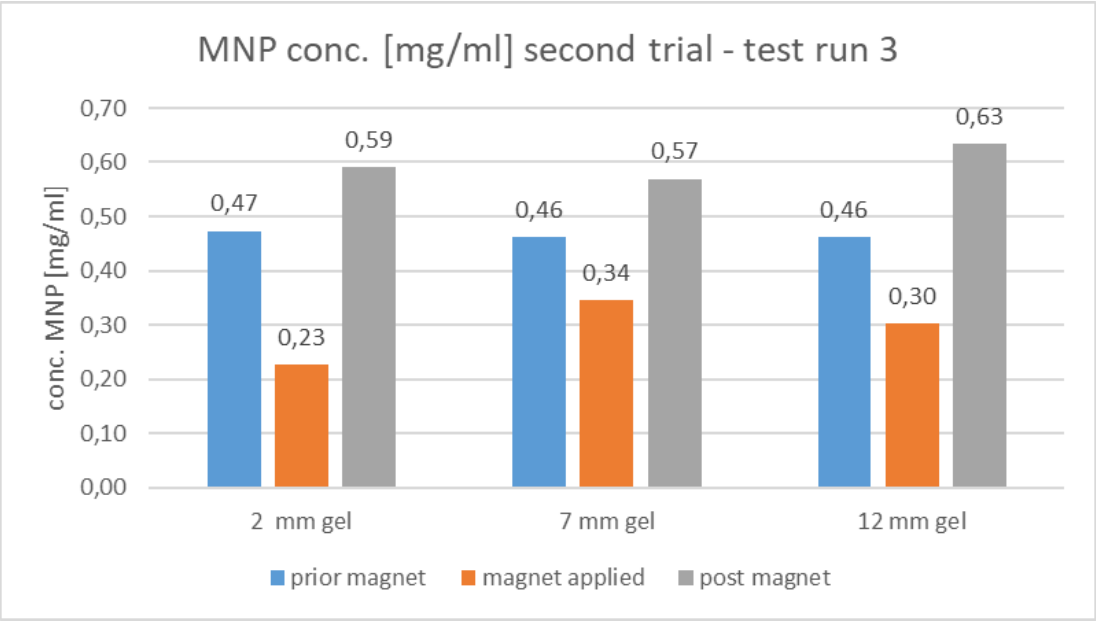

Figure 35: MNP concentrations after the conditions "prior magnet", "magnet applied" and "post magnet" in test run 3 (second trial). *The highest differences in MNP conc. after applying/removing the magnet were achieved at position 1 (2 mm gel).*

The volume measurement of the third test run showed unexpected results. The outflow volume at the condition "prior magnet" was the lowest at all three positions. The values reached their peak after "magnet applied" and decreased again to lower values around 28 µl after the final condition "post magnet".

In **Figure 36**, the volume measurement results are depicted. **Table 14** refers to the volume measurement using pipettes.

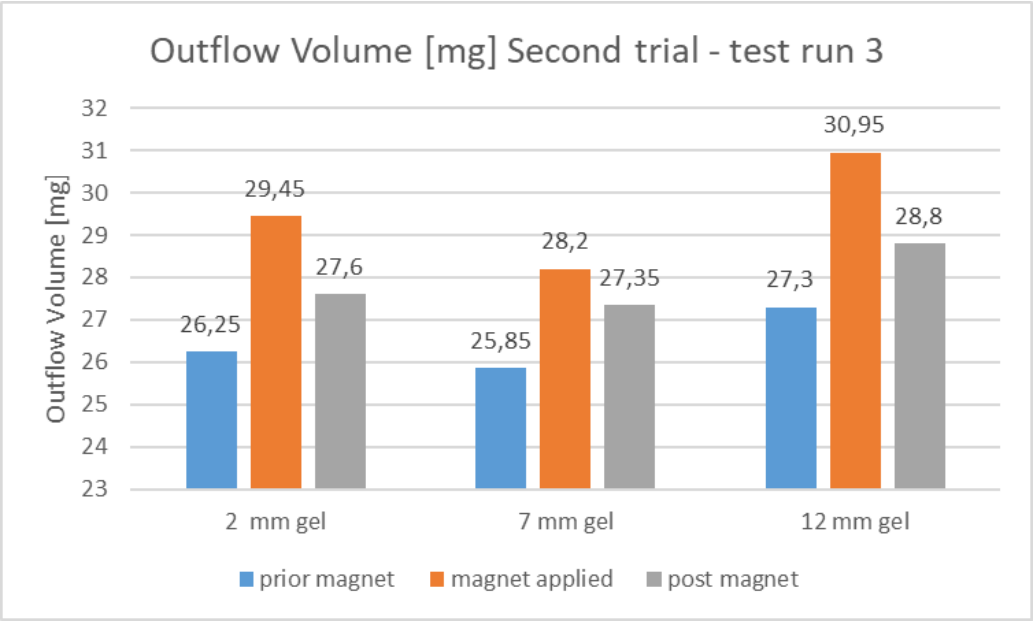

Figure 36: Outflow volumes after the conditions "prior magnet", "magnet applied" and "post magnet" in test run 3 (second trial). *At all positions, the volumes increased at the condition "magnet applied" and decreased again during the third condition.*

Table 14: Outflow volumes of test run 3 (second trial) [ml] measured using pipettes.

	d [barrier]	volume [µl]		d [barrier]	volume [µl]		d [barrier]	volume [µl]
prior magnet	2 mm	27	magnet applied	2 mm	28.5	post magnet	2 mm	26.75
	7 mm	22.5		7 mm	27.75		7 mm	27.25
	12 mm	26.5		12 mm	30.3		12 mm	28.75

Test runs 4 & 5

Those two test runs refer to some experimental setups that mainly aimed at evaluating the different impacts of the applied magnet types. Therefore, in addition to magnet type 2, magnet types 1 and 3 were also applied on the first position that referred to the thinnest investigated barrier thickness. Additionally, magnet type 3 was applied on the third position (12 mm gel), and the tube at the second position was squeezed between two medium-sized magnets to evaluate a double-sided exposure to magnetic capture. The results of those experimental setups are briefly presented below.

Concerning the three different magnet types positioned on gel 1, it can be said that the highest retention was achieved with magnet type 1, followed by magnet type 3 (**Table 15**).

Table 15: MNP concentrations [mg/ml] after the application of the three magnet types 1-3 at position 1 with a barrier thickness of 2 mm. *The highest concentration decrease was achieved with magnet type 1, followed by magnet type 3. The smallest magnet (type 2) led to the highest MNP concentration.*

	Magnet type applied	conc. MNP [mg/ml]
Position 1	1	0.15
	2	0.23
	3	0.20

On the third position (barrier thickness of 12 mm), magnet types 1 and 2 were examined. The best retention was achieved by magnet type 2, resulting in an outflow concentration of 0.20 mg/ml compared to a 0.30 mg/ml concentration achieved by magnet type 1.

The effects of the double-sided exposure to magnetic capture also showed an increase in MNP retention compared to a single-sided exposure (0.23 mg/ml vs 0. 34 mg/ml) at position 2.

The impacts on the flow-through volumes were less significant at all examined conditions. However, the results can be considered successful. The test runs have shown that magnet type 1 led to eligible retention at all positions.

Repeat experiment

Test run 6

The third and last trial of the *in vitro* testing phase comprised just one experimental setup, which appeared to be the most reliable and meaningful according to the first and the second trial. It included three instead of six tubes implanted into depths of 2 mm, 5 mm and 12 mm. As already mentioned, only magnet type 1 was used, and the time was again set to 20 minutes. The three conditions “prior magnet”, “magnet applied”, and “post magnet” were measured three times to achieve meaningful results (n=3).

At the condition “prior magnet,” an average MNP concentration of 0.41 mg/ml was achieved. As already observed in previous test runs, this concentration is to some extent lower than the MNP concentration in the inflow. However, this probably occurred in all investigated conditions and did not falsify the results.

After applying the magnets on the gels, a drastic concentration decrease was measured. The average value was 0.05 mg/ml, which increased again to very high concentrations after removing the magnets (0.73 mg/ml). This time the maximum retention was achieved at position 2, followed by position 3. The results are depicted in **Figure 37**.

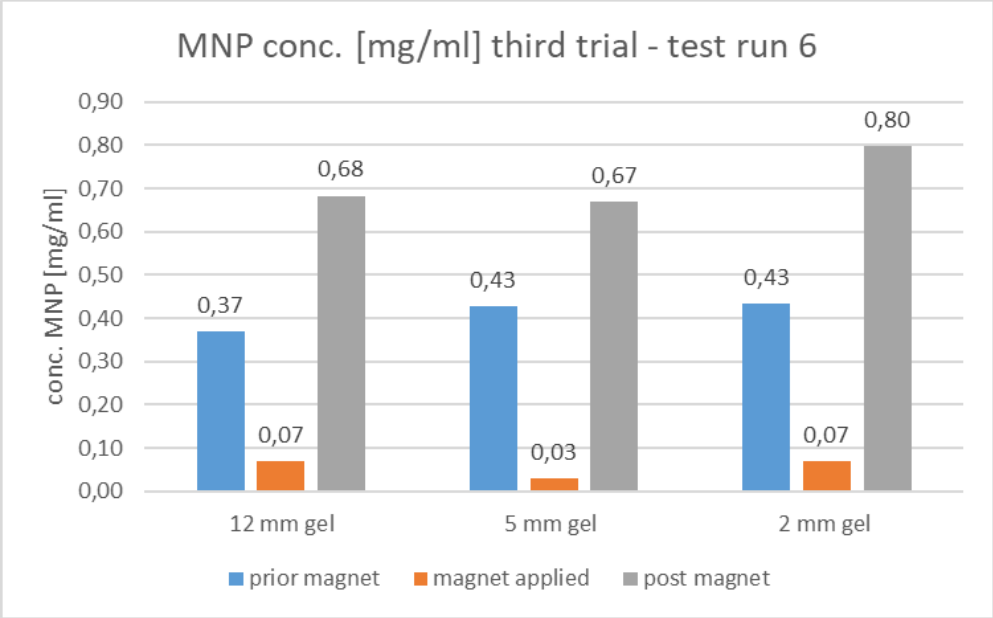

Figure 37: Average MNP concentrations after the conditions "prior magnet", "magnet applied" and "post magnet" in test run 6 (third trial). *At all three positions, a drastic decrease in the MNP conc. was measured when the magnets were applied. After removing them again, the values increased and reached the maximum concentrations.*

The volume measurement showed a similar trend as in the third test run. At positions 2 and 3, the outflow volumes were lowest after the first condition, increased to their maximum values after the following situation and decreased again after the last condition. Those results resembled the values obtained in the third test run. At position 1, the outcome resembled that of the first trial. The volume increased at the condition “magnet applied”, but subsequently decreased again. The results of the outflow volume measurement are presented in **Figure 38**.

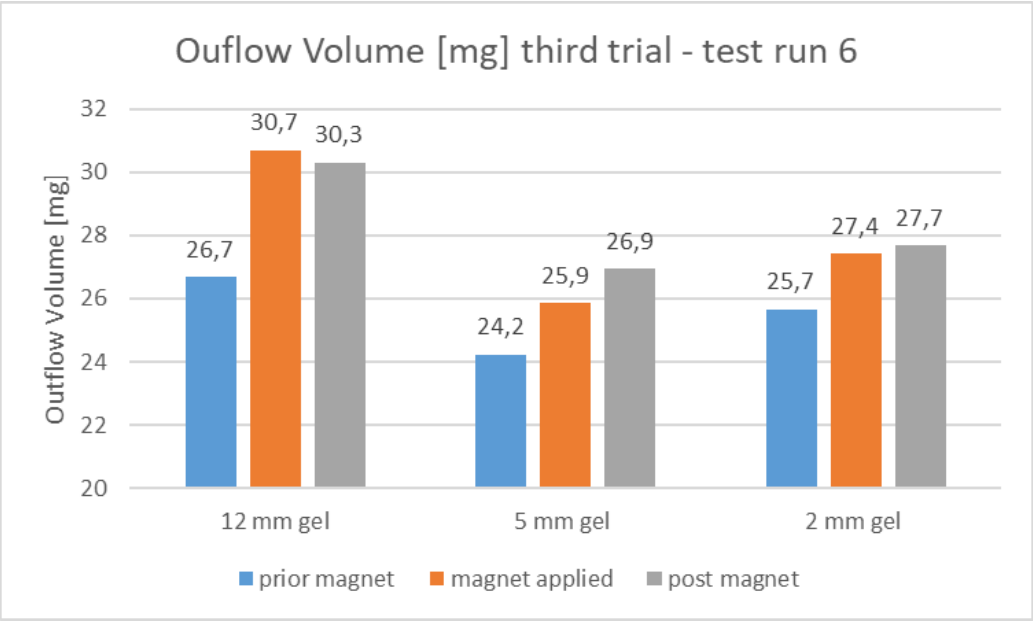

Figure 38: Average outflow volumes after the conditions "prior magnet, "magnet applied" and "post magnet" in test run 6 (third trial). *The outcome resembles that obtained in the first (position 1) and second (position 2 and 3) trial.*

Ex vivo experiment using porcine skin flaps

Before moving on to the preclinical *in vivo* testing phase, it is essential to ensure that the desired effect can also be achieved with the original barrier, physiological porcine skin. Therefore, an *ex vivo* experiment using porcine skin flaps was conducted.

In the course of the *ex vivo* trial, it could be shown that the desired trend regarding the MNP concentration also sets in an experimental setup that includes porcine skin as the barrier. At all three positions, the initial concentration decreased when the magnets were applied and increased to higher values after removing them again. At the second position, where the tube was implanted approximately 2 mm deep into the skin and magnet type 1 was applied, the effect was the most significant. At the other two positions, the results were still explicit. However, one can notice the minor impact of an increased depth and a smaller-sized magnet. Both parameters seem to impair the outcome to a similar extent. The primary idea to proceed with magnet type 1 to the preclinical testing phase was thereby validated. **Figure 39** depicts the results of the MNP concentration measurement of the *ex vivo* experiment using porcine skin flaps.

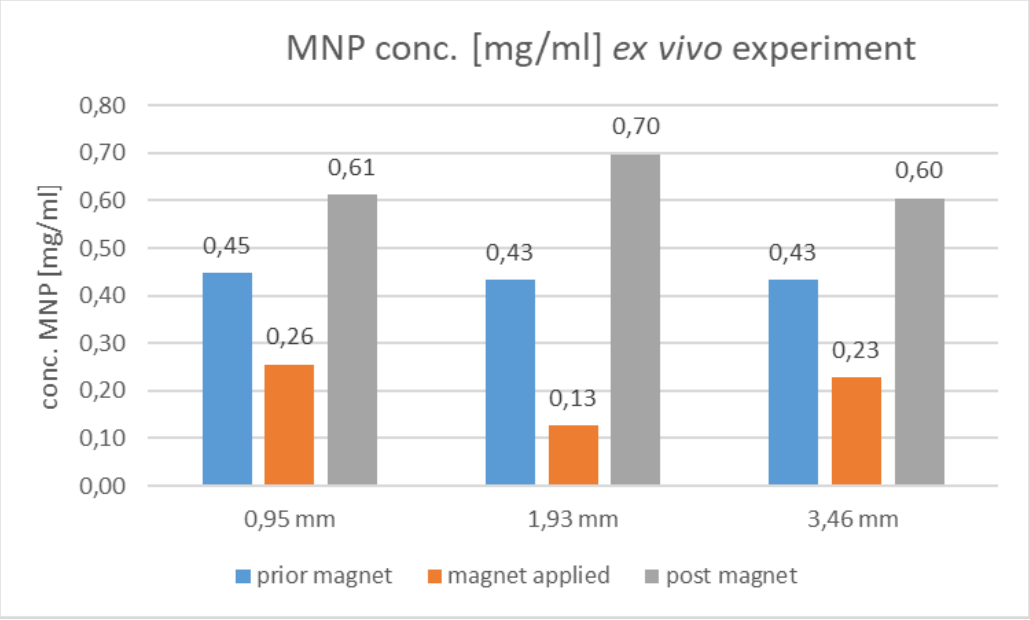

Figure 39: Average MNP concentrations after the conditions "prior magnet", "magnet applied" and "post magnet" in the ex vivo experiment. *At all three positions, the MNP conc. decreased when the magnets were applied and increased again after removing them. The highest differences in the MNP concentrations were measured at position 2, where magnet type 1 was applied.*

The results of the volume measurement, which are shown in **Figure 40**, mostly resembled the outcome of the previously conducted third *in vitro* trial. The desired trend only settled at the second position. There, the volume decreased when the magnet was applied and increased to the maximum value after the removal of the magnet. Even though the differences are minor, the desired trend established. At the other two positions, this course was not observable. Instead of a decrease in the outflow volume after the third condition, an increase was measured. This outcome was already obtained before in some of the *in vitro* test runs.

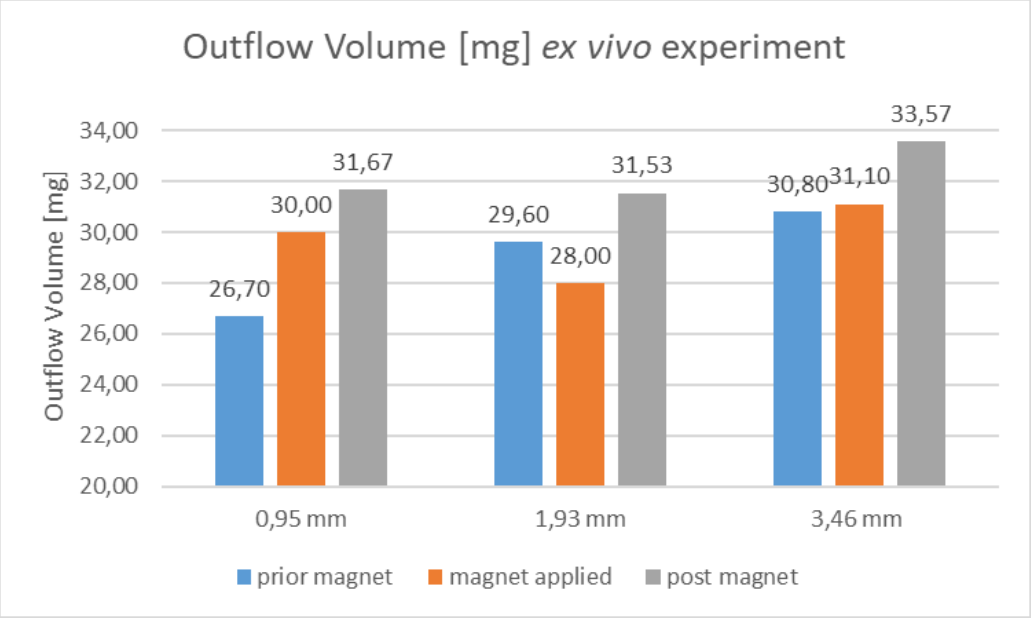

Figure 40: Average outflow volumes after the conditions "prior magnet", "magnet applied" and "post magnet" in the ex vivo experiment*. Different trends established at the investigated positions.*

Discussion

In vitro tests

The first trial aimed at allowing an estimation of the quality and meaningfulness of the experimental design. The goal was to observe a possible influence of the magnets on the magnetic nanoparticles in solution, which were pumped through the tubing system. The evaluation was done via MNP concentration measurement as well as outflow volume measurement. The *in vitro* experiments have successfully shown that the magnets are able to reach the magnetic nanoparticles in all examined depths. Especially the results of the measurement of the MNP concentration were explicit. In all the test runs the concentration of magnetic nanoparticles was decreased whenever magnets were applied.

In each test run of the first trial, an impact of the magnets on the concentration of magnetic nanoparticles in solution was observable. The apparent trend showed that the initial concentration at the condition “prior magnet” decreased if the magnets were placed on the gels. Additionally, in the second test run, it was shown that the MNP concentration increased again and even reached the maximum values after subsequently removing the magnets (post magnet). This outcome displays the desired expectations. A clear influence of the magnets onto the flow behaviour of the magnetic nanoparticles was detectable. The nanoparticles were retained due to the exposure to the magnets’ magnetic forces. Since this first goal was achieved and complied with the requirements, further preliminary tests with slightly changed parameters were planned to optimize the experimental setup.

The interpretation of the volume measurement results was more challenging since there was no clear trend observable. Whereas a decrease in the outflow volume after applying the magnets on the gels was observed in test run 1, an increase occurred in the second test run. The third condition “post magnet”, which reached the maximum values at all positions, was not included in test run 1. Therefore, no comparison of the two test runs regarding this condition was possible. However, the small increases from condition 1-3 in the second test run are probably results of unintended deviations due to imperfections in the setup rather than the applied magnet's consequence. Further reasons for this are hard to define, but in general, it implies that the chosen time step of 15 minutes was too short to see meaningful changes in the outflow volume, as it

was possible in the first test run with the time step of 40 minutes. Even though the differences in the volumes in the first test run did not deviate considerably, they still imply a significant impact. It can be assumed that the reduced volume is a consequence of the retention of the MNPs and the tube's temporary constipation.

During both test runs, it was not possible to obtain equal results among the samples being exposed to the identical conditions. For unknown reasons, the left-sided tubes 1B-3B showed, right from the beginning, less flow-through than the right-sided tubes (1M-3M). Due to this, those samples were not included in the evaluation since they cannot be considered meaningful.

Since this trial refers to the first proof-of-principle tests of this kind, the experimental setup had some imperfections, leading to an inconsistency in the results. The tubes used were not fully compatible with the Y-connectors and had to be glued together using a UV-based glue. It is possible that unintended dead volume was created by this. Other sources of errors may have been that the tubes had leaks and different amounts of air got into the tubes, or other contaminations that caused constipation. Consequently, the second and third preliminary dummy experiments were conducted with some alterations addressing those issues in the experimental setup.

Since the barrier thicknesses investigated in the first trial did not enable the identification of a meaningful correlation between the gel thickness and the achieved magnetic capture, higher barrier thicknesses were included into the second trial, aiming at observing a decrease of magnetic capture with increasing gel depth. Accordingly, it could be shown that the position with the thinnest gel depth (2 mm) led to the most efficient MNP retention. However, subsequent to that, position 3, where the gel had a diameter of 12 mm, achieved the second highest MNP retention. At the second position, where the gel had a diameter of 7 mm, the decrease in the MNP concentration was the lowest. However, those two positions' values resembled, whereas they were far apart from the value obtained at position 1. That indicates that the retention of the magnetic nanoparticles increases with a decreasing barrier thickness. However, the differences in the gel thicknesses must be significant and far enough apart from each other to see consequences. The diameters of 7 mm and 12 mm both refer to very thick barriers that are too similar to achieve meaningful results.

In general, it was possible to identify a correlation between the gel thickness and the achieved magnetic capture.

The results of the outflow volume measurement were again difficult to interpret. They indicate that the time step of 20 minutes was too short to show an effect of the magnets on the flow-through volume, as they affected the MNP concentration. Another explanation can be that the magnetic strength of the applied magnets attracted the nanoparticles in solution in a way that led to an increased travel velocity of the solution in the tubing system towards the magnets. However, that effect was not observed in the first trial.

In addition to the third test run, two other setups were investigated in the second trial. The fourth and fifth test run refer to experimental designs, which mainly aimed at studying different constructions, even though they do not refer to intended, first choice setups in the preclinical testing. The prime goal of the two test runs was to evaluate the differing impacts of the applied magnet types. Consequently, all of the three magnet types were analyzed and compared. The outcome revealed that magnet type 1 led to the highest retention, followed by magnet type 3. In general, magnet type 1 led to eligible retention at all positions. This supports the idea to proceed only with the medium-sized magnets. Since those also have the best dimensions regarding the experimental mounting of the subsequent testing phases, they are also the ones that are planned to be used in the preclinical testing. In contrast, a double-sided magnetic capture is not applicable in the preclinical testing and was, therefore, more of an additional setup due to personal interest.

Overall, the second trial revealed satisfying results. A correlation between the barrier thickness and a decreasing magnetic capture was detectable. Additionally, it could be shown that magnet type 1 achieves an eligible retention of magnetic nanoparticles. Subsequently, a third trial of *in vitro* experiments was conducted in a setup, which included conditions that were most reliable according to the first two trials.

In this last *in vitro* trial, a drastic concentration decrease was measured, when the magnets were applied on the gels. The average value was 0.05 mg/ml, which increased again to very high concentrations after removing the magnets (0.73 mg/ml). Even though the results of the third trial show the same trend as the results of the previous test runs, the obtained values were much lower. By reaching concentrations

below 0.1 mg/ml, the magnetic nanoparticles' retention was by far more efficient than before. Although that is desirable for our further proceeding, it is also hard to interpret the deviations between the different trials. Especially the third and the sixth test run resembled closely but still led to varying results. Reasons for that are hard to define. However, since the trend remained the same and desired conditions were observable, a proceeding to the next testing phase was justified.

The results regarding the outflow volume resembled the values obtained in the third test run. The volume was lowest after the first condition, increased to the maximum values after the following situation and decreased again after the last condition. Even though they did not show the trend we hoped to achieve, they can eventually be explained by the short sampling time of 20 minutes. However, since no comparative data was found in the literature, the precise reason cannot be given with certainty. Though, the measurement of the MNP concentration proved that the magnets are able to reach the magnetic nanoparticles through the barriers and that they significantly affect the flow behaviour thereof. The principle feasibility of the method is thereby guaranteed.

Ex vivo experiment using porcine skin flaps

The *ex vivo* experiments aimed at ensuring that the desired trend can also be achieved with the original barrier - porcine skin. This goal was achieved since the course of the magnetic nanoparticle concentration in the outflow throughout the experiment matched the one of the *in vitro* trials. Accordingly, the desired trend regarding the MNP concentration also set in an experimental setup that included porcine skin as the barrier instead of agarose gels. Since the investigated depths were to some extent smaller than those of the *in vitro* trials, the smaller sized magnet (magnet type 2) was applied again at the first position (~1 mm deep).

At all three positions, the initial MNP concentration decreased when the magnets were applied and increased to higher values after removing them again. This was the most significant at the second position, where the tube was implanted approximately 2 mm deep into the skin and magnet type 1 was applied. At the other two positions the results were still explicit. However, one can notice the minor impact of an increased depth and a smaller-sized magnet. Both parameters seem to impair the outcome to a similar

extent. The primary idea to proceed with magnet type 1 to the preclinical testing phase was thereby validated.

Concerning the volume measurement, the desired course only settled at the second position. Even though the differences are minor, the volume decreased when the magnets were applied and increased to their maximum values after the removal of the magnets. At the other two positions, another trend established that was already observed in some of the *in vitro* test runs and is probably caused by the short sampling time step in combination with the suboptimal setup at those two positions compared to position 2. However, position 2 grants the utmost importance for the further proceeding in this study project, since it refers to an implantation depth that covers the region of interest regarding the subsequent *in vivo* application. Consequently, the outcome can be considered satisfying.

The results also state that skin does indeed have a higher barrier function than the previously used agarose gels. Reasons for that lie in the density differences of the associated material and the skin's unique composition and structure. Its general structure, hair follicle content, pigmentation, and collagen and lipid composition make skin a very complex tissue [26]. Simple agarose gels are not a precise imitation of original porcine skin. Therefore, identical results should not be expected. A comparison with already existing data from the literature cannot be made here since, to our knowledge, this method has not yet been applied.

Conclusion

In conclusion, the *in vitro* as well as the *ex vivo* experiments have successfully shown that the method can be considered promising. In both setups, the magnets impacted the flow behaviour of the magnetic nanoparticles in solution. According to the results, magnet type 1 features the most suitable properties and is strong enough to efficiently reach all relevant capillaries in porcine skin. The conditions and materials at the second position in the *ex vivo* trial greatly resemble those of the following *in vivo* study. Accordingly, the success achieved at this position was very important and suggests great potential in the method. The proceeding to the preclinical phase is justified and the foundation for the establishment of a novel technique of producing ischemia in skin has been laid.

Final conclusion and integrative interpretation of the results of the two projects

The goal of establishing a novel ischemic wound model is a large and extensive project that requires a lot of preparatory work as well as many preliminary tests. In the course of this master`s thesis, the development of an ischemia model that uses magnetic nanoparticles to occlude blood flow in microcapillaries, allowing precise spatiotemporal control, but without the need of surgical intervention, was planned and started. This occlusion should be achieved via neodymium-iron-boron (NdFeB-) magnet-mediated aggregation of specific superparamagnetic nanoparticles within defined microcapillaries. To be able to establish such an innovative model, preliminary tests are necessary. Consequently, within this master`s thesis two issues that are essential to be resolved in the development of this large project were planned, designed and carried out. Firstly, a detailed analysis of the porcine skin in the back region was performed on a histological as well as molecular level. With that it was possible to identify region-related differences in the thickness of porcine skin, as well as in gene expression patterns of certain skin-related genes. Secondly, entirely novel *in vitro* and *ex vivo* models were designed and constructed, which have proven that the method of producing ischemia in skin using magnetic nanoparticles is feasible and a proceeding to the next testing stage is justified. With the results of the two studies, the following *in vivo* phase can now be planned precisely and reliably.

The proof of principle experiments using magnetic nanoparticles have shown that magnet type 1 (medium-sized magnet) can effectively reach all microcapillaries that are located in the examined region of porcine skin. In the *ex vivo* experiment, magnet type 1 was applied at the second position, where an implantation depth of approximately 2 mm was given. Since the histological measurement of the skin thickness revealed that domestic female pigs have an average skin thickness of around 2 mm, magnet type 1 should definitely be capable of reaching into the depths of the desired microcapillaries. In addition, in the anatomical site differences project, certain areas were identified, in which the skin is in principle rather thin. In those areas it should be even easier for the magnet to reach the desired capillaries. Especially the lumbar region and most of the medial sites were found to be thinner and can therefore be considered preferred. In addition, also the results of the gene expression assays can

be included in the selection of suitable sites. However, the location related differences in the gene expression levels of the examined genes were rather small. Nevertheless, especially the vascularization factors can be important, as these are indicators of the amount and number of blood vessels in the tissue. *VEGFA* was expressed significantly higher in the lateral area. In addition, there was a trend that the expression is somewhat increased in the lumbar region. Consequently, the area of the loin could be interesting for the application of this novel technique of producing ischemia in skin, since also the skin thickness there is usually rather thin.

In addition, the results of the anatomical site differences project are not only of interest for this specific purpose, but can also become important in the planning of many different *in vivo* experiments using the animal model, pig. For this reason, both projects can be regarded as successful, as they provide the necessary data and information and thereby lay the foundation for the establishment of a novel ischemic wound model.

References

[1] A. Summerfield, F. Meurens, and M. E. Ricklin, “The immunology of the porcine skin and its value as a model for human skin,” *Molecular Immunology*, vol. 66, no. 1. Elsevier Ltd, pp. 14–21, Jul. 01, 2015. doi: 10.1016/j.molimm.2014.10.023.

[2] E. Proksch, J. M. Brandner, and J.-M. Jensen, “The skin: an indispensable barrier,” *Experimental Dermatology*, vol. 17, no. 12, pp. 1063–1072, Dec. 2008, doi: 10.1111/j.1600-0625.2008.00786.x.

[3] P. M. Elias, “The skin barrier as an innate immune element,” *Seminars in Immunopathology*, vol. 29, no. 1. Springer, pp. 3–14, Apr. 30, 2007. doi: 10.1007/s00281-007-0060-9.

[4] A. Matejuk, “Skin Immunity,” *Archivum Immunologiae et Therapiae Experimentalis*, vol. 66, no. 1. Birkhauser Verlag AG, pp. 45–54, Feb. 01, 2018. doi: 10.1007/s00005-017-0477-3.

[5] E. A. Grice and J. A. Segre, “The skin microbiome,” *Nature Reviews Microbiology*, vol. 9, no. 4. Nature Publishing Group, pp. 244–253, Apr. 16, 2011. doi: 10.1038/nrmicro2537.

[6] “Skin: The Human Body’s Largest Organ | Live Science.” https://www.livescience.com/27115-skin-facts-diseases-conditions.html (accessed Mar. 21, 2021).

[7] “Basal lamina scaffold-anatomy and significance for maintenance of orderly tissue structure - PubMed.” https://pubmed.ncbi.nlm.nih.gov/4614671/ (accessed Mar. 21, 2021).

[8] J. M. Abdo, N. A. Sopko, and S. M. Milner, “The applied anatomy of human skin: A model for regeneration,” *Wound Medicine*, vol. 28. Elsevier GmbH, p. 100179, Mar. 01, 2020. doi: 10.1016/j.wndm.2020.100179.

[9] I. v. Yannas and I. v. Yannas, “Regeneration of Skin,” in *Tissue and Organ Regeneration in Adults*, Springer New York, 2015, pp. 89–136. doi: 10.1007/978-1-4939-1865-2_5.

[10] R. F. Rushmer, K. J. K. Buettner, J. M. Short, and G. F. Odland, “The skin,” *Science*, vol. 154, no. 3747, pp. 343–348, Oct. 1966, doi: 10.1126/science.154.3747.343.

[11] S. Debeer *et al.*, “Comparative histology and immunohistochemistry of porcine versus human skin,” *Eur J Dermatol*, vol. 23, no. 4, pp. 456–66, doi: 10.1684/ejd.2013.2060.

[12] J. M. Reinke and H. Sorg, “Wound Repair and Regeneration,” *European Surgical Research*, vol. 49, no. 1, pp. 35–43, Aug. 2012, doi: 10.1159/000339613.

[13] R. Zhao, H. Liang, E. Clarke, C. Jackson, and M. Xue, “Inflammation in chronic wounds,” *International Journal of Molecular Sciences*, vol. 17, no. 12. MDPI AG, Dec. 11, 2016. doi: 10.3390/ijms17122085.

[14] M. A. Fonder, G. S. Lazarus, D. A. Cowan, B. Aronson-Cook, A. R. Kohli, and A. J. Mamelak, “Treating the chronic wound: A practical approach to the care of nonhealing wounds and wound care dressings,” *Journal of the American Academy of Dermatology*, vol. 58, no. 2. pp. 185–206, Feb. 2008. doi: 10.1016/j.jaad.2007.08.048.

[15] T. N. Demidova-Rice, M. R. Hamblin, and I. M. Herman, “Acute and impaired wound healing: Pathophysiology and current methods for drug delivery, part 1: Normal and chronic wounds: Biology, causes, and approaches to care,” *Advances in Skin and Wound Care*, vol. 25, no. 7. NIH Public Access, pp. 304–314, Jul. 2012. doi: 10.1097/01.ASW.0000416006.55218.d0.

[16] “Studies on the Biology of Collagen During Wound Healing: III... : Annals of Surgery.” https://journals.lww.com/annalsofsurgery/Citation/1971/09000/Studies_on_the_Biology_of_Collagen_During_Wound.17.aspx (accessed Mar. 22, 2021).

[17] M. Mahmoudi and L. Gould, “ Opportunities and Challenges of the Management of Chronic Wounds: A Multidisciplinary Viewpoint ,” *Chronic Wound Care Management and Research*, vol. Volume 7, pp. 27–36, Jul. 2020, doi: 10.2147/cwcmr.s260136.

[18] M. Olsson *et al.*, “The humanistic and economic burden of chronic wounds: A systematic review,” *Wound Repair and Regeneration*, vol. 27, no. 1. Blackwell Publishing Inc., pp. 114–125, Jan. 01, 2019. doi: 10.1111/wrr.12683.

[19] “SCARLETRED - Chronic wounds - Objective telemedicine and remote wound care 2.0 made in Austria.” https://www.scarletred.com/news/show/chronic-wounds---objective-telemedicine-and-remote-wound-care-2.0-made-in-austria (accessed Nov. 06, 2020).

[20] T. Mustoe, “Understanding chronic wounds: A unifying hypothesis on their pathogenesis and implications for therapy,” *American Journal of Surgery*, vol. 187, no. 5 SUPPL. 1, pp. S65–S70, May 2004, doi: 10.1016/S0002-9610(03)00306-4.

[21] “Recognizing and Diagnosing Ischemia in Wound Treatment.” https://www.woundsource.com/blog/recognizing-and-diagnosing-ischemia-in-wound-treatment (accessed Mar. 23, 2021).

[22] S. Roy *et al.*, “Characterization of a preclinical model of chronic ischemic wound,” *Physiol Genomics*, vol. 37, pp. 211–224, 2009, doi: 10.1152/physiolgenomics.90362.2008.

[23] R. Nunan, K. G. Harding, and P. Martin, “Clinical challenges of chronic wounds: Searching for an optimal animal model to recapitulate their complexity,” *DMM Disease Models and Mechanisms*, vol. 7, no. 11, pp. 1205–1213, Nov. 2014, doi: 10.1242/dmm.016782.

[24] N. J. Turner, D. Pezzone, and S. F. Badylak, “Regional variations in the histology of porcine skin,” *Tissue Engineering - Part C: Methods*, vol. 21, no. 4, pp. 373–384, Apr. 2015, doi: 10.1089/ten.tec.2014.0246.

[25] W. Meyer, R. Schwarz, and K. Neurand, “The skin of domestic mammals as a model for the human skin, with special reference to the domestic pig.,” *Current problems in dermatology*, vol. 7, pp. 39–52, 1978, doi: 10.1159/000401274.

[26] W. Meyer, “BEMERKUNGEN ZUR EIGNUNG DER SCHWEINEHAUT ALS BIOLOGISCHES MODELL FUR DIE HAUT DES MENSCHEN,” *Hautarzt*, vol. 47, no. 3. Springer, pp. 178–182, Mar. 1996. doi: 10.1007/s001050050399.

[27] "„Wilfried Meyer, Die Haut des Schweines“ – Bücher gebraucht, antiquarisch & neu kaufen." https://www.booklooker.de/B%C3%BCcher/Angebote/autor=Wilfried+Meyer&titel=Die+Haut+des+Schweines (accessed Mar. 21, 2021).

[28] "Die Haut des Schweines: vergleichende histologische und histochemische ... - Wilfried Meyer - Google Books." https://books.google.je/books/about/Die_Haut_des_Schweines.html?hl=de&id=FqAEAQAAIAAJ&utm_source=gb-gplus-shareDie (accessed Mar. 21, 2021).

[29] A. R. Moxr and F. C. Henriques, "STUDIES OF THERMAL INJURY II. THE RELATIVE IMPORTANCE OF TIME AND SURFACE TEMPERATURE IN THE CAUSATION OF CUTANEOUS BUBTNs *."

[30] G. A. Simon and H. I. Maibach, "The pig as an experimental animal model of percutaneous permeation in man: Qualitative and quantitative observations - An overview," *Skin Pharmacology and Applied Skin Physiology*, vol. 13, no. 5. S. Karger AG, pp. 229–234, 2000. doi: 10.1159/000029928.

[31] "Nanotechnology patent survey: Who will be the leaders in the fifth technology revolution?" https://www.researchgate.net/publication/290125602_Nanotechnology_patent_survey_Who_will_be_the_leaders_in_the_fifth_technology_revolution (accessed Jun. 01, 2021).

[32] "What is Nanotechnology? | nano.gov." https://www.nano.gov/nanotech-101/what/definition (accessed Nov. 17, 2020).

[33] S. Bayda, M. Adeel, T. Tuccinardi, M. Cordani, and F. Rizzolio, "The history of nanoscience and nanotechnology: From chemical-physical applications to nanomedicine," *Molecules*, vol. 25, no. 1. MDPI AG, p. 112, 2020. doi: 10.3390/molecules25010112.

[34] Katz, "Synthesis, Properties and Applications of Magnetic Nanoparticles and Nanowires—A Brief Introduction," *Magnetochemistry*, vol. 5, no. 4, p. 61, Nov. 2019, doi: 10.3390/magnetochemistry5040061.

[35] E. Katz, "Magnetic Nanoparticles," *Magnetochemistry*, vol. 6, no. 1, p. 6, Jan. 2020, doi: 10.3390/magnetochemistry6010006.

[36] L. Mohammed, H. G. Gomaa, D. Ragab, and J. Zhu, "Magnetic nanoparticles for environmental and biomedical applications: A review," *Particuology*, vol. 30. Elsevier B.V., pp. 1–14, Feb. 01, 2017. doi: 10.1016/j.partic.2016.06.001.

[37] K. Wu, D. Su, J. Liu, R. Saha, and J. P. Wang, "Magnetic nanoparticles in nanomedicine: A review of recent advances," *Nanotechnology*, vol. 30, no. 50, p. 502003, Sep. 2019, doi: 10.1088/1361-6528/ab4241.

[38] K. Wu, D. Su, J. Liu, R. Saha, and J. P. Wang, "Magnetic nanoparticles in nanomedicine: A review of recent advances," *Nanotechnology*, vol. 30, no. 50, p. 502003, Sep. 2019, doi: 10.1088/1361-6528/ab4241.

[39] H. Markides, M. Rotherham, and A. J. el Haj, “Biocompatibility and toxicity of magnetic nanoparticles in regenerative medicine,” *Journal of Nanomaterials*, vol. 2012. 2012. doi: 10.1155/2012/614094.

[40] V. der Medizinischen Fakultät, J. Oversohl aus Aachen Berichter, H. Professor med Andreas Horst Mahnken, and med Dipl-Ing Thomas Schmitz-Rode, “Magnetische Thermoablation mit Ferrofluiden: Einfluss von Gewebeart und Applikationsweg auf den thermischen Effekt,” 2009.

[41] A. H. Lu, E. L. Salabas, and F. Schüth, “Magnetic nanoparticles: Synthesis, protection, functionalization, and application,” *Angewandte Chemie - International Edition*, vol. 46, no. 8. pp. 1222–1244, Feb. 12, 2007. doi: 10.1002/anie.200602866.

[42] H. M. Williams, “The application of magnetic nanoparticles in the treatment and monitoring of cancer and infectious diseases,” *Bioscience Horizons: The International Journal of Student Research*, vol. 10, Aug. 2017, doi: 10.1093/biohorizons/hzx009.

[43] W. Wu, Q. He, and C. Jiang, “Magnetic iron oxide nanoparticles: Synthesis and surface functionalization strategies,” *Nanoscale Research Letters*, vol. 3, no. 11, pp. 397–415, Nov. 2008, doi: 10.1007/s11671-008-9174-9.

[44] C. Y. Chiu, T. W. Chung, S. Y. Chen, and Y. H. Ma, “Effects of PEGylation on capture of dextran-coated magnetic nanoparticles in microcirculation,” *International Journal of Nanomedicine*, vol. 14, pp. 4767–4780, 2019, doi: 10.2147/IJN.S204844.

[45] Y. Gao, Y. Liu, and C. Xu, “Magnetic nanoparticles for biomedical applications: From diagnosis to treatment to regeneration,” in *Engineering in Translational Medicine*, vol. 9781447143727, Springer-Verlag London Ltd, 2014, pp. 567–583. doi: 10.1007/978-1-4471-4372-7_21.

[46] T. Yousaf, G. Dervenoulas, and M. Politis, “Advances in MRI Methodology,” in *International Review of Neurobiology*, vol. 141, Academic Press Inc., 2018, pp. 31–76. doi: 10.1016/bs.irn.2018.08.008.

[47] C. Alexiou *et al.*, “Magnetic drug targeting - Biodistribution of the magnetic carrier and the chemotherapeutic agent mitoxantrone after locoregional cancer treatment,” *Journal of Drug Targeting*, vol. 11, no. 3, pp. 139–149, Apr. 2003, doi: 10.1080/1061186031000150791.

[48] C. Alexiou *et al.*, “Magnetisches Drug Targeting - Ein neuer ansatz in der lokoregionären tumortherapie mit chemotherapeutika. Tierexperimentelle untersuchungen,” *HNO*, vol. 53, no. 7, pp. 618–622, Jul. 2005, doi: 10.1007/s00106-004-1146-5.

[49] A. J. GIUSTINI, A. A. PETRYK, S. M. CASSIM, J. A. TATE, I. BAKER, and P. J. HOOPES, “MAGNETIC NANOPARTICLE HYPERTHERMIA IN CANCER TREATMENT,” *Nano LIFE*, vol. 01, no. 01n02, pp. 17–32, Mar. 2010, doi: 10.1142/s1793984410000067.

[50] R. K. GILCHRIST, R. MEDAL, W. D. SHOREY, R. C. HANSELMAN, J. C. PARROTT, and C. B. TAYLOR, “Selective inductive heating of lymph nodes,” *Annals of surgery*, vol. 146, no. 4, pp. 596–606, Oct. 1957, doi: 10.1097/00000658-195710000-00007.

[51] X. Liu *et al.*, “Comprehensive understanding of magnetic hyperthermia for improving antitumor therapeutic efficacy,” *Theranostics*, vol. 10, no. 8, pp. 3793–3815, 2020, doi: 10.7150/thno.40805.

[52] X. Liu *et al.*, “Comprehensive understanding of magnetic hyperthermia for improving antitumor therapeutic efficacy,” *Theranostics*, vol. 10, no. 8, pp. 3793–3815, 2020, doi: 10.7150/thno.40805.

[53] C. C. Goh, J. L. Y. Li, D. Becker, W. Weninger, V. Angeli, and L. G. Ng, “Inducing ischemia-reperfusion injury in the mouse ear skin for intravital multiphoton imaging of immune responses,” *Journal of Visualized Experiments*, vol. 2016, no. 118, p. 54956, Dec. 2016, doi: 10.3791/54956.

[54] K. T. Mankin, “Axial Pattern Flaps,” *Veterinary Clinics of North America: Small Animal Practice*, vol. 47, no. 6, pp. 1237–1247, Nov. 2017, doi: 10.1016/j.cvsm.2017.06.008.

[55] J. M. Jia *et al.*, “Control of cerebral ischemia with magnetic nanoparticles,” *Nature Methods*, vol. 14, no. 2, pp. 160–166, Feb. 2017, doi: 10.1038/nmeth.4105.

[56] “Essentials of Real-Time PCR | Thermo Fisher Scientific - AT.” https://www.thermofisher.com/at/en/home/life-science/pcr/real-time-pcr/real-time-pcr-learning-center/real-time-pcr-basics/essentials-real-time-pcr.html (accessed Apr. 18, 2021).

[57] M. Saint-Geniez *et al.*, “Fatty acid binding protein 4 deficiency protects against oxygen-induced retinopathy in mice,” *PLoS ONE*, vol. 9, no. 5, May 2014, doi: 10.1371/journal.pone.0096253.

[58] C. Chen *et al.*, “Ultrasound assessment of skin thickness and stiffness: The correlation with histology and clinical score in systemic sclerosis,” *Arthritis Research and Therapy*, vol. 22, no. 1, p. 197, Aug. 2020, doi: 10.1186/s13075-020-02285-x.

[59] S. Moein, S. Javanmard, M. Abedi, M. Izadpanahi, and Y. Gheisari, “Identification of Appropriate Housekeeping Genes for Gene Expression Analysis in Long-term Hypoxia-treated Kidney Cells,” *Advanced Biomedical Research*, vol. 6, no. 1, p. 15, 2017, doi: 10.4103/2277-9175.200790.

[60] H. H. Jeon *et al.*, “FOXO1 regulates VEGFA expression and promotes angiogenesis in healing wounds,” *Journal of Pathology*, vol. 245, no. 3, pp. 258–264, Jul. 2018, doi: 10.1002/path.5075.

[61] J. E. Albina, B. Mastrofrancesco, J. A. Vessella, C. A. Louis, W. L. Henry, and J. S. Reichner, “HIF-1 expression in healing wounds: HIF-1α induction in primary inflammatory cells by TNF-α,” *American Journal of Physiology-Cell Physiology*, vol. 281, no. 6, pp. C1971–C1977, Dec. 2001, doi: 10.1152/ajpcell.2001.281.6.C1971.

[62] P. Auguste, S. Javerzat, and A. Bikfalvi, “Regulation of vascular development by fibroblast growth factors,” *Cell and Tissue Research*, vol. 314, no. 1. Springer, pp. 157–166, Oct. 08, 2003. doi: 10.1007/s00441-003-0750-0.

[63] E. Hofmann *et al.*, “A novel human ex vivo skin model to study early local responses to burn injuries,” *Scientific Reports*, vol. 11, no. 1, Dec. 2021, doi: 10.1038/s41598-020-79683-3.

[64] X. Terra *et al.*, “FABP 4 is associated with inflammatory markers and metabolic syndrome in morbidly obese women,” *European Journal of Endocrinology*, vol. 164, no. 4, pp. 539–547, Apr. 2011, doi: 10.1530/EJE-10-1195.

[65] H. M. DeLisser, P. J. Newman, and S. M. Albelda, “Molecular and functional aspects of PECAM-1/CD31,” *Immunology Today*, vol. 15, no. 10, pp. 490–495, 1994, doi: 10.1016/0167-5699(94)90195-3.

[66] S. Tadokoro *et al.*, “Leptin promotes wound healing in the skin,” *PLoS ONE*, vol. 10, no. 3, Mar. 2015, doi: 10.1371/journal.pone.0121242.

Abbreviations

ABS	Absorbance
ACTA	Cell motility protein actin alpha 2, smooth muscle
AMF	Alternating magnetic field
CD209/14	Cluster of differentiation 209/14
CLA	Conjugated linoleic acid
CXCL-8	Chemokine C-X-C motif ligand 8
DC	Dendritic cells
ECM	Extracellular matrix
FABP4	Fatty acid binding protein 4
FGF	Fibroblast growth factor
IL1	Interleukin-1
IONP	Iron oxide nanoparticles
KRT	Keratin
LEP	Leptin
mg	Milligram
MH	Magnetic hyperthermia
ml	Milliliter
mm	Millimeter
MNP	Magnetic nanoparticles
MRI	Magnetic resonance imaging
NdFeB	Neodymium iron boron
nm	Nanometer
PCR	Polymerase chain reaction
PECAM	Platelet endothelial cell adhesion molecule
PEG	Polyethylene glycol
PFA	Perfluoroalkoxy
PPARγ	Peroxisome proliferator-activated receptor γ
qPCR	Quantitative polymerase chain reaction

RES	Reticuloendothelial system
ROS	Reactive oxygen species
RT	Reverse transcriptase
SIS	Skin immune system
Ss	Sus scrufa (Pig)
STM	Scanning tunnelling microscope
VEGFA	Vascular endothelial growth factor
µg	Microgram

Appendix

Table 16: Average cutis thicknesses of pig 1 at all examined positions (n=3).

Position	Average cutis d [µm] (n=3)	Standard deviation
Bx01	2343,0	190,5
Bx02	2106,7	249,8
Bx03	2027,3	520,3
Bx04	2333,3	125,7
Bx05	1849,7	283,7
Bx06	1844,3	79,6
Bx07	1699,3	59,7
Bx08	2003,7	174,0
Bx09	1867,3	210,3
Bx10	2033,3	130,3
Bx11	1903,3	116,4
Bx12	2185,0	104,5
Bx13	1764,0	26,9
Bx14	1548,7	227,0
Bx15	1703,7	113,4
Bx16	1805,7	311,0

Table 17: Average cutis thicknesses of pig 2 at all examined positions (n=3).

Position	Average dermis d [µm] (n=3)	Standard deviation
Bx01	2119,3	97,1
Bx02	2032,3	266,0
Bx03	1936,3	510,9
Bx04	2271,0	156,9
Bx05	1762,7	268,9
Bx06	1736,7	55,8
Bx07	1607,3	100,9
Bx08	1844,3	133,3
Bx09	1762,0	190,3
Bx10	1949,0	130,8
Bx11	1795,3	101,5
Bx12	2031,0	155,4
Bx13	1604,3	87,3
Bx14	1443,3	236,6
Bx15	1582,7	153,8
Bx16	1679,3	332,4

Table 18: Average cutis thicknesses of pig 3 at all examined positions (n=3).

Position	Average epidermis d [µm] (n=3)	Standard deviation
Bx01	117,1	9,4
Bx02	117,3	10,3
Bx03	97,2	14,5
Bx04	100,9	14,9
Bx05	114,3	28,3
Bx06	106,0	15,0
Bx07	111,2	10,9
Bx08	140,8	45,7
Bx09	104,1	21,3
Bx10	85,9	9,8
Bx11	97,0	9,5
Bx12	113,8	14,0
Bx13	118,5	25,7
Bx14	98,8	16,1
Bx15	103,1	20,7
Bx16	116,0	22,3

***Table 19: Average cutis thicknesses of Pig 1-3** at the 16 examined positions (n=3) arranged in a position-specific subdivision.*

Position	Average cutis d [µm] (n=3)	Standard deviation
Bx01	2343,0	190,5
Bx05	1849,7	283,7
Bx09	1867,3	210,3
Bx13	1764,0	26,9
Bx02	2106,7	249,8
Bx06	1844,3	79,6
Bx10	2033,3	130,3
Bx14	1548,7	227,0
Bx03	2027,3	520,3
Bx07	1699,3	59,7
Bx11	1903,3	116,4
Bx15	1703,7	113,4
Bx04	2333,3	125,7
Bx08	2003,7	174,0
Bx12	2185,0	104,5
Bx16	1805,7	311,0

Table 20: Average dermis thicknesses of Pig 1-3 at the 16 examined positions (n=3) arranged in a position-specific subdivision.

Position	Average dermis d [µm] (n=3)	Standard deviation
Bx01	2119,3	97,1
Bx05	1762,7	268,9
Bx09	1762,0	190,3
Bx13	1604,3	87,3
Bx02	2032,3	266,0
Bx06	1736,7	55,8
Bx10	1949,0	130,8
Bx14	1443,3	236,6
Bx03	1936,3	510,9
Bx07	1607,3	100,9
Bx11	1795,3	101,5
Bx15	1582,7	153,8
Bx04	2271,0	156,9
Bx08	1844,3	133,3
Bx12	2031,0	155,4
Bx16	1679,3	332,4

Table 21: Average epidermis thicknesses of Pig 1-3 at the 16 examined positions (n=3) arranged in a position-specific subdivision.

Position	Average epidermis d [µm] (n=3)	Standard deviation
Bx01	117,1	9,4
Bx05	114,3	28,3
Bx09	104,1	21,3
Bx13	118,5	25,7
Bx02	117,3	10,3
Bx06	106,0	15,0
Bx10	85,9	9,8
Bx14	98,8	16,1
Bx03	97,2	14,5
Bx07	111,2	10,9
Bx11	97,0	9,5
Bx15	103,1	20,7
Bx04	100,9	14,9
Bx08	140,8	45,7
Bx12	113,8	14,0
Bx16	116,0	22,3

Table 22: Average dermis thicknesses of Pig 1-3 at the 16 examined positions (n=3) according to the ultrasound based measurement, arranged in a position-specific subdivision.

Position	Average Dermis [µm] (n=3)	Standard deviation
Bx01	1376	207
Bx05	1206	232
Bx09	1363	218
Bx13	1309	166
Bx02	1249	192
Bx06	1576	387
Bx10	1367	244
Bx14	1600	183
Bx03	1119	106
Bx07	1473	484
Bx11	1236	134
Bx15	1802	183
Bx04	1187	146
Bx08	1589	250
Bx12	1275	356
Bx16	1573	119

Table 23: Used gene expression assays (PrimePCR™ Probe Assays; Bio-Rad Laboratories, Inc.; California, United States)

Gene	Name; commonly used aliases	Cat. No.
CXCL8	C–X–C motif chemokine ligand 8; interleukin 8 (IL8)	qSscCEP0036027
IL1B	Interleukin 1 beta	qSscCEP0030960
VEGFA	Vascular endothelial growth factor A	qSscCIP0026316
ACTA2	Actin alpha 2, smooth muscle; alpha smooth muscle actin (aSMA)	qSscCIP0033051
FGF2	Fibroblast growth factor 2; basic FGF (bFGF)	qSscCIP0023090
KRT5	Keratin 5	qSscCEP0036673
LEP	Leptin	qSscCEP0030032
PECAM-1	platelet endothelial cell adhesion molecule-1/ CD31	qSscCEP0041667
CD209	CD209 molecule	qSscCIP0041340
CD14	CD14 molecule	qSscCEP0038078
FABP4	adipocyte fatty acid-binding protein	Ss03373313_m1
HIF1a	hypoxia inducible factor 1, alpha subunit	qSscCIP0025745
ACTAB	Beta-Actin, cytoplasmic 1 Actin	qSscCEP0032507